MULTI-SCALE MECHANO-CHEMISTRY – FROM ATOMIC FORCE MICROSCOPY TO GRAM SCALE SYNTHESIS

A Dissertation

by

SHIVARANJAN RAGHURAMAN

Submitted to the Office of Graduate and Professional Studies of
Texas A&M University
in partial fulfillment of the requirements for the degree of

DOCTOR OF PHILOSOPHY

Chair of Committee,	Jonathan R. Felts
Committee Members,	James D. Batteas
	Hong Liang
	Dion Antao
Head of Department,	Andreas Polycarpou

May 2020

Major Subject: Mechanical Engineering

ABSTRACT

This dissertation systematically explores the fundamental connections between mechano-chemistry, nano-tribology and nano-mechanics. Mechanically induced chemical change is arguably the most primitive class of chemistry humans have explored, yet its physical origins largely remain a mystery. A theoretical framework based on chemical kinetics and transition state theory is provided to rationalize the influence of force on thermal and electrochemical reactions. Thermal reduction of graphene by a heated atomic force microscope tip and electrochemical oxidation of graphene through local anodic oxidation can be effectively measured by monitoring friction change. It is observed that applied normal force can accelerate the reactions and reduce the energy barrier by distorting the energy landscape of the underlying chemical processes. The activation length can be estimated from our experiments from accompanying MD simulations to assess the nature of contact between the tip and substrate. The force-modified energetics or Hammond effect can be utilized to alter the reaction conditions, forward and backward rates and even render reactions barrierless. The same notion of thermally activated process modulated by force was applied to describe folding and crease formation events in three-dimensional crumpled graphene structures. Force-indentation curves on crumpled structures show reversible and irreversible energy dissipations that bear indications to the quantity of crease formation events during deformation. The energy absorption characteristics of crumples depended strongly with chemistry of their starting flat sheets, where, graphene oxide showed greater amenability to form stable folds. The fundamental

insights of mechano-chemistry were tested at the gram scale by introducing a novel mechano-chemical reactor. By adding force control and measuring impacts with microsecond time resolution, kinetics of particle size reduction was demonstrated to strongly depend on the magnitude of applied force. Incorporating *in situ* chemical measurement techniques can transform the reactor into an indispensable tool for probing solid state reactions in both labs and other research facilities. The theoretical framework, nanoscale tip-based experiments and gram scale synthesis discussed in this dissertation lay the foundation to conduct mechano-chemistry across spatial scales.

ACKNOWLEDGEMENTS

I would like to thank my advisor, Dr. Jonathan Felts, for the opportunity to pursue my Ph.D. under his advisement. He generously invested his time, money and resources to shape me into a successful student and a scientist. He encouraged developing original ideas and provided extra support and time to pursue them independently. Working with him was an inspiring experience every single day and these five years will remain the most enjoyable part of my scientific career. I would also like to thank Dr. James Batteas for his advice and active participation in our projects. I sincerely thank my doctoral committee for their time and advise throughout my Ph.D. I would like to thank my fellow lab mates and collaborators from other groups who encouraged new research directions and nudged me into disciplines other than traditional mechanical engineering.

I would like to thank my father who is the only reason for beginning my career in science. He diversified my childhood interests and let me pursue my dreams. I try very hard to emulate him and I will miss him my entire life. I would like to thank my mother for her equally immense support and sacrifice, without which I could not have dreamed to pursue my Ph.D. I owe my success and accomplishments to my entire extended family, who supported me through the demise of my father to keep me focused, motivated and to preserve my will to advance as a scientist.

CONTRIBUTIONS AND FUNDING SOURCES

This work was supervised by a dissertation committee consisting of Dr. Jonathan Felts (advisor), Dr. Dion Antao and Dr. Cynthia Hipwell of the Department of Mechanical Engineering and Dr. James Batteas of the Department of Chemistry at Texas A&M University.

Study presented in Chapter 2 and Chapter 5 was performed in collaboration with Dr. James Batteas of the Department of Chemistry at Texas A&M University. Dr. Megan Elinski of the Department of Chemistry performed Raman Thermometry to calibrate the heated AFM tips shown in Chapter 2. Dr. Zhijiang Ye of the Department of Mechanical and Manufacturing Engineering at Miami University provided the Molecular Dynamics results and Dr. Mohammadreza Soleymaniha of the Department of Mechanical Engineering at Texas A&M University provided the Finite Element Simulations presented in Chapter 3. Study presented in Chapter 4 was performed in collaboration with Dr. Micah Green of the Department of Chemical Engineering at Texas A&M University. Dr. Dorsa Parviz and Dr. Smit Alkesh Shah of the Department of Chemical Engineering at Texas A&M University provided the crumpled graphene samples shown in Chapter 4. The reactor shown in Chapter 5 was fabricated in collaboration with Ubaldo Lopez, the lead machinist at Machining Facility of the Department of Mechanical Engineering and the Fischer Engineering Design Center.

All other work presented in this dissertation was independently completed by the student.

The study in this dissertation were made possible in part by support from the Texas A&M Engineering Experiment Station, Texas A&M Energy Institute, Texas A&M University X-Grant and the National Science Foundation (CMMI-1436192).

NOMENCLATURE

Δx_o	Path Length
E_a	Thermal Activation Barrier
F_C	Faraday's Constant
f_{max}	Maximum Friction
I_{Scan}	Current Per Scan
I_{Tot}	Total Current
L_1	Length of Flat Region
L_2	Length of Bent Region
L_{Total}	Total Length of Fold
n_a	Number of Active Site
n_e	Number of Electrons Transferred
N_s	Number of AFM Image Scans
V_p	Product Potential
V_r	Reactant Potential
γ_p	Width of Product Well
γ_r	Width of Reactant Well
ΔG_o	Gibb's Free Energy
A	Exponential Pre-factor/Attempt Frequency
a	Tip Radius
AFM	Atomic Force Microscopy

C	Concentration
DC	Direct Current
DFT	Density Functional Theory
E_{eff}	Effective Energy Barrier
ESM	Electrochemical Strain Microscopy
eV	Electron Volts
fA	Femto Ampere
FEM	Finite Element Method
FWHM	Full Width Half Maximum
GO	Graphene Oxide
H_2O	Water
k	Boltzmann's Constant
k_f	Rate Constant
LAO	Local Anodic Oxidation
MD	Molecular Dynamics
MHz	Mega-Hertz
n	Reaction Order
η	*Overpotential*
nN	nano newton
OER	Oxygen Evolution Reaction
p	Pitch between Scan Lines
PDS	Potential Determining Step

PEEK	Polyether Ether Ketone
PES	Potential Energy Surface(s)
RDS	Rate Determining Step
rpm	rotations per minute
R_{tip}	*Tip Radius*
SECM	Scanning Electrochemical Microscopy
SEM	Scanning Electron Microscope/Microscopy
SiO_2	Silicon Oxide
SPM	Scanning Probe Microscopy
T	Temperature
t	Time
TEM	Transmission Electron Microscope/Microscopy
ThDM	Thermal Desorption Microscopy
$U_{Adhesion}$	Adhesion Energy
U_{Bend}	Bending Rigidity
v	Velocity
VFD	Variable Frequency Drive
x	Reaction Coordinate
Y_{eff}	Effective Young's Modulus
$\alpha(F_N, \eta)$	Symmetry Factor
β	Temperature Ramp Rate
δ	Indentation

Δf	Change in Friction Per Scan
ζ	Voltage Ramp rate
λ	Rate of a Reaction
ν	Exponential Pre-factor
$\psi(F_N)$	Effect of Force on Energy Landscape

TABLE OF CONTENTS

Page

LIST OF FIGURES

Page

CHAPTER I

INTRODUCTION TO MULTI-PHYSICAL MECHANO-CHEMICAL REACTIONS*

Introduction

Mechanochemistry or mechanically induced chemical change is arguably the most primitive class of chemistry that humans have explored[1]. The earliest mechanochemical reaction can be attributed to man creating and controlling fire by rubbing wood pieces against each other. The oldest surviving document of chemistry was written by Theophrastus, a Greek philosopher, in the fourth century B.C. and possibly describes mechanochemical conversion of mercury sulfide into pure mercury by grinding in a copper vessel. Whereas, the nineteenth and twentieth century has seen more systematic observations of chemical effects due to mechanical action in the fields including grinding and milling[2], photography[3], phase transformation and mechanical alloying[4], geology[5] and solid-state organic chemistry[6].

Mechanochemistry is fundamentally different from other conventional classes of chemistry such as thermochemistry and photochemistry. Mechanical energy on a chemical bond can act along with other forms of energy, thereby altering the reaction conditions and the energy barrier of a reaction. However, force being a vector quantity and chemical bonds inherently being directional together lead to strengthening or weakening of chemical bonds. This results in unique reaction pathways that can accelerate or retard

---

*Reprinted with permission from "Driving Surface Chemistry at the Nanometer Scale Using Localized Heat and Stress" by Raghuraman, S., Elinski, M.B., Batteas, J.D. and Felts, 2017. *Nano Letters*, 17(4), 2111-2117, Copyright [2017] by American Chemical Society and "The Role of Mechanical Force on the Kinetics and Dynamics of Electrochemical Redox Reactions on Graphene" by Raghuraman, S., Soleymaniha, M., Ye, Z. and Felts, J.R., 2018. *Nanoscale*, 10(37), 17912-17923, Copyright [2018] by The Royal Society of Chemistry.

chemical processes. Further, in chemical systems beyond simple diatomic molecules, the direction of applied force can affect the ensemble of chemical bonds differently and influence product selectivity.

Atomic Force Microscopy in Mechano-chemistry

Despite its unique nature, the physical origins of mechanochemistry remained largely unexplored for most of the twentieth century until the invention of Scanning Probe Microscopy (SPM), alternatively known as Atomic Force Microscopy (AFM). AFMs primarily consist of an atomically sharp tip raster scanning on samples making it a high-resolution surface imaging technique (Figure 1(a)). The AFM tip is a spring like cantilever with a sharp conical or pyramidal tip at its end (Figure 1(c)). The position of the tip along the Z (vertical) axis is controlled by a piezo positioner. When the piezo positioner extends, tip pushes against a sample and the cantilever bends or deflects proportional to the applied force. This deflection is typically tracked by a laser bounce back method, where a laser shining on the polished back side of the tip gets reflected and detected by a photodetector. The photodetector has a four-quadrant detection (Figure 1(a) shows the four quadrants A, B, C and D) in which a vertical cantilever deflection alters the position of the laser on the detector along the vertical axis. Therefore, difference in laser intensities between the top two and bottom two quadrants (i.e. (A+B) ~ (C+D)) is proportional to the vertical cantilever deflection. Imaging in an AFM is typically performed by raster scanning the sample stage using piezo positioners in the X and Y directions. When the tip is in contact with the sample, any movement in the X direction causes the AFM tip to twist due to long range forces and friction. This torsion due to friction is picked up by the photodetector as

a change along its horizontal axis. A change in intensity between the left two and the right two quadrants of the photodetector (i.e. (A+C) ~ (B+D)) is a measure of friction between the tip and surface.

The simplicity behind AFMs enabled atomic scale imaging and laid foundations for investigations of chemical bonds using atomic scale forces in unprecedented spatial detail. AFMs transformed from just an imaging tool into a nano-reactor which can explore complex chemical processes with sub 1nN force scales. AFMs are versatile as shown in Figure 1(b), where the chemistry of the tip, surface and the environment can be arbitrarily chosen to mimic real-operating conditions. Attaching a functional group to an AFM tip can make it chemically sensitive to specific functional groups on surface. AFMs can be run in ambient, liquid and ultra-high vacuum environments. In addition, external stimuli such as electric field, light and magnetic fields can be employed to obtain chemical measurements and to explore specific reaction pathways. Nano IR and tip enhanced Raman spectroscopies on 2D materials are prime examples of adapting AFM to obtain in situ independent chemical measurements while driving interfacial chemical processes. AFMs have also been integrated with Scanning electron Microscopes (SEM) and Transmission Electron Microscopes (TEM) to directly observe Tip-Surface interactions at the atomic scale.

The ability of AFMs to driving many classes of chemical processes combined with its high degree of control over applied forces makes it the most suitable tool to investigate nanoscale analogs of real life mechanochemical reactions. AFMs can detach individual molecules from a surface and in the process measure the rupture force as a function of

force loading and unloading rates[7-11]. Several scanning probe based studies of mechanochemistry show that applying force on the reacting species can significantly affect the rate of a chemical reaction and even result in products impossible through other chemical methods[12, 13]. AFMs have been employed extensively to mimic real life sliding interfaces to probe high pressure and high shear wear at solid-solid and solid-liquid interfaces. Both wear and film growth phenomena have been shown to strongly depend on applied load suggesting the can be explained as thermally activated processes. Atomic scale stress assisted photochemical and electrochemical reactions have been explored using tip-based techniques.

In spite of substantial progress in tip-based chemistry, there is a lack of quantitative framework – similar to thermo-, electro- and photo-chemistry - which prevents us from unifying mechanochemistry with the rest. As a result, most studies are qualitative and fail to describe the force-driven reactions in terms of traditional thermodynamic descriptors, providing little insight into the rates and energetics of the processes driven.

This dissertation explores mechanochemistry at the nanoscales and the macroscale and provides a theoretical and experimental framework based on chemical kinetics to unify mechanochemistry with tribology. This quantitative approach enables us to rationalize findings at the nanoscale in terms of reaction dynamics and extend the insights to gram scale material synthesis.

Theory of Multi-Physical Mechano-chemical Reactions

There are several means of accelerating a chemical reaction and perhaps the most common ways are using heat (thermochemistry) and electric field (electrochemistry). A

relatively less understood way of initiating chemical reactions is by using mechanical force (mechanochemistry). Decades of research shows that electrochemical or mechanochemical reactions can lead to different reaction pathways in comparison to thermochemical reactions and sometimes even lead to different products even when starting from the same reactants[14, 15].

Despite this, an efficient way to describe all chemical reactions in general is by representing how the potential energy of the reactant structure changes as it undergoes the chemical transformation. Such representations are called potential energy surfaces (PES), are multi-dimensional quantum mechanical calculations and consider the bond distances and structural changes along various geometric coordinates during the transformation. For example, Figure 2A shows an arbitrary model potential energy surface (PES)[16], where two axes are geometric coordinates and the third axis is the potential energy. PESs can immediately indicate two distinct features - potential energy wells and energy barriers (hills). The lowest points of the energy wells are the reactant and product structures. The first order saddle point on the energy surface is called the Transition structure. Basically, this is the point which is minimum in all directions except one.

A chemical reaction can therefore be described as the path taken along the energy surface during the reactant to product transformation while going through the transition structure. This path is more formally called as the “Reaction Pathway” and is shown as a thick red line in Figure 2A (also shown in Figure 2B by projecting along the reaction pathway). The notion of reaction pathways can simplify complicated multi-dimensional PES onto 1D profiles often called as “Reaction Coordinate Profiles”**[17]**.

While the PES and the resulting 1D reaction coordinate profiles are calculated from the interatomic potentials, the energy wells can be approximated to be parabolic in the limit that the bond is not stretched too far away from the equilibrium position[18]. Mathematically,

$$V_r(x) = \frac{x^2}{\gamma_r} \tag{1}$$

$$V_p(x) = \frac{\left(x-\Delta x_o^{\ddagger}\right)^2}{\gamma_p} + \Delta G_o \tag{2}$$

here, curve V_r and V_p are the potential energy profiles for the reactants and products as a function of the path length coordinate (x) (blue curve in Figure 3. The path length $\Delta x_o^{\ddagger}$ is the distance between the reactant and product states along the reaction coordinate, and γ_r and γ_p determine the width of the parabolic well and are analogous to spring compliance. The net chemical reaction is the sum of forward and backward reactions, where both the reactants and products proceed through a common transition state. The energy difference between the reactant and product minimum is the standard Gibbs free energy (ΔG_o). The energy difference between the reactant state and the top of this barrier is the activation energy.

The picture of reaction coordinates given so far is for a purely thermochemical reaction. Whereas, we study reactions driven by multiple sources such as force and electric field in addition to temperature. Each of these drivers can influence the potential energy surfaces and the reaction coordinate profiles. For instance, applying an electric field applies a force on the electrons, causing them to migrate towards surfaces and altering

transition state barriers. Thus, the external work done by the electric field significantly enhances the forward reaction and lowers the energy barrier. This can be perceived as translating the reactant potential vertically by the constant external work.

On the other hand, when mechanical force is applied to the reactants, the mechanical energy performs work to drive reactants from one energy minimum to another when the applied force aligns with the reaction coordinate[19-21]. An applied force distorts the multi-dimensional PES. Considering a single representative reaction coordinate simplifies this notion and in 1D the effect of force is a tilting of the potential energy curve shown by the red curve in Figure 3. Such tilting can accelerate or decelerate reactions dependent on the direction of the applied load[22]. We modified the potential energy curve for a thermochemical reaction to incorporate the effects of applied force F and Voltage V as,

$$V_r(x) = \frac{x^2}{\gamma_r} - Fx - n_e F_c V \tag{3}$$

$$V_p(x) = \frac{\left(x - \Delta x_o^{\ddagger}\right)^2}{\gamma_p} + \Delta G_o - Fx \tag{4}$$

where, n_e is the number of electrons transferred and F_C is Faraday's Constant. The energy barrier for the forward reaction is the difference between the transition state energy and the reactant energy minimum, that is,

$$E_{eff} = V_r(x_{\max}) - V_r\left(x_{r,\min}\right) \tag{5}$$

This results in an effective activation barrier (*Eeff*)for the forward reaction of the form,

$$E_{eff} = E_a + \alpha(F_N, V) n_e F_c V - \psi(F_N) \tag{6}$$

$$E_a = \left[\frac{\Delta x_o^2}{4\gamma} + \frac{\Delta G_o}{2\gamma^2} + \frac{\Delta G_o^2}{4\Delta x_o^2 \gamma^2}\right] \tag{7}$$

$$\alpha(F_N, V) = \left[\frac{1}{2} + \frac{\gamma \Delta G_o}{2\Delta x_o^2} - \frac{\gamma F}{2\Delta x_o} + \frac{\gamma n_e F_c V}{4\Delta x_o^2}\right] \tag{8}$$

$$\psi(F_N) = \left[\frac{\Delta x_o}{2} + \frac{\gamma \Delta G_o}{2\Delta x_o}\right] F + \left[\frac{\gamma}{4}\right] F^2 \tag{9}$$

$$\alpha(F_N, V) \sim \alpha(F_N) \sim \left[\frac{1}{2} - \frac{\gamma F}{2\Delta x_o}\right] \tag{10}$$

where E_a is the thermal activation barrier related only to the shape of the potential wells, $\alpha(F_N, V)$ is the convoluted effect of force and applied voltage on the overall energy barrier and conceptually represents the ratio of the slopes of the potential wells for the forward and reverse reactions. For the case of an applied electric field only, and when the effect of the applied electric field is roughly equal to the change in Gibbs free energy, $\alpha(F_N, V) \sim 0.5$, which implies that the slope of the PES for both the forward and reverse reactions are roughly identical. Indeed, this is a common assumption in many electrochemical reaction experiments, as the observed reactions occur over a small voltage potential window close in magnitude to the change in Gibbs free energy[23, 24]. While still including the application of force for this case, alpha merely becomes a linear function of force as in equation(10). The term $\psi(F_N)$ is the effect of force on the energy landscape. This set of equations (6)-(9) gives the general mathematical form for the activation barrier for an electro-mechano-thermo-chemical reaction.

Chemical Kinetics

Isothermal Kinetics: Now, we can see that the effective activation barrier (E_{eff}) is a thermal barrier modified by the applied force and the rate of the forward reaction will proceed according to an Arrhenius relationship as,

$$k_f = A.e^{-\frac{E_{eff}}{kT}} \tag{11}$$

where, k_f is the rate constant, A is the exponential pre factor (also called attempt frequency), k is Boltzmann's constant and T is the temperature. For a purely thermochemical reaction E_{eff} can be obtained by neglecting force and voltage terms in equation set (6)-(9). For an *n*th order reaction, at any given temperature, the reaction rates can be expressed as,

$$\frac{d\lambda}{dt} = k_f[C]^n \tag{12}$$

where, k_f is the rate constant, λ is the rate of the reaction and C is the concentration. Specifically, for a first order reaction,

$$\Delta \mathrm{C}(t) = \lambda_0 e^{-k_f t} + \mathrm{C}_0 \tag{13}$$

where, $\mathrm{C}(t)$ is the concentration as a function of time, k_f is the rate constant and t is time. Therefore, by measuring reaction rates as a function of time at several temperatures, the activation energy can be obtained by using equation (11).

Non-Isothermal Kinetics: As we probe chemical reactions driven by multi-physical sources such as temperature, force and voltage, we require a compact and efficient theoretical framework to describe chemical kinetics. By introducing another variable (say force) into isothermal kinetics we can immediately realize that to reliably measure activation energy as a function of force, we need to obtain several data sets at

many applied forces while each data set requires several constant temperature curves. Clearly, including additional drivers of chemical reactions into the isothermal kinetics framework will increase the size of experiments exponentially.

To overcome the limitations of the isothermal approach, we developed a non-isothermal nanoscale thermal desorption microscopy (NanoThDM) technique to quickly measure activation barriers during a AFM tip-temperature ramp using principles from bulk thermal analysis techniques such as thermogravimetry and temperature programmed desorption[25].

The rate of change of concentration during a linear temperature ramp is governed by,

$$\frac{\mathrm{d}C}{\mathrm{d}T} = \frac{\nu}{\beta} C^{n} \mathrm{e}^{-\frac{(E_{eff})}{kT}} \tag{14}$$

where β is the temperature ramp rate, ν is the exponential pre-factor, C is the concentration of species on the surface, n is the order of reaction, E_a is the activation energy for bond removal, k is the Boltzmann's constant and T is the absolute interface temperature. Integrating equation (14) over temperature has similar form to solutions developed over the last few decades for bulk thermal analysis, and an effective estimation is[26],

$$Q = \frac{\nu}{\beta} \mathrm{e}^{-\frac{E_{eff}}{kT}} \left(\frac{k}{E_{eff}}\right) \left[1 - \left(\frac{kT}{E_{eff}}\right)\right] \tag{15}$$

where,

$$Q = \begin{cases} \dfrac{C^{1-n}}{T^2(1-n)}, & n \neq 1 \\ \ln\left(\dfrac{1}{T^2 C}\right), & n = 1 \end{cases} \tag{16}$$

For a first order reaction, plotting $\ln(Q)$ against $\frac{1}{T}$ yields a straight line with the slope proportional to activation energy (slope=-*E*eff/*k)*. For higher order reactions, a computational approach could be taken to iterate on the reaction order that gives the best straight line fit. Using this non-isothermal technique, activation energies can be directly obtained from a single reaction curve as opposed to the isothermal technique where several curves are required to measure activation energy. Performing temperature ramps makes the experiment compact both in time and sample requirements.

Mechano-Thermal Reactions: To probe mechano-thermal reactions, recall from equation (6) that the effective energy barrier incorporates $\psi(F_N)$ – the non-trivial effect of applied force on thermochemical reactions. Therefore, for a mechano-thermal reaction, by neglecting voltage terms in equations set (6)-(9), equation (14) can be modified to incorporate the definition of effective energy barrier (*Eeff*) as,

$$\frac{\mathrm{d}C}{\mathrm{d}T} = \frac{\nu}{\beta} C^n \mathrm{e}^{-\frac{\left(E_a - \psi(F_N)\right)}{kT}} \tag{17}$$

By obtaining activation energies at various applied forces using the non-isothermal kinetics, the effect of force on a chemical reaction can be experimentally measured using equations set (15)-(16).

Mechano-Electro-Thermal Reactions: For an electrochemical reaction influenced by applied force, we modified the non-isothermal kinetics for a voltage ramp at a constant applied force. The rate of change of surface composition during a voltage ramp can be given as,

$$\frac{dC}{dt} = k_f a^n \tag{18}$$

where, C is composition, t is time, a is concentration of reactant species and n is order of reaction. For a linear voltage ramp rate $\boldsymbol{\zeta}$ [V/s], the time of the experiment is linearly related to the ramp rate as,

$$\zeta = \frac{dV}{dt} \tag{19}$$

Combining equations (11),(18) and (19) provides a kinetic reaction model dependent on voltage ramp rate, force, and applied voltage (equation (20)).

$$\int_0^f \frac{dC}{C^n} = \frac{v}{\zeta}\int_0^V e^{\frac{E_{eff}(F_N,V)}{kT}} dV \tag{20}$$

For a first order reaction, Eqn 14 can be integrated with respect to V, where taking the logarithm twice results in a linear relationship between the measured friction curve and the applied voltage.

$$\ln(-\ln\rrbracket(1-\mathrm{C})\big) = Q_1 + Q_2 V \tag{21}$$

$$Q\_1 = \ln(-\left(\frac{ART}{\zeta\alpha(F_N,V)n_e F_c}\right) - \frac{E_a - \psi(F_N)}{RT} \tag{22}$$

$$Q_2 = -\left(\frac{\alpha(F_N,V)n_e F_c}{RT}\right) \tag{23}$$

Plotting $\ln(-\ln(1-\mathrm{C}))$ against V results in a straight line with slope Q_2 and intercept Q_1. From equations (21),(22) and (23), by substituting known constants, the values of effective symmetry factor (α) and effective activation barrier (E_{eff}) can be obtained from an experimental voltage ramp curve performed at a known applied load F_N. Thus, this modified non-isothermal kinetics allows for determination of the dependence

of the activation barrier and the relative slopes of the forward and reverse reactions as a function of applied voltage, temperature and force.

Figures

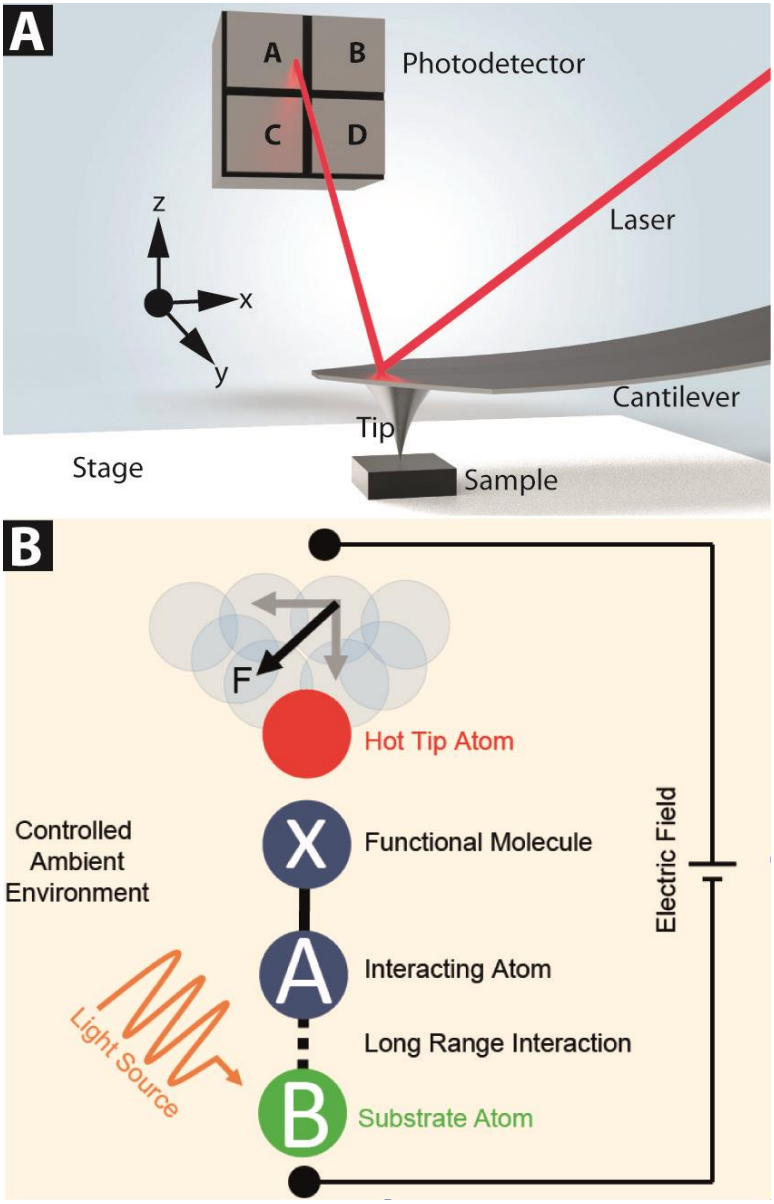

Figure 1: A) Schematic of an Atomic Force Microscope (AFM). B) AFM as a nano-reactor.

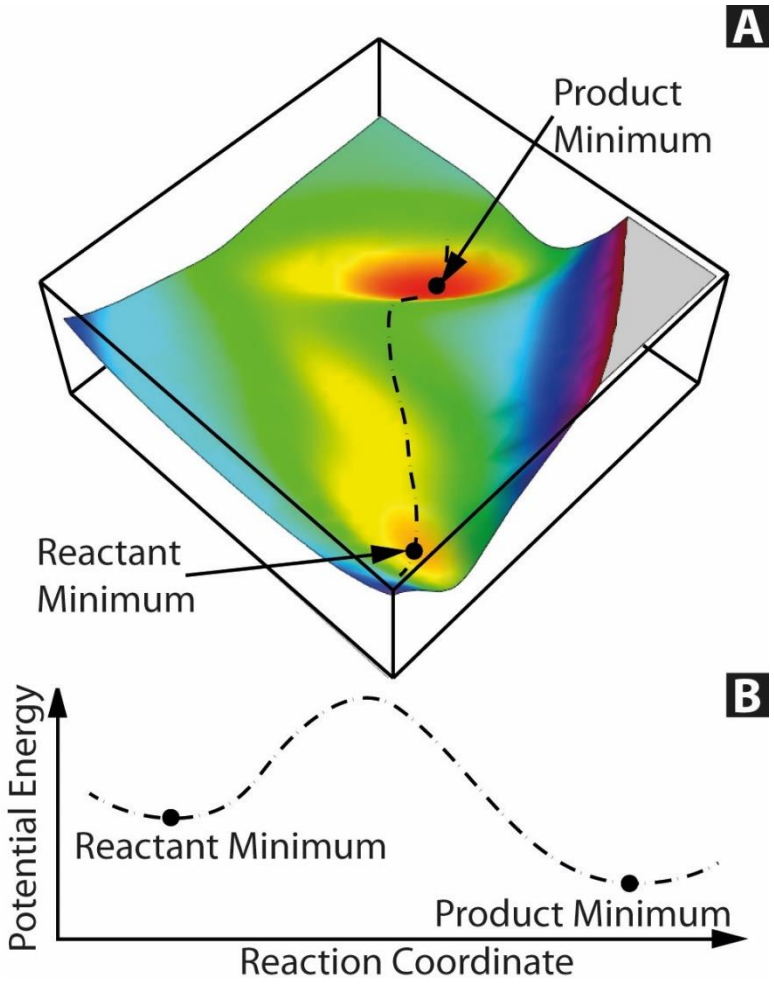

Figure 2: A) Illustration of a Potential Energy Surface (PES). Red line shows the minimum energy path or the "reaction pathway" B) Looking through the reaction pathway for the transformation from reactant to product A, a one-dimensional reaction coordinate profile can be obtained.

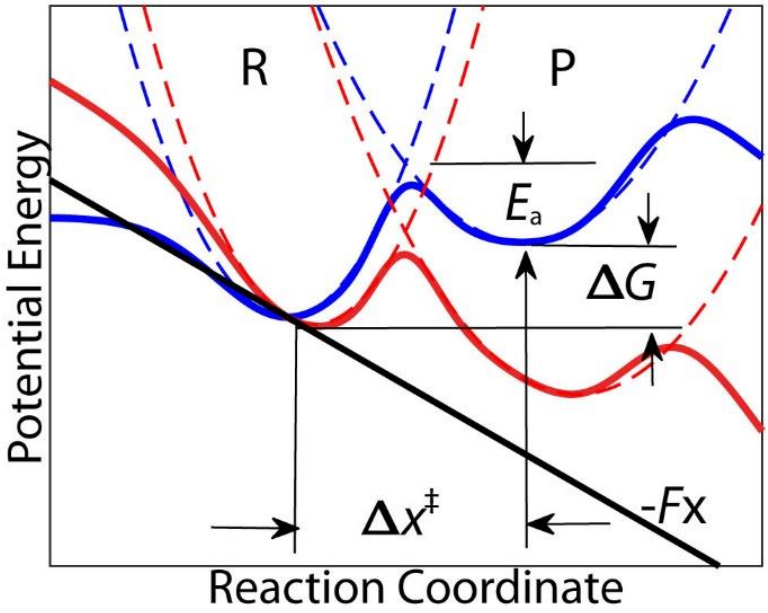

Figure 3: Illustration of tilted PES model. The blue curves represent the energy profile for a reaction unmodified by force or voltage. Introducing a Force term in the energy descriptions (solid black line) tilts the potential as shown by the red curves.

CHAPTER II

DRIVING SURFACE CHEMISTRY AT THE NANOMETER SCALE USING LOCALIZED HEAT AND STRESS*

Introduction

Surface properties influence many chemical and biological processes that hold the key to fundamental advancements in diverse fields such as energy storage and conversion[27-29], 2D optoelectronics[30, 31], friction and wear modification and mitigation[32, 33], wetting and self-assembly[34], medicine[35-37] and nanofabrication[38, 39]. The chemical reactivity of many surfaces in a specific process often depends on multiple factors, including local surface geometry and composition, environmental composition, temperature, pressure, and any additional external stimuli, such as light and electric field. Developing a comprehensive understanding of how to drive and measure surface reactions at the nanometer scale under a wide range of conditions is crucial for development of more efficient chemical reactors, fuel cells, batteries and supercapacitors, flexible electronics, lubricants and biomaterials[40-46].

Presently, Atomic Force Microscopy (AFM) techniques have gained prominence in studying nanoscale surface chemistry and structures owing to their ultra-high resolution in ambient air or liquid. Functional AFM tips can drive adsorption and desorption from surfaces in a wide range of environments via local application of electric field, light, temperature, and force. AFM tips have previously demonstrated oxide growth and

*Reprinted with permission from "Driving Surface Chemistry at the Nanometer Scale Using Localized Heat and Stress" by Raghuraman, S., Elinski, M.B., Batteas, J.D. and Felts, 2017. *Nano Letters*, 17(4), 2111-2117, Copyright [2017] by American Chemical Society

reduction, deposition of self-assembled monolayers, thermochemical modification and phase change in organic films, optical lithography, and thermal deposition of polymers, metals, and composites[47-51].

While AFM proves well suited to drive small-scale surface reactions, obtaining quantitative, *in situ* information on the kinetics and thermodynamics of surface reactions remains a significant challenge [52, 53]. Recent studies of atomic scale wear have begun to directly measure reaction rates of the wear process of both sliding asperity and the counter surface[54]. The results show great promise in using AFM tips to drive and measure chemical reactions. However, it is difficult to interpret the results in the context of conventional chemical kinetic and thermodynamic descriptions, which rely on measures of surface concentration as a function of time and temperature in the absence of an applied load. There is a need to develop tip-based techniques that can directly assess chemical kinetics and thermodynamics at surfaces *in situ*, making it possible to measure reactions driven by arbitrary multi-physical sources in virtually any environment and interpret results in the context of conventional surface analysis techniques.

Methods

Material Preparation: GO/H2O was purchased from Sigma-Aldrich. The dispersion was further diluted in deionized H2O to obtain 0.5mg/ml solution. Single layered GO flakes on SiO2 were obtained by spin coating the solution at 4000 rpm for 120s.

Experimental Setup: AFM experiments were performed using an Asylum Research MFP-3D. A closed-cell heater was used to maintain an ambient temperature of

32 °C throughout the AFM experiments. Heated atomic force microscope tips were used to perform all the local reduction experiments. A relationship between the cantilever vertical deflection and tip force was obtained using force distance curves and thermomechanical noise measurements[55]. These relationships were used to calculate the deflection voltage necessary to apply a specified force. The raw data collected from the experiments were pull-off force and relative friction as a function of tip force, cantilever temperature and scans. The details of the experiments are described in the supporting information.

Experimental Procedure

Here we measure the kinetics and thermodynamics of oxygen group desorption from graphene oxide in ambient air by independently tuning both the force and temperature of a heated atomic force microscope (AFM) probe[56]. The AFM probe is single crystalline silicon with high-doped legs for efficient charge transfer, and a low-doped resistive Joule heater-thermometer at the cantilever free end. The tip is heated by applying a voltage across the legs of the cantilever. The heater electrical resistivity is a strong function of temperature, making it possible to measure and control heater temperatures *in situ* by correlating resistance to temperature *via* optical measurements. Raman thermometry was used to calibrate the heater temperature as a function of applied voltage[57]. The heater operates routinely from 20-800 ˚C with temperature resolutions better than 1˚C[58]. Placing the hot tip onto a substrate forms a nanometer scale hotspot used here to drive local reduction of graphene oxide.

Heated probes have previously demonstrated direct writing of conductive nanoribbons on GO sheets through local thermal reduction [48]. Figure 4(a) illustrates the experimental setup, where a heated tip locally cleaves oxygen groups from a graphene oxide (GO) sheet *via* the application of both temperature and force. Previous AFM mechano-chemistry studies on functionalized graphene show that measured friction linearly relates to the chemical composition at the surface, and that the GO sheet can be reduced solely through applied force [59]. Specifically, oxygenated graphene has two to nine times higher friction than pristine graphene [60, 61]. Accordingly, friction force images of thermochemically fabricated lithographic features reveals sub 100 nm low friction lines as shown in Figure 4(b). Measuring the friction of the lithographic features relative to surrounding unmodified GO (Figure 4(c)), termed "relative friction," provides a measure of the extent of reduction. We employed a two-step routine to cleave oxygen groups and monitor the resulting change in relative friction. First, a 250 x 250 nm2 "drive scan" (Figure 5(a)), with a heater temperature and tip force dictated by the experimental conditions, cleaves oxygen. A subsequent 625 x 625 nm2 "measure scan" (Figure 5(b)), with the heater at room temperature and 40 nN tip load for all the experiments in this study, monitors the friction change. The average of friction values in the drive scan area (indicated in blue) relative to the adjacent unmodified GO region (indicated in red) constitutes a relative friction datum. Repeating this routine several times in the same scan area to obtain a series of images shown in Figure 5(c) - and thereby a relative friction datum from each image – effectively tracks the concentration of functional groups on the surface. Thus, measuring chemical kinetics with the same AFM tip that drives a chemical

reaction enables *in situ* characterization of the evolving surface composition and quantitative understanding of the combined effect of heat and stress on a chemical reaction driven locally at the surface.

Results

Thermodynamics of oxygen removal from graphene was first studied by measuring the kinetics of reduction driven by the tip at various constant temperatures. Figure 6(a) shows changes in relative friction for constant tip temperatures between 300-375 ˚C as a function of cumulative tip dwell time. Recall that for isothermal kinetics, the concentration as a function of time is given by equation(13). As our two-step routine is an intermittent reduction procedure with multiple passes, the total reaction time i.e. cumulative tip dwell time (*t*) is the total time the tip spends at any scan point over multiple scans spanning an entire reduction process. This was calculated as,

$$t = 4N_s \frac{\pi a^2}{vp} \tag{24}$$

where, N_s is the number of AFM image scans, v is the velocity of the tip and p is the pitch between scan lines. The tip radius a is measured by scanning a line on GO as shown in Figure 4(c) and fitting a Gaussian curve. Contact radius is then estimated from the full-width-half-max (FWHM) of the gaussian fit. A factor of 2 is included to account for the trace and retrace scan of the AFM. For all the data, $v = 12$ μm s^{-1} and $p = 0.9766$ nm. Figure 6(b) plots the fitted reaction rates as a function of tip temperature, showing a strong exponential dependence. This thermally activated process was fit using the classical Arrhenius activation model in equation(11). Applying this to the data as shown in figure 2B inset, the slope of the straight line yielded an activation energy of 0.7 ± 0.3 eV, which

compares reasonably well to previous AFM mechanochemistry measurements[59]. Although the activation energy measured here compares reasonably to some previous experimental and theoretical works, the broad error in the activation energy resulting from uncertainty in the exponential fits, and an assumption of a first order reaction prevent any definitive conclusion regarding the chemical reactions under investigation. Gathering additional isothermal datasets for longer dwell times to bring down the measurement error would require prohibitively large amounts of data and an accordingly large sampling area, thereby making the experiment practically impossible. This necessitates an experiment compact in both time and sampling area to reduce the measurement error significantly.

To overcome the limitations of the isothermal approach, we developed a non-isothermal, nanoscale thermal desorption microscopy (ThDM) technique to quickly measure the temperature dependence of reaction rate during a tip temperature or force ramp, using principles from bulk thermal analysis techniques such as thermogravimetry and temperature programmed desorption[25]. Linearly increasing either the tip temperature or the tip force between each scan provides a measure of the reaction rate as a function of either tip temperature, force, or both. Figure 7(A) shows change in friction as a function of temperature for different tip heating rates, determined by dividing the temperature increase per scan (ΔT) by the tip dwell time per scan (equation(25)). The effective ramp rates of 190, 380, 760 and 1500 ºC/min correspond to scan rates of 1, 2.5, 10 and 20 Hz, respectively

$$\beta = \frac{\Delta T}{\frac{t}{N_s}} \tag{25}$$

The friction data obtained were normalized for the purpose of analyses throughout this study. Error in relative friction measurements that arose from surface topography and thermal noise was consistently within ±3% for all the experimental data in this study. Friction profiles obtained for 190, 380, 760 and 1500 ºC/min effective ramp rates show that the thermochemical reduction occurred between 50 ˚C and 450 ˚C heater temperature, whereas, ramping beyond 450 ˚C did not cause any appreciable further reduction in the relative friction. The derivative of the decomposition curve as shown in Figure 7(b) provides the rate of removal as a function of temperature.

The rate of change of oxygen concentration during a linear temperature ramp is governed by equation (14)[26]. The order of the reaction was estimated to be 1 by plotting the ln(Q) against 1/T as in equation(15)-(16). Applying this technique to the data in Figure 7(a) yielded an activation energy of 0.62 ± 0.07 eV with a reaction order of 1 (Figure 7(c)). The nano-ThDM technique reduced the error in the activation energy by a factor of 4, requiring far less data than the isothermal technique, and allowed direct determination of reaction order from the experimental data.

The ability to independently control applied localized temperature and force provides an effective means to quantitatively study the impact of force on the observed energy barrier E_{eff}. Figure 8(a) shows friction measured during linear temperature ramps from 50 ºC to 450 ºC for various tip loads between 40-320 nN. Increasing the load spreads the reaction over a wider temperature range as illustrated by the growing peak width of the derivative curves in Figure 8(b). Activation energies calculated by applying

equation(15)-(16) for decomposition curves as shown in Figure 8(c) decreased from 0.61 eV to 0.22 eV over a force range of 40-320 nN applied tip load, clearly demonstrating that the applied stress substantially modifies the activation barrier.

The influence of applied load on observed activation barrier as shown in Figure 8(c) provides a basis to adopt an explicit mathematical form for the function $\psi(F_{\mathrm{N}})$ in equation(6). A number of theoretical models describe stress assisted chemical reactions. The Zhurkov model[62], originally developed to model fracture events, proposes a linear reduction of the activation energy in response to an applied stress over some activation volume. The model has been used previously to describe atomic wear at tip-substrate interface in AFM scanning experiments, clearly showing an exponential dependence between the observed reaction rates and the applied stress.

$$\Delta E\_\mathrm{Bell} = \Delta E(\psi(F\_\mathrm{N}) = 0) - \psi(F\_\mathrm{N})), \qquad \text{where } \psi(F_{\mathrm{N}}) = F_{\mathrm{N}}\Delta x \tag{26}$$

Bell's theory in equation(26) [63] proposes a similar linear dependence between applied load and activation barrier, but in terms of an applied force over some reaction coordinate (x), where Δx is the distance between reactant and transition state configurations and ΔE is the activation energy barrier when no external force is applied. This model has been used to interpret the forces required to break chemical bonds and the change between reactant and transition states in single molecule pulling experiments[64, 65]. Unlike single molecule experiments, where a known load is applied to a single known bond, here it is difficult to relate the applied load on the tip to the loads applied to each molecule under

the tip, but these two models are directly related with appropriate choice of contact mechanics model between tip and substrate.

Many studies have shown the failure of linear dependence suggested by Bell's model[22, 66, 67]. Bell's model relies on an implicit assumption that the applied force does not distort the potential energy landscape and does not change the reactant or transition state structures. A study on disrotatory and conrotatory ring opening of *cis*-1,2-dimethyl-benzocyclobutene (BCB) demonstrates that the Bell's model fails to capture the non-linear stress dependence and disappearance of reaction pathway beyond a certain applied force[21]. A similar study on BCB shows that including higher order terms in Bell's approximation accounts for the non-linear stress dependence[68]. An experimental study demonstrates rupture of Carbon-Carbon bonds at forces of ~2 nN, whereas theoretical studies show that the maximum force required to rupture a C-C bond is about 6 nN, possibly indicating a modified reaction pathway[11].

Further, as our observations (fig. 4C) point to a non-linear stress dependence of activation barrier, we adopt an extension of Bell's model that includes second order correction[68]. Including this correction yields an expression for the effect of force as in equation(9) which was derived by assuming parabolic interaction potentials for the reacting species. Data in fig 4C fits well with a second order polynomial revealing a non-linear decrease in force dependence of activation. This phenomenon is commonly known as the Hammond effect, where increased applied force shifts the energy levels of the reactant state and transition state, thereby altering the minimum reaction trajectory through the transition state and reducing the force dependence of activation barrier. [19, 69].

The dependence of a chemical reaction to applied load was further assessed by monitoring the decomposition of oxygen groups as a function of increasing force. Figure 9(a) shows relative Friction profiles as a function of linearly ramped force for 50, 100, 150, 200, and 250 ºC heater temperatures. Figure 9(c)-inset illustrates the non-linear rate dependence of activation energy. A molecular system with no change in mechanical compliance following Bell's model would exhibit a linear rate dependence on applied load. On the contrary, including the Hammond effect in the definition of $\psi(F_{\mathrm{N}})$ results in a non-linear plot indicated by the red curve, which is again consistent with the data in Figure 8(c).

Conclusion

The chemical kinetics and thermodynamics observed here differ significantly from previous bulk thermal reduction studies on graphene oxide which suggest a second order recombination reaction with an activation energy in excess of 1.3 eV[70, 71]. The observed activation barrier of 0.62 eV is much closer to theoretical estimations of oxygen diffusion on graphene and silicon oxide[72, 73], suggesting oxygen groups diffuse along either surface or hop between surfaces. The measured first order reaction further suggests diffusion or hopping. This is consistent with previous investigations of the stability of graphene oxide films, which found reduction was largely driven by diffusion (indeed, they must diffuse before they can recombine), with energy barriers of 0.81 and 0.35 eV for epoxides and hydroxyls, respectively[74]. Finally, non-linear stress dependence of activation energy suggests that higher loads increase stability of the oxygen groups.

During sliding, thin graphene sheets undergo out of plane deformation[75] forming a convex region around the periphery of the tip, where atoms bound are more stable[76].

In summary, we have demonstrated that nano-ThDM is an effective approach to measure the kinetics of surface chemical reactions and to precisely tune the surface composition. Varying the tip material, functional group to be cleaved, environmental composition, and substrate material would provide chemical kinetics of virtually any rubbing interface, and appropriate passivation of the tip material would allow the tip to observe the reaction without significantly altering the reaction pathway. Incorporating both molecular dynamics simulations, and *in situ* electron microscopies will provide a more complete picture of the stoichiometric products, reaction pathway of the observed reactions, and more accurate contact mechanics with atomic resolution. Importantly, this technique has few limits on environmental conditions, making it ideal to study multi-physical reactions in extreme environments, closely resembling operation of real chemical systems.

Figures

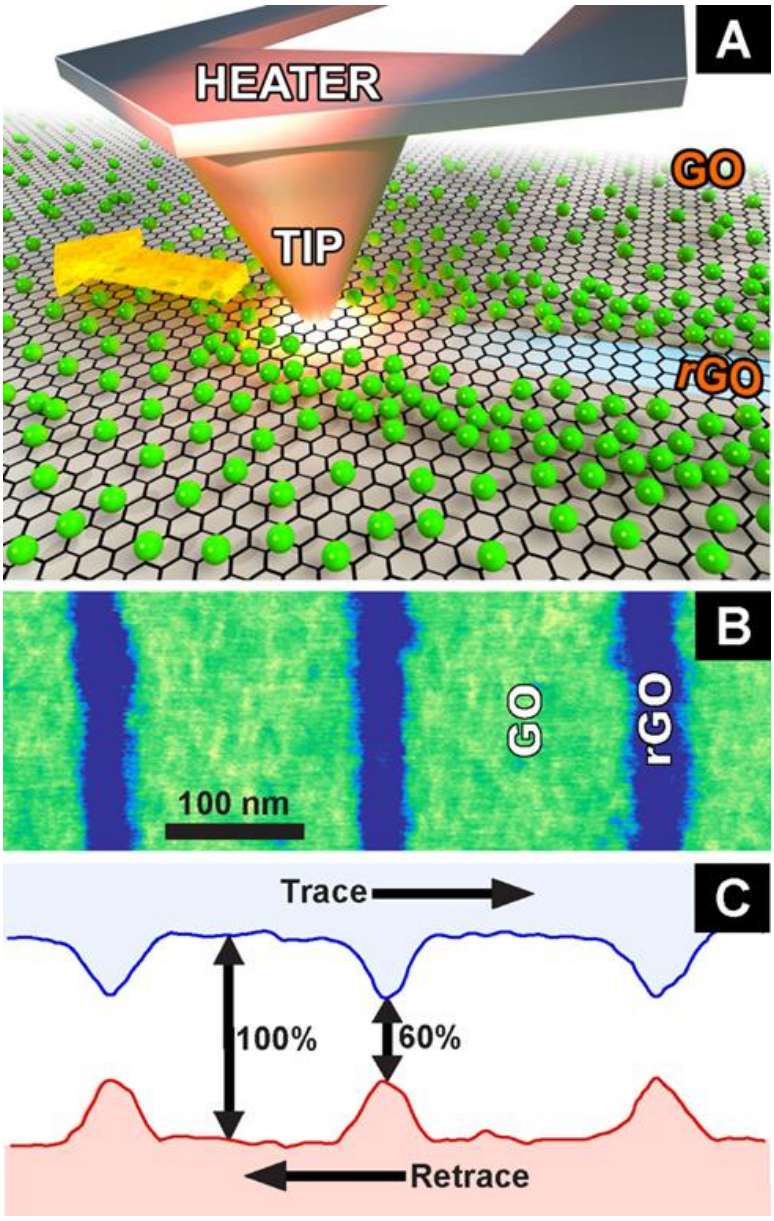

Figure 4: A) Schematic of reduction by a hot AFM tip, where heat and pressure locally remove oxygen groups. B) Friction Force image of the reduced graphene oxide patterns. C) A friction drop of 60% due to removal of oxygen groups.

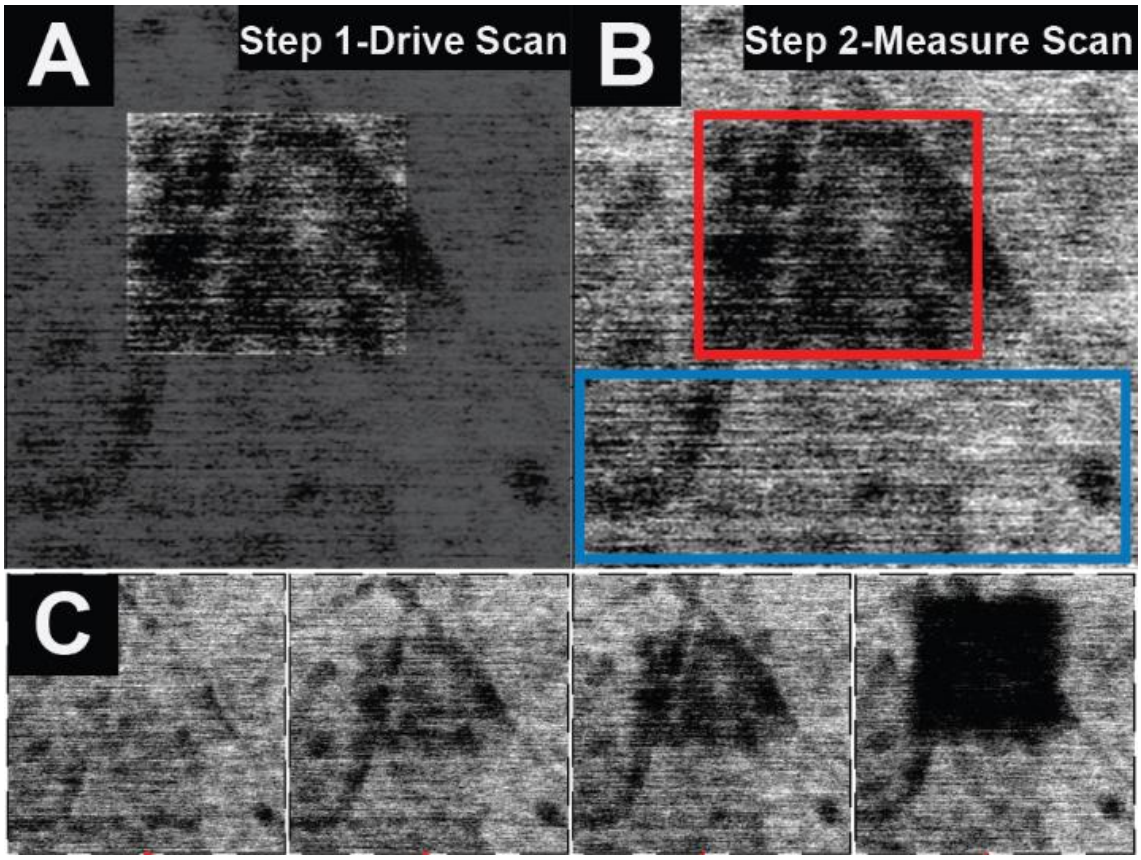

Figure 5: A) 250x250 nm2 drive scan to cleave oxygen. B) 625 x 625 nm2 measure scan to measure the friction change. Red box indicates the thermochemically modified area. Blue box indicates the surrounding un-modified area C) Selected images from a series of images taken at the same scan area shown to represent the progress of thermochemical reduction.

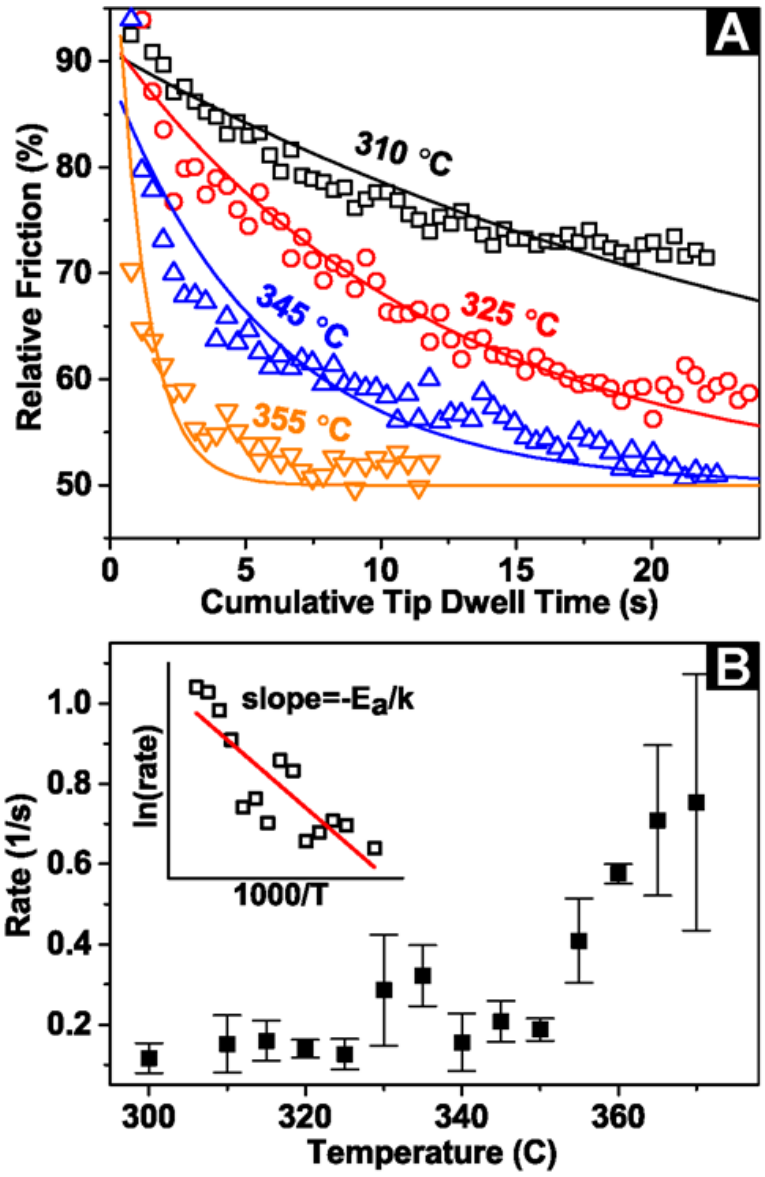

Figure 6: 2 A) Relative Friction drop as a function of cumulative tip dwell time for various cantilever temperatures. The friction data obtained were normalized for the purpose of analyses. B) Reaction rate as a function of temperature - inset shows the Arrhenius plot. The friction data obtained were normalized for the purpose of analyses.

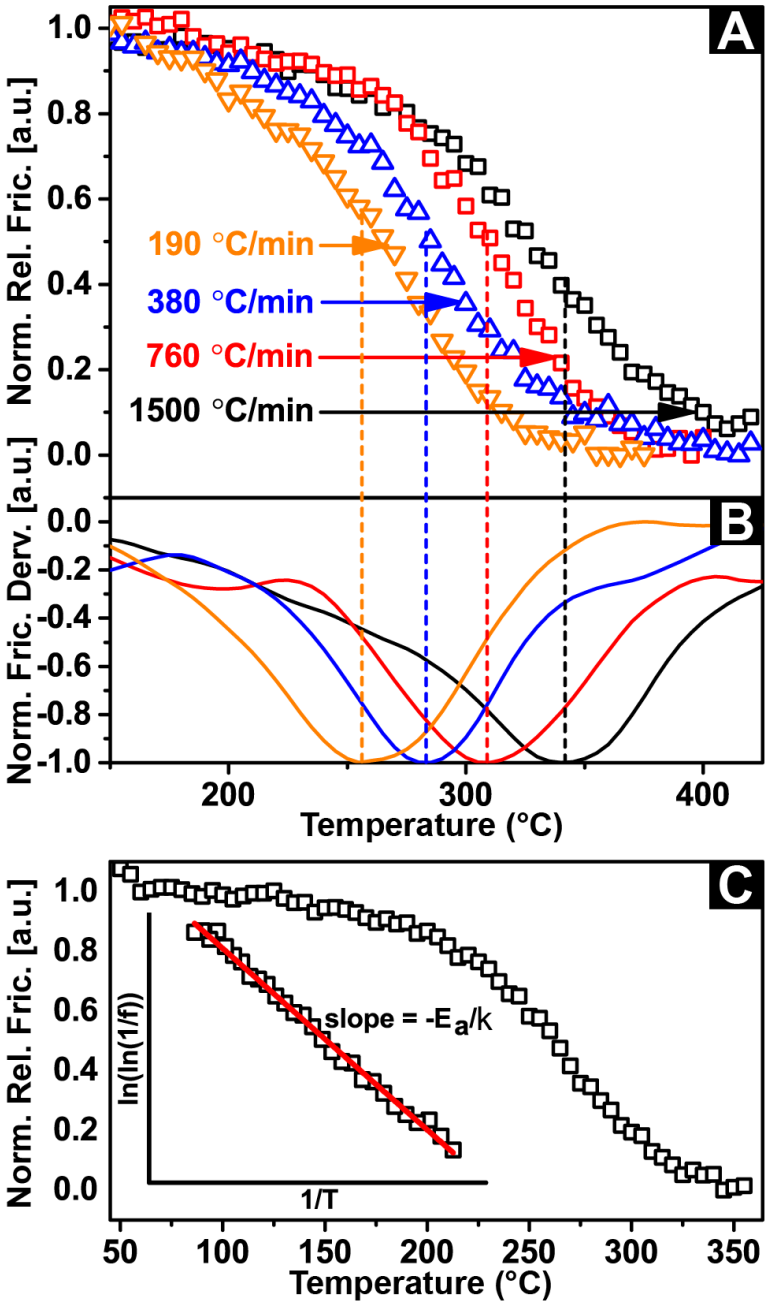

Figure 7: A) Normalized Relative friction drop as a function of cantilever temperature for various ramp rates. The friction data obtained were normalized for the purpose of analyses. B) Normalized relative friction derivative showing a rightward shift in maximum removal with increasing ramp rates. C) A typical constant heating rate curve – inset illustrates the calculation of activation energy.

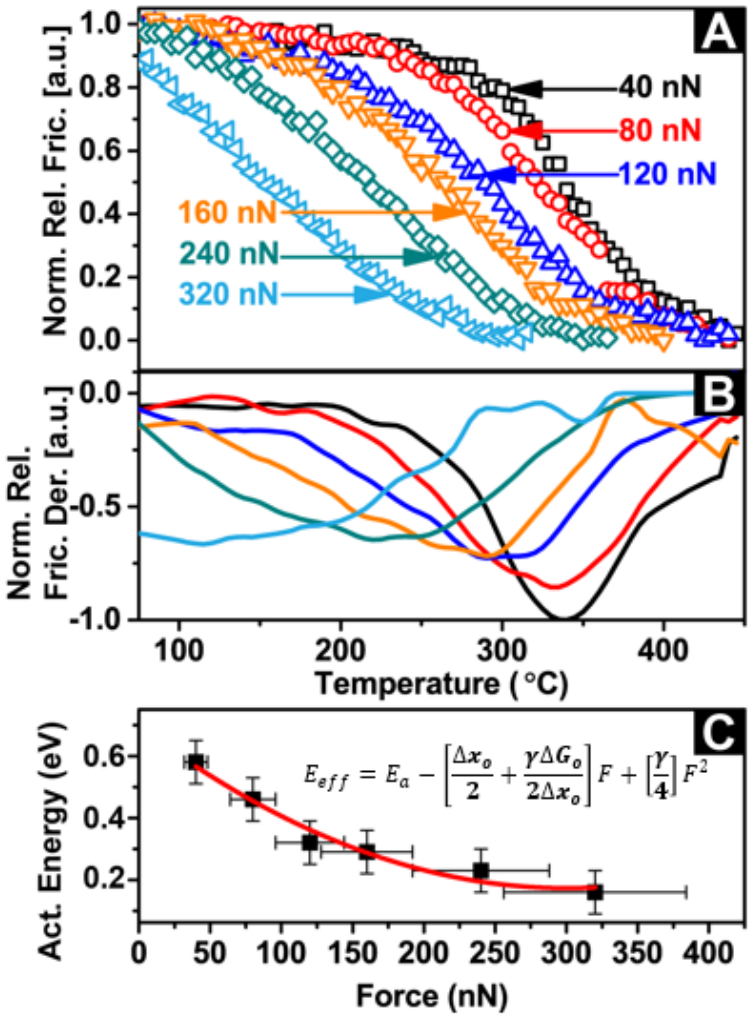

Figure 8: A) 760 °C/min constant heating rate curves for various tip forces. The friction data obtained were normalized for the purpose of analyses. B) Normalized relative friction derivative showing a shift in maximum removal towards lower temperatures for increasing tip force C) Measured activation energy as a function of tip force, showing a non-linear reduction with increasing force.

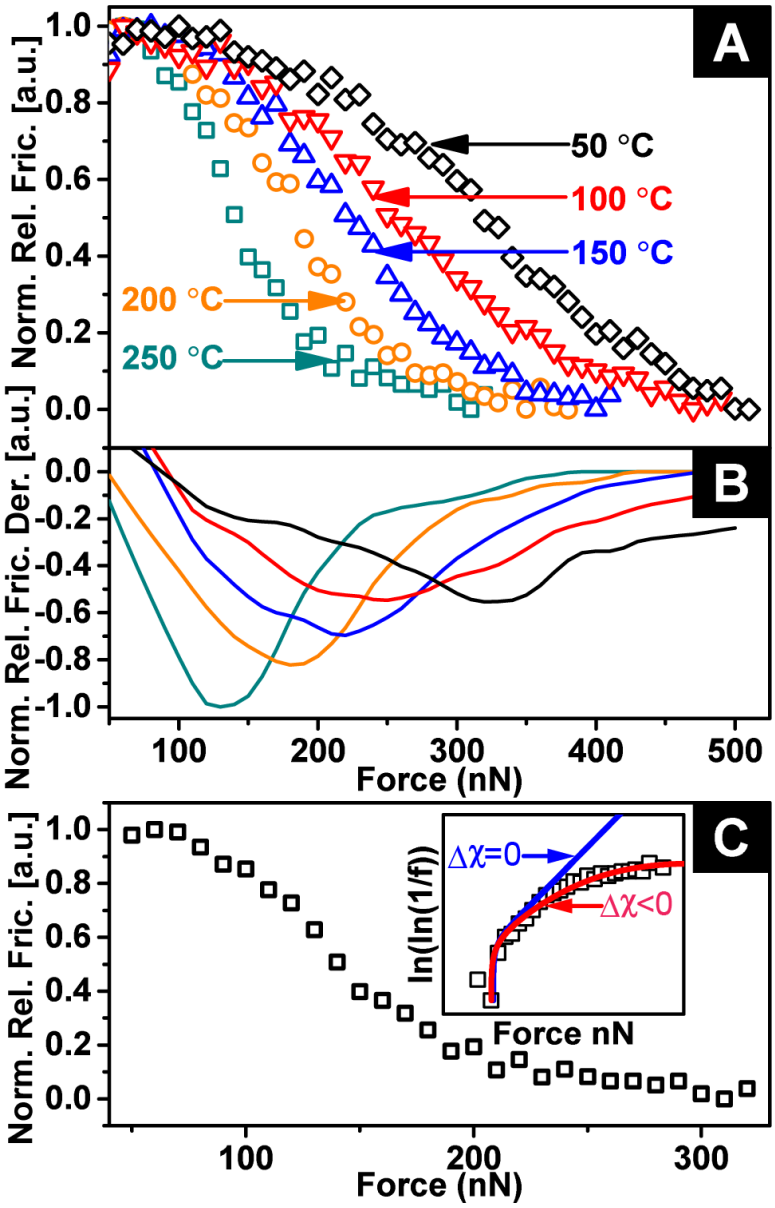

Figure 9: A) Normalized Relative friction drop as a function of tip force while a constant cantilever temperature was maintained. The friction data obtained were normalized for the purpose of analyses. B) Normalized relative friction derivative showing a shift in maximum removal towards lower forces for higher temperatures. C) A typical linear force ramp curve with inset illustrating the failure of Bell's model.

CHAPTER III

THE ROLE OF MECHANICAL FORCE ON KINETICS AND DYNAMICS OF ELECTROCHEMICAL REDOX REACTIONS ON GRAPHENE*

Introduction

Electrochemical reactions form the basis of many important processes both naturally occurring—such as photosynthesis and corrosion—and those explored in the fields of energy storage and conversion, chemical separations, and electroplating[77-80]. Electrochemical reactions are surface reactions with rates depending on the electronic state of the interacting surface atoms, which can be strongly modulated by the applied stress, strain and chemical composition of the participating surface[81, 82]. Improved understanding of the complex interplay between surface chemistry and mechanics would enable rational design and synthesis of surface structure with prescribed morphology to greatly enhance electrochemical reaction rates. Although several techniques exist that measure electrode kinetics at the atomic scale, the reactions are traditionally driven by macroscale stimuli, making it difficult to capture nanometer scale mechano-chemical effects[83]. There is a need to develop tools and techniques that can relate locally applied stress, strain, and chemical composition to reaction rates on a well-defined surface structure to understand the relationship between stress and electrochemical reactivity.

---

*Reprinted with permission from "The Role of Mechanical Force on the Kinetics and Dynamics of Electrochemical Redox Reactions on Graphene" by Raghuraman, S., Soleymaniha, M., Ye, Z. and Felts, J.R., 2018. *Nanoscale*, 10(37), 17912-17923, Copyright [2018] by The Royal Society of Chemistry.

Atomic force microscopes (AFMs) have been used to measure and drive a number of chemical processes *in situ*, providing insight into local electron densities of adsorbed surface intermediates, and local electrochemical kinetics[84-91]. Most of these measurement techniques, such as non-contact atomic force microscopy (NC-AFM)[92-94] and scanning electrochemical microscopy (SECM)[95-97], take measurements some distance away from the surface, making it difficult to simultaneously measure chemical reactivity and local stress/strain. Electrochemical strain microscopy (ESM) uses measurements of local surface strain under global bias to measure the rate of ion transport into a surface, providing a relationship between surface morphology and reactivity, but it remains difficult to determine how applied strain modifies the reactivity of the surface[98, 99]. Recent *in situ* studies of steel corrosion have begun to qualitatively investigate the role of applied stress on the corrosion rate[80]. Interestingly, it is possible to locally drive oxygen or hydrogen adsorption with a conductive AFM tip in contact with a surface, which has been routinely demonstrated for semiconducting and conducting materials, making it an ideal platform to study the relationship between electrochemical reactivity and applied local strain [47, 100]. However, to date these studies are merely qualitative, and disregard the influence of applied force on electrochemical reaction rates, despite recent work showing that applied force has a profound effect on reaction kinetics[11, 19-21, 56, 101, 102].

Here, we investigate the effect of applied force on the kinetics of surface oxidation using a conductive AFM tip sliding on a graphene surface[103]. Atomic

force microscope tips can localize the oxygen evolution reaction (OER) within the contact between the tip and the sample by the formation of a microscopic water meniscus at the tip contact[104]. Applying a voltage bias between tip and sample splits water, where hydrogen atoms and oxyanions drift towards oppositely charged surfaces as shown in Figure 10(a). The tip-surface voltage can be tuned to achieve a narrow electric field distribution under the tip apex, resulting in oxide features (Figure 10(c), (d) and (e)) with thickness ranging between 10 nm and 30 nm. We introduce mechanical force as a significant modifier of electrode kinetics and provide an explicit mathematical form for the rate of an electro-mechano-chemical reaction. We devise a compact experiment to measure the kinetic parameters of the oxidation. Results show that applied force can significantly enhance or suppress the forward and/or backward reaction. The effect of load on the observed electrochemical kinetics is discussed in the context of transition state theories of mechanochemical reactions.

Methods

Sample Preparation: Silicon <100> substrates were coated with 100 nm nickel using e-beam evaporation. Thick graphene flakes (>10 layers) were obtained by exfoliating highly ordered pyrolytic graphite using a modified scotch tape method.[105] Spring metal clips were used to mount and make electrical contact with the substrate. AFM experiments were performed using an Asylum Research MFP-3D. A PEEK cantilever clip fabricated with copper wire was used to mount a platinum coated Silicon tip with electrical

contact. A Keithley 2400 source meter was used to control the voltage bias between the tip and sample.

Molecular Dynamics Simulations: The fully atomistic model consisted of the apex of a platinum AFM tip placed on a five-layer graphene surface, illustrate in Fig 7. The graphene substrate had dimensions of 10x10 nm2; the bottom layer of graphene is fixed. A model tip was constructed in a hemispherical geometry with a 2.5 nm radius, and 2.5 nm height; the topmost atoms in the tip were treated as a rigid body under a constant load and connected by a harmonic spring to a support that moved laterally at a constant speed of 1 m/s. The spring had stiffness of 8 N/m in the horizontal directions. A Langevin thermostat was applied to the free atoms maintained a temperature of 300 K. The simulations were performed using LAMMPS simulation software.

Finite Element Simulations: Quasi-static axisymmetric model was used in ABAQUS/Explicit to model the AFM tip and graphene interactions. Tip was modeled as half sphere rigid body with radius of 30 nm and was placed at 0.530 nm above the top-most graphene layer. Double layer graphene sheet with thickness of 0.07 nm with equilibrium separation of 0.33 nm is placed on rigid body silicon oxide substrate. For substrate and tip, element types RAX2 of and for graphene sheets CAX4R element type was selected. Interactions between graphene layers, tip/graphene and substrate/graphene were modeled by Lenard-Jones (L-J) potential in VUINTER subroutine. Simulations were done in displacement-controlled regime by moving the tip either 0.1 nm up or 0.1nm, 0.2 nm, 0.3 nm, 0.4 nm, 0.530 nm and 0.580 nm down. Young modulus and Poisson's ratio

of the graphene were selected as 5.5 TPa and 0.3, respectively. It was assumed that the graphene deformation was purely elastic and the contact is frictionless.

Experimental Procedure

To understand electrochemical reactions, monitoring faradaic current as a function of applied overpotential is an effective way to measure the reaction rate. In local anodic oxidation experiments, where electrochemical reactions are confined to nanometer scale double layers, the faradaic currents can be on the order of femto-ampere (fA) or lower [106, 107]. It is difficult to measure such low currents in AFM without specialized electronics. Further, it is not possible to measure applied overpotential relative to a standard electrode, as it is not possible to integrate an independent electrode into the microscale water meniscus surrounding the tip.

An alternative measure of charge transfer is the accumulation of oxygen species on the surface. Oxygen evolution during water splitting is a 4e- process involving surface bound intermediates, which depend strongly on solution pH, temperature, applied voltage, and surface catalytic activity. Despite this complexity, the first step is often the chemisorption of -OH onto the anode, followed by the creation of epoxides and/or carboxylic acid before the final formation of O2. Generally, the epoxide and carboxyl formation is the potential determining step (PDS) or rate determining step (RDS). Previous LAO studies on graphene showed that hydroxyl groups are the primary species adsorbed, with significant epoxides occurring only at higher voltages[108]. Therefore, at the onset of surface oxide growth, the concentration of hydroxyls on the surface is proportional to the total number of electrons transferred to the surface over time, where

the derivative is the electron current. Thus, a measure of the evolving hydroxyl concentration on the surface is a proxy for the integral of the electron current over time.

Several studies have shown that friction on functionalized graphene positively correlates to surface concentration in a roughly linear fashion[109, 110]. Measuring friction changes on the surface during a linear voltage sweep can generate a voltammogram by taking the derivative of the friction data. We implemented a two-step routine to measure the friction of the modified surface relative to pristine graphene. First, a "drive scan" (250x250 nm2) with a voltage bias and applied force drives the electrochemical reaction. Then, a subsequent "measure scan" is taken with 5 nN tip load and no applied voltage bias to monitor the extent of surface chemical composition change. Relative friction measurement from one such two-step routine constitutes a single data point of a typical experimental reaction curve like those shown in this work. The routine is repeated until a full reaction curve is obtained.

Figure 11(a) shows friction measured during a cyclic voltammogram. The surface is first cycled between oxygenation and reduction, followed by hydrogenation and dehydrogenation, demonstrating both the change in friction upon surface modification and the reversibility of the process. Figure 11(b) shows the derivative of the friction signal, showing peaks in electronic current upon surface modification, and zero current otherwise (the current may not be zero, however, as a saturated surface does not necessarily imply zero evolution). The magnitude of the current is estimated by assuming saturation at 100% coverage of –OH or –H on a single side of graphene (which represents the total charge Q transferred to the surface), divided by the time between scans. For the one electron transfer

process considered in the study, the total current (I_{Tot}) involved in depositing oxygen over the surface can be calculated as,

$$I_{tot} = e \times \frac{\mathrm{d}n_a}{\mathrm{d}t} \tag{27}$$

where, n_a is the total number of active sites in the given scan area. As a graphene unit cell has 2 carbon atoms accounting for sharing and an area of $0.05\ nm^2$, a scan size of $250\ nm^2$ contains 2,500,500 carbon atoms. However, several studies show that even at a theoretical maximum functionalization of graphene, a significant fraction of the carbon atoms would have functional groups attached. Nevertheless, for a conservative estimate, *n* was assumed to be equal to the number of carbon atoms. The time per scan *t* is 15s and charge of an electron e is $1.6 \times 10^{-19}\ C$. As friction directly correlates to composition, the maximum friction observed can be attributed to a fully oxygenated surface. Accordingly, the current per scan (I_{Scan}) can be calculated as,

$$I_{Scan} = \frac{\Delta f}{f_{\max}} \times I_{tot} \tag{28}$$

where, Δf is the change in friction per scan and f_{max} is the maximum value of friction observed during the reaction. The current in our study was observed to be on the order of a few fA.

Procedure to Obtain Kinetics and Dynamics Parameters

1. The reaction curve obtained by voltage ramps at a given applied tip load (Figure 11(a)) can be described by equation(20). Consequently, using equations (21)-(23), plotting $\ln(-\ln(1-f))$ against V results in a straight line with slope Q_2 and intercept Q_1.

2. The value of symmetry factor, i.e. $\alpha(F_N, V)$, can be obtained from the slope Q2 by substituting known values ($n_e = 1, F_c = 96485.232 \frac{C}{mol}, R = 8.314 \frac{J}{mol.K}$ and $T = 300K$ (room temperatue). The value of $E_a - \psi(F_N)$ can be obtained from intercept Q1 by substituting $\alpha(F_N, V)$ assuming a value for attempt frequency (A=1e13/s) [54, 111]. A voltage ramp rate of ζ =-58.33 V/s was used throughout our work.
3. Using equations(7) and (9), we get equation(29). By fitting equation(29) with a second order polynomial, the stiffness of the potential (γ) can be calculated from the quadratic term.

$$E_a - \psi(F_N) = \left[\frac{\Delta x_o^2}{4\gamma} + \frac{\Delta G_o}{2\gamma^2} + \frac{\Delta G_o^2}{4\Delta x_o^2 \gamma^2}\right] - \left[\frac{\Delta x_o}{2} + \frac{\gamma \Delta G_o}{2\Delta x_o}\right] \boldsymbol{F} - \left[\frac{\gamma}{4}\right] \boldsymbol{F^2} \qquad (29)$$

4. Using equation(10) and fitting a straight line, the value of path length(Δx_o) can be calculated from the slope.
5. As it is not possible to integrate a reference electrode into the localized water meniscus and with the estimated currents being on the order of fA, the overpotential were not measured during the experiments. However, we can fit for the overpotential from the value of standard Gibbs Free Energy Change (ΔG_0) which can be calculated from the first order term of the quadratic fit to eq 13. The standard Gibbs free energy for water splitting has been theoretically and experimentally shown to be around 1.2V. We use this fact to fit for overpotential and estimate a voltage offset of -3.63V. This offset was then propagated into the experimentally applied voltage bias values to obtain the corrected values of the

effective symmetry factor ($\alpha(F_N, V)$) and effective energy barrier ($E_{eff}(F_N, V)$) shown in figures 6b and 6c.

Results

Voltage ramps were performed to study the kinetics of oxidation of graphene as a function of applied force. Monitoring change in friction of oxygenated areas relative to unmodified graphene (relative friction) as a function of applied voltage provided a single cumulative reaction curve during a voltage ramp experiment. Figure 12(a) shows reaction curves at 10, 100, 200, 300 and 700 nN tip load. The magnitude of onset voltage for oxygen deposition decreases with increasing applied load, indicating a strong dependence of oxygenation rate on applied stress. Figure 12(b) shows a sample fit to obtain quantities *Q1*and *Q2* which were used to obtain kinetics and dynamics parameter as discussed in the experimental methods.

Interestingly, unlike previous local anodic oxidation studies on Silicon and Graphene, a glaring non-uniformity in oxygen deposition was observed throughout the experiments, as shown in Figure 13. To investigate this further, images for each cumulative reaction curve (from experiments shown in Figure 12) were divided into 10x10 partitions. Reaction curves were extracted for each partition and $\boldsymbol{\alpha}$ was determined from equation(23). Figure 13(e)-(h) show the $\boldsymbol{\alpha}$ maps for 10, 100, 300 and 700 nN tip loads respectively. At low applied load conditions (Figure 13(e)) when the oxygen deposition should be almost unaffected by force, meaning $\boldsymbol{\alpha \sim 0.5}$, two distinct regimes (blue and red) can be identified with significantly different $\boldsymbol{\alpha}$ values. Correspondingly, a typical reaction curve from each of these regions (Figure 13(a)) show vastly different reaction

rates. This non-uniformity in reaction rate fades with increasing applied load as seen from Figure 13(f)-(h) and their corresponding reaction curves shown in Figure 13(b)-(d).

Topographic inhomogeneity such as wrinkles and other defects cause stress concentration, which enhances the local rate of deposition, and effectively lowers the value of alpha. At low applied loads, such variations show up as a prominent difference in the measured alpha values. Histograms of alpha values (Figure 13(a)) also show two distinct peaks supporting the observation of vastly different reaction rates. At high applied loads however, any rate variation due to topography is weak in comparison to the rate enhancement due to applied force. Applied force sufficiently lowers the barrier for adsorption such that the rates are uniform across the surface. As a result, the deposition over the scan area becomes more uniform with increasing applied load. This can be clearly seen from the histograms (Figure 13(b)-(d) insets) where the two distinct peaks at 0.1 and 0.5 blend into a single peak at 0.1 at high loads.

To obtain an average measure of α and E_{eff}, we chose several reaction curves from the partitions. For low applied forces – 10 and 100 nN – we used histograms to choose curves with higher alpha values, as these regions are the least affected by topography. At high applied loads, the effect of topography was small relative to the effect of applied load, so data from each partition was used. Using equations(21)-(23), the symmetry factor and effective activation barrier were calculated as a function of applied tip load (Figure 14(a) and (b)). Using equations(6)-(9), and experimental results shown in Figure 13, the path length (Δx_o) can be calculated (detailed in above section "Procedure to obtain kinetics and dynamics parameters"). Importantly, the force used in the kinetic

equation is the force per atom, requiring knowledge of how the total force applied to the tip is distributed over the atoms within the nanoscale contact. In general, the force distribution in a nanoscale contact is a complex function of atomic morphology of the tip, substrate and constrained water molecules, which cannot be captured well by macroscopic models of contact. Nevertheless, under the assumption that the contact area is well estimated by the Hertz contact mechanics model, and the force applied within the contact is evenly distributed over the number of graphene atoms in the contact, the calculated path length is 2 orders of magnitude greater than typical C-O bond lengths, suggesting that average force is an inaccurate estimation of force applied to the atoms in the contact. Reasonable values of activation length emerge when assuming that the force applied in the contact is distributed over 1-3% of the number of graphene atoms in the contact (Figure 14(c))

We performed molecular dynamics (MD) simulations of a platinum AFM tip sliding on multi-layered graphene in the presence of a water meniscus to better understand the relationship between total applied load and the force applied to the molecules in the contact (Figure 15(a)). For a tip radius of 2.5 nm and an applied force of 10 nN, the contact radius was estimated from the simulation to be 1 nm (Figure 15(b)). The contact area is then 3.14 nm2, which corresponds to ~156 carbon atoms in contact under the water layer. In the absence of water layer and assuming uniform force dissipation, the average force would be 0.06 nN per carbon atom, which is much weaker than the forces typically required to make or break covalent bonds. However, the simulations reveal that the force is not supported uniformly across the surface. Figure 15(b) shows that the surface density

of water molecules within the contact line is 16 per nm2 whereas the surface density outside is 160 per nm2. Apart from having fewer atoms in contact, the force distribution map in Figure 15(b) shows that around 5% of the water molecules experience a force of 1nN or higher which is typically the magnitude of forces involved in covalent mechanochemistry[21]. Consequently, the number of water molecules experiencing significant forces within the contact is roughly 1-2% the number of graphene atoms in the contact.

The non-uniform force distribution on atoms produced by the MD simulations were taken into account to translate applied tip loads to force applied per atom within the contact. Path length value of 0.47 nm calculated as a function of carbon atoms is reasonable when the tip load is distributed over 1% of the total carbon atoms within the contact, consistent with the result from the MD simulations, whereas the path length quickly becomes an order of magnitude more than a typical covalent bond length when 5% or more of the total atoms present in the contact area are mechanochemically activated (Figure 14(c)). Assuming the tip exerts a force on the water molecules in the contact equivalent to 1% of the total carbon atoms within the contact region, the symmetry factor and the effective energy barrier were calculated as a function of force per atom (Figure 14(b) and (c) inset). Applied force therefore reduces E_{eff} non-linearly and α linearly in accordance with equations(8) and (9) respectively.

The force applied at the contact could also manifest itself as strain in the substrate material, which could be the source of the enhanced reactivity of the graphene. We explored the strain on the graphene lattice due to applied stress using finite element

method (FEM) simulations[112-114]. Here, we considered the effect of both out of plane strain, quantified by the radius of curvature of graphene, and in plane strain due to the stretching of the carbon-carbon lattice. It has been demonstrated previously that adhesion between an AFM tip and graphene causes the graphene sheet to "pucker" out of plane to conform to the tip structure, causing out of plane bending, while application of force in the contact will exert a strain within the graphene basal plane. Considering flat graphene to have an infinite radius of curvature, our results show that increasing applied load decreases the maximum radius of curvature as shown in Figure 16. Recent density functional theory (DFT) calculation of the adsorption of hydroxyls and epoxides onto graphene have shown that a radius of 0.68 nm decreases the activation energy for adsorption only by 0.08 eV, meaning that our larger radius of curvature induced here likely plays a negligible role in the observed reaction[76]. Increasing the applied force induces a 2% strain relative to flat graphene at 200nN with no significant increase at higher forces. Several studies show that such strains of around 2% reduces the activation barrier by about 0.2 eV[115-117]. This suggests that while reactivity may be increased by simply straining the graphene lattice, the effect is unlikely to account for the total observed decrease in activation energy of 0.6 eV. Based on the experimental findings and the simulations, it is hypothesized that the force applied to the water molecules in the contact works in concert with applied electric field to split H2O into a chemisorbed –OH and free H+ that is subsequently converted to molecular hydrogen at the tip surface.

Based on the hypothesis that applied load drives the reactant towards the product state, we interpret the experimental results using the mechanochemical transition state

formalism described above. The qualitative shape of the potential energy profile for force modified electrochemical oxidation of graphene can be calculated from the experimentally observed energy barriers and symmetry factors. The compliance of the potential (γ) was calculated (see above section "Procedure to obtain kinetics and dynamics parameters") for a range of percentage atoms in contact as shown in Figure 17(a). Here, again assuming the number of molecules supporting the tip load as 1% of the number of graphene atoms in the contact, the compliance of the reactant and product states is ~ 1.3 nm/nN. Now, from the starting descriptions of the potential energy profile (equations(3) and (4)) the effect of voltage and the effect of applied force can be individually obtained. For only applied force conditions, the voltage term was excluded (V=0) and potential profiles for 10, 200 and 450 nN are shown in Figure 17(b) with path length corresponding to 1% atoms in contact. Compared to the unmodified potential (Black curve), the qualitative shapes correspond to the tilting effect due to applied force. By tilting the potential, applied force also shifts the reactant minimum and the transition state closer to each other thus reducing the path length. To visualize the effect of applied voltage, the force terms were neglected (F=0) (Figure 17(c)). Applied voltage translates the reactant state relative to the unmodified potential (Black curve).

Conclusion

The theory of force modified electrochemical reactions provided in this work enables decoupling of the force and voltage effect on an electrochemical reaction with a regular AFM set up in ambient air. Force applied directly on the atoms (stress) and strain

of the graphene lattice can affect a chemical reaction in different ways. While it is likely that the applied force dominates chemical kinetics in this study, the effect of strain on chemical kinetics cannot be discarded in general. Further experiments could be devised in combination with first-principles based studies to decouple the effect of stress applied directly to the mechanophore versus strain applied to the surface atoms. Careful comparison between molecular dynamics simulations and experiment can also provide a relationship between the macroscopically applied load and the corresponding forces on the atoms within the nanoscopic contact. This experimental technique has previously been used to study chemical reactions on graphene as a function of temperature, and coupled with the results here provide a compelling framework to study complex, multi-physical activated surface reactions, with an emphasis on the relationship between applied load, local surface morphology and applied temperature and electric field. Such studies would improve our fundamental understanding of how all of these factors work in concert to define the overall macroscopic reactivity of surfaces.

Figures

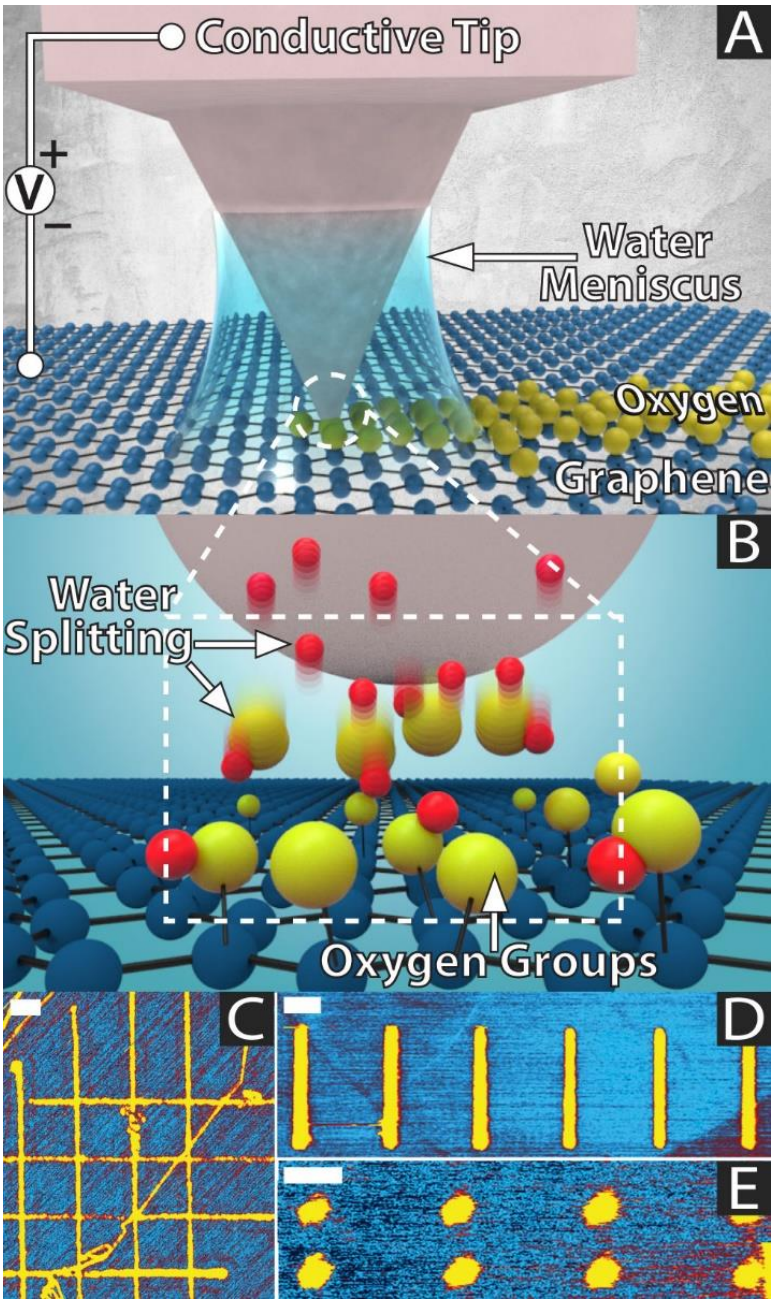

Figure 10: A) Local anodic oxidation – setup. B) Tip-Surface contact showing electric field induced water splitting within the water meniscus. C-E) Oxide features fabricated on graphene as seen in friction images. All scale bars represent 50nm

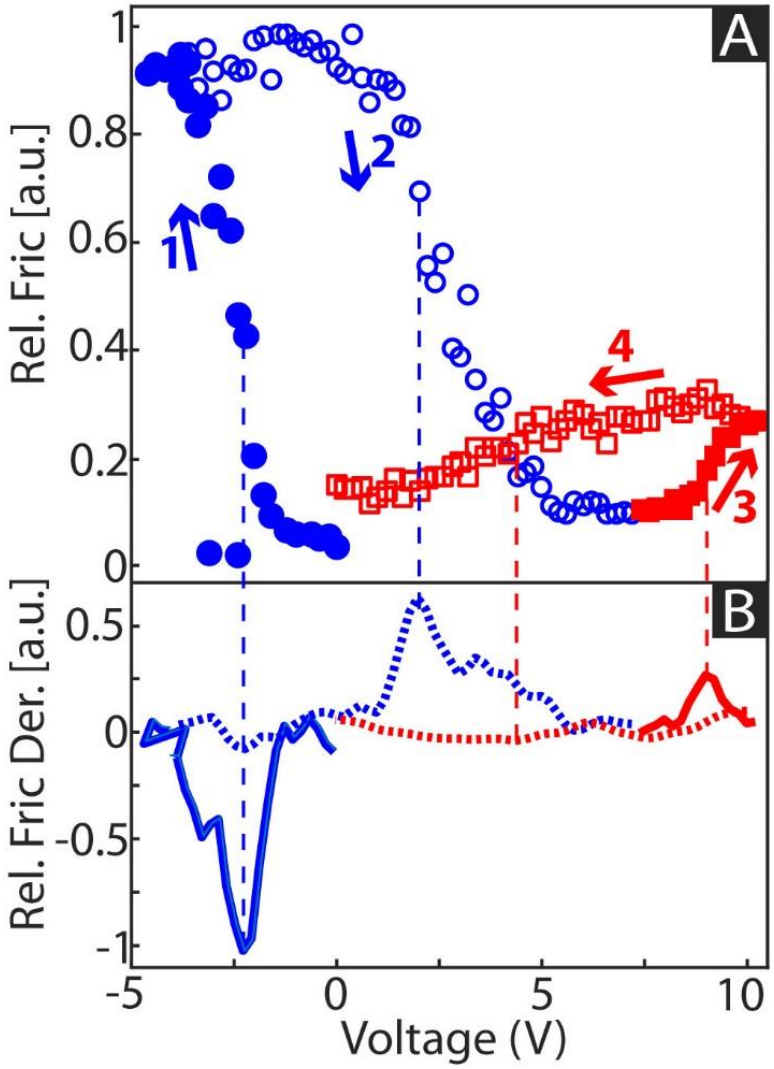

Figure 11: A) Cyclic voltammogram. The surface is cycled first with oxygenation (solid circles), reduction (open circles), hydrogenation (solid boxes) and finally dehydrogenation (open boxes). B) Relative friction derivative.

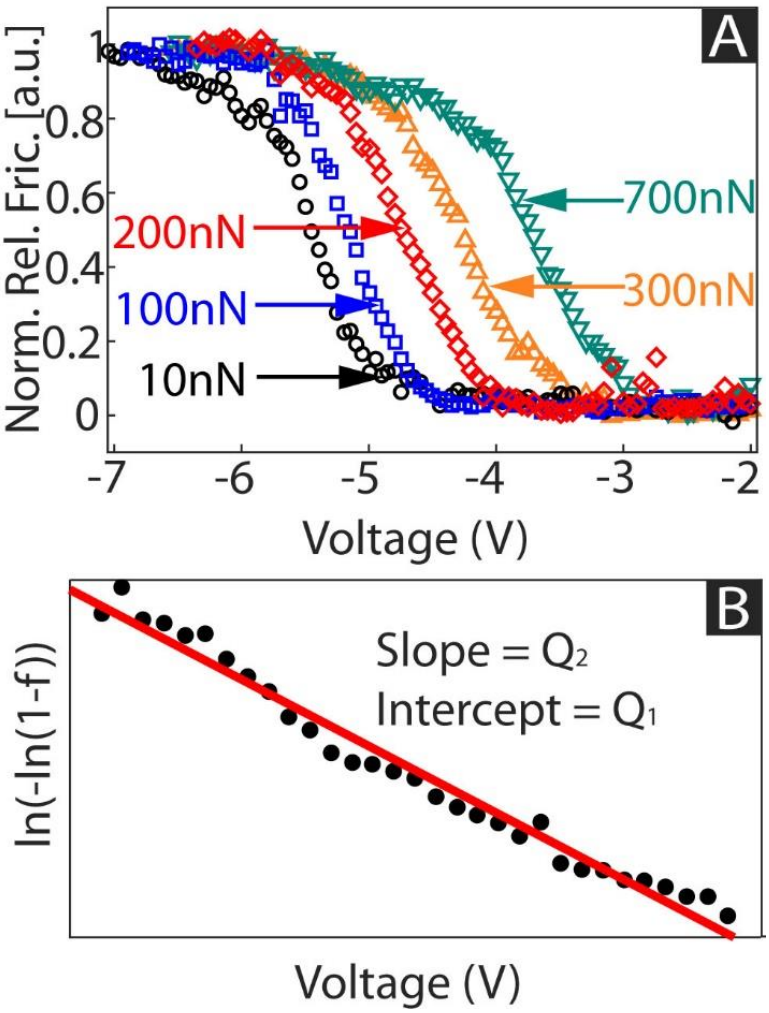

Figure 12: A) Voltage Ramps at 10, 100, 200, 300 and 700 nN applied tip load. B) Curve fitting a voltage ramp curve to obtain kinetic parameters.

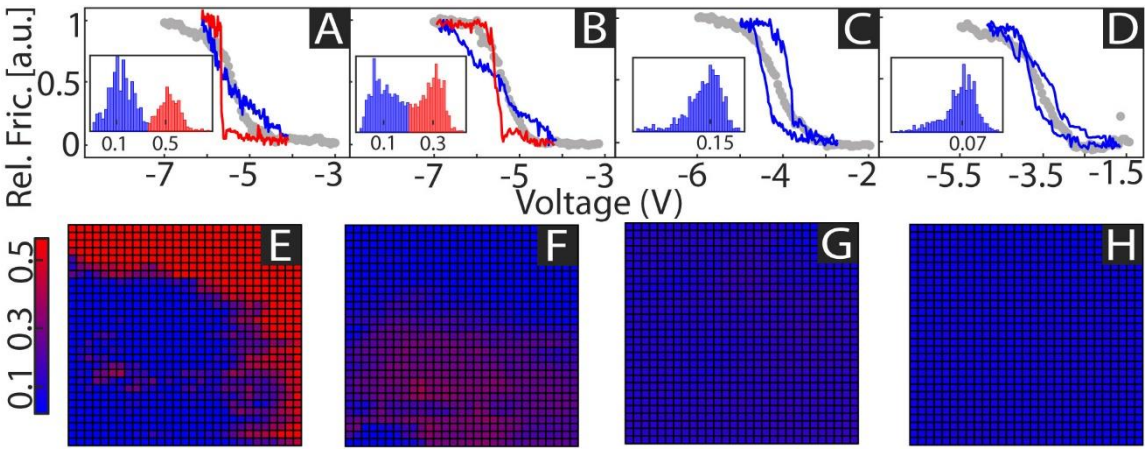

Figure 13: A), B), C) and D) Curves from Regime I and II for 10, 100, 300 and 700 nN overlaid over their respective Cumulative Reaction curves. E), F), G) and H) α map for 10, 100, 300 and 700 nN respectively

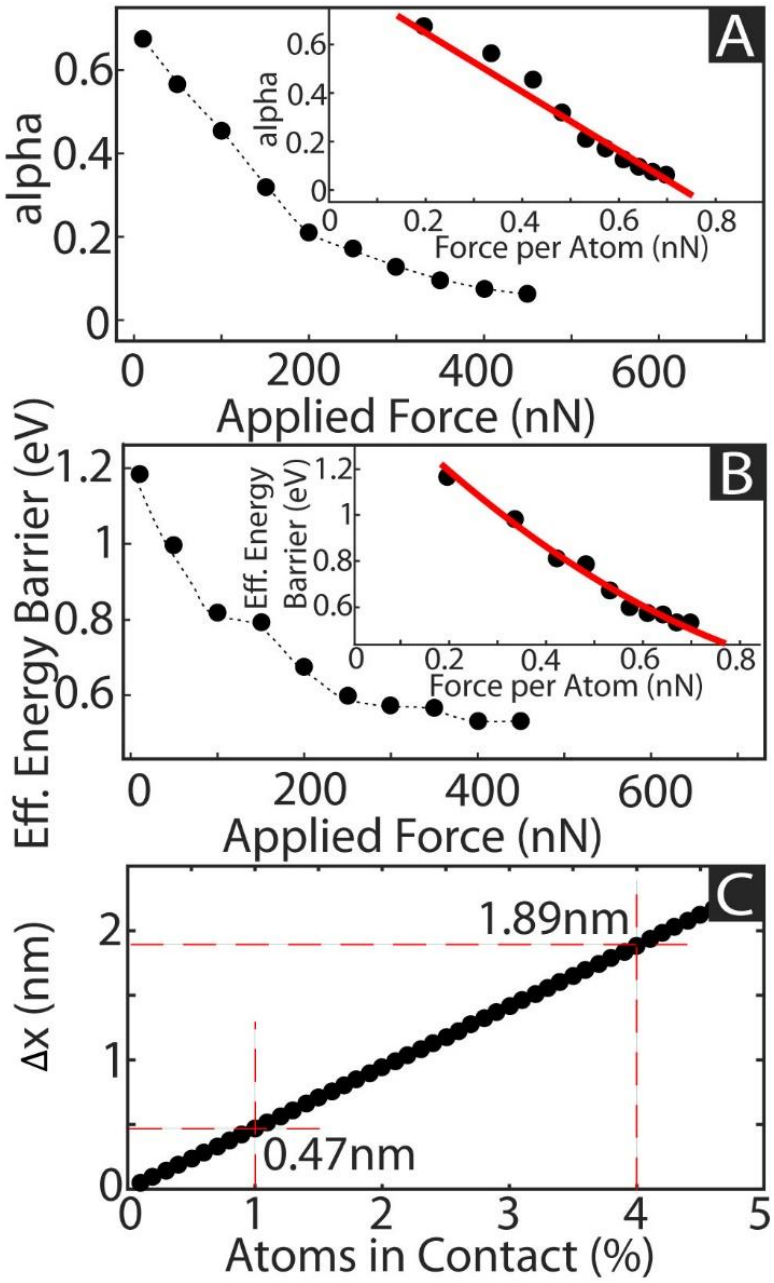

Figure 14: A) effective symmetry factor as a function of applied tip load. Inset shows the same as a function of force per atom. B) Effective energy barrier as a function of applied tip load. Inset shows the same as a function of force per atom. C) Path Length as a function of percent atoms considered in contact.

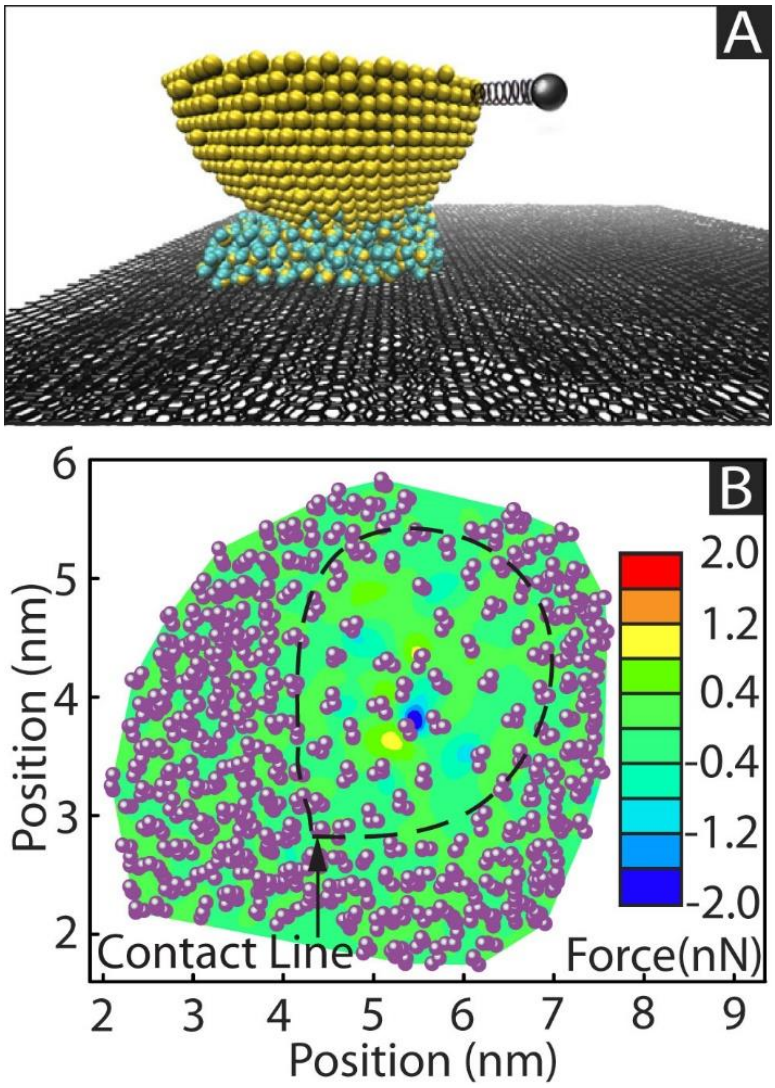

Figure 15: A) Molecular Dynamics (MD) simulation of a platinum AFM tip sliding across multi layered graphene substrate with water meniscus at contact. B) Normal Force distribution on the water meniscus due to the applied tip force showing force concentration on a fraction of water molecules at contact.

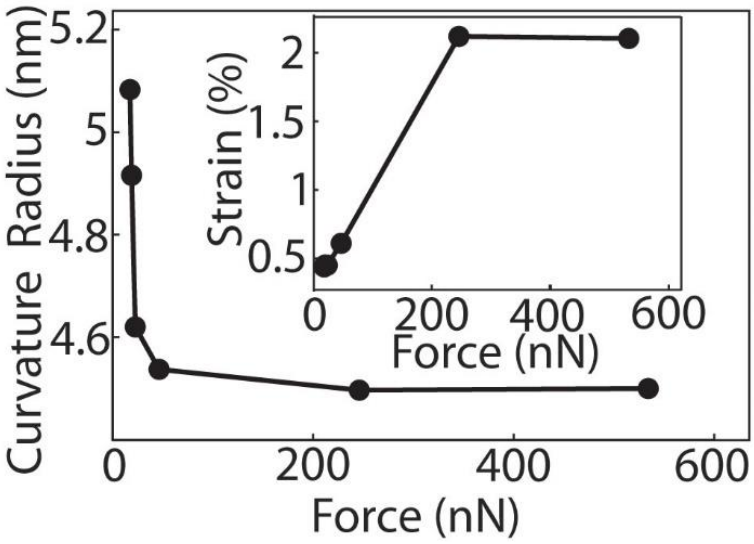

Figure 16: Results from Finite Element Simulation. Maximum curvature of graphene sheet as a function of applied tip load. While curvature increases with applied load, there is no significant increase beyond 50 nN tip load. Inset shows maximum strain (%) experienced by graphene sheet as a function of applied load.

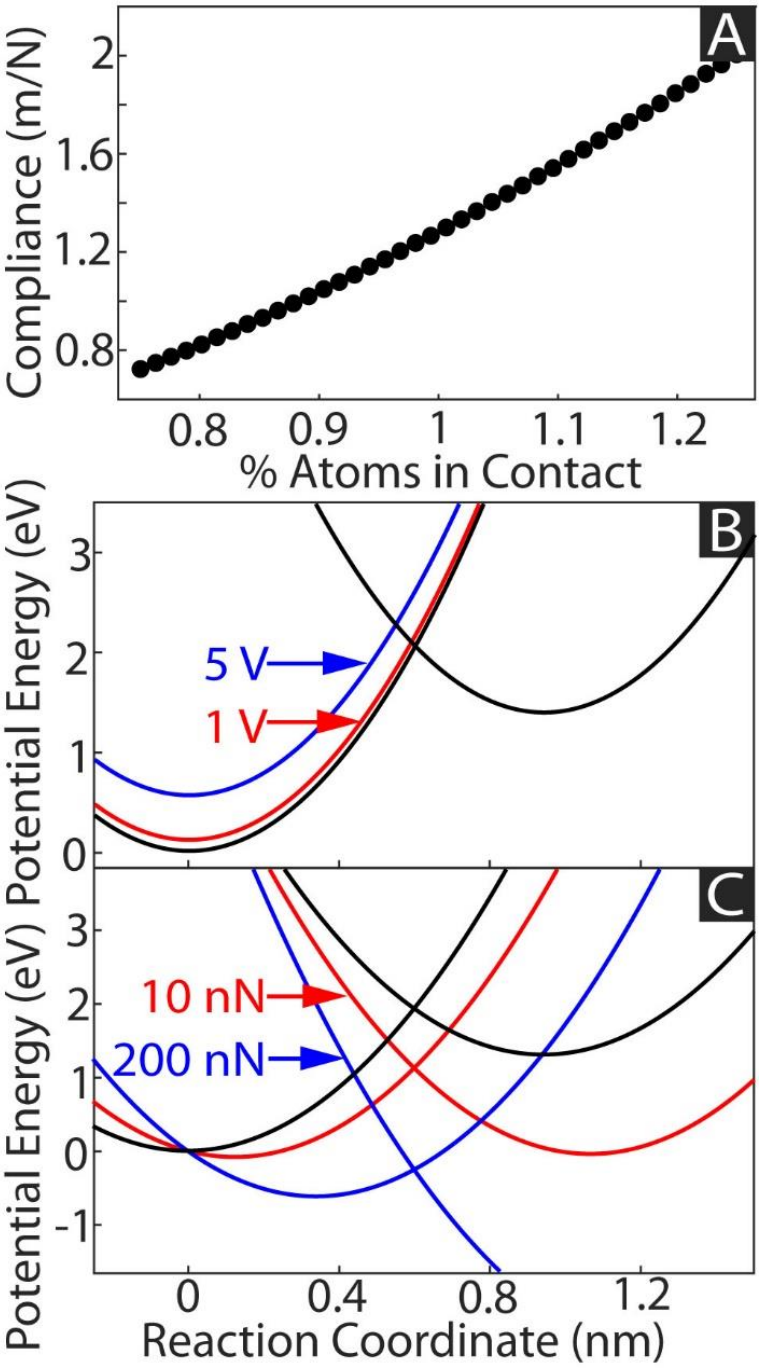

Figure 17: A) Compliance of interaction potential (γ) as a function of percent atoms in contact B) Force Effect – applied force tilts the potential energy profile. Black curve corresponds to unperturbed potential (V=0 & F=0). C) Applied Voltage only translates the reactant profile vertically. Black curve corresponds to unperturbed potential (V=0 & F=0).

CHAPTER IV

NANOMECHANICS OF CRUMPLED GRAPHENE

Introduction

Crumpled 2D sheets are a novel class of nanomaterials that have garnered significant research interest owing to their peculiar properties[118-124]. Deforming 2D materials has shown to directly influence the band gap, thereby providing a unique method to tune other material properties[125-128]. Both reversible and irreversible strain due to crumples, wrinkles and corrugations can influence the chemical potential, optical absorption and wettability of 2D materials[129, 130]. Nanoscale crumples are also compact 3D structures which still possess very high accessible surface area rivalling that of engineered layered and porous hierarchical materials[131]. A variety of 2D materials such as graphene, functionalized graphene, hexagonal boron nitride and MXenes have been synthesized into crumples while still preserving their chemistries intact, making them prominent candidates for energy storage and conversion, energy absorption, chemical sensing, strain sensing and material encapsulation[132-135].

Crumpled 2D sheets are a novel class of nanomaterials that have garnered significant research interest owing to their peculiar properties[118-124]. Deforming 2D materials has shown to directly influence the band gap, thereby providing a unique method to tune other material properties[125-128]. Both reversible and irreversible strain due to crumples, wrinkles and corrugations can influence the chemical potential, optical absorption and wettability of 2D materials[129, 130]. Nanoscale crumples are also compact 3D structures which still possess very high accessible surface area rivalling that

of engineered layered and porous hierarchical materials[131]. A variety of 2D materials such as graphene, functionalized graphene, hexagonal boron nitride and MXenes have been synthesized into crumples while still preserving their chemistries intact, making them prominent candidates for energy storage and conversion, energy absorption, chemical sensing, strain sensing and material encapsulation[132-135].

However, in order to incorporate crumpled nano-structures along with other materials in a wide range of applications, it is imperative to understand their mechanical properties and response to applied stress. Experiments in this regard are limited and typically probe single folds made by a sliding AFM tip[136] – which are meticulous but lack the statistical significance to describe a wide range of possible crease morphologies. Several molecular dynamics (MD) simulations explore uniaxial and hydrostatic compression of crumpled graphene[137, 138]. While they provide useful insight into the deformation behaviors, such experiments are not practical on isolated nanometer scale crumples. First principles theoretical based studies describe folding mechanisms of 2D materials in great detail but require extensive experimental validations. There is a need to examine the mechanical properties and force response of individual nanometer scale crumples to extend single fold mechanics to mechanical behavior of macroscale clusters.

Experimental Procedure

In this work, we explore the mechanics of isolated graphene crumples through force-indentation routines using Atomic Force Microscopy (AFM). Crumpled graphene was synthesized using a protocol detailed in a previous study by spray drying dispersions of graphene and graphene oxide sheets[121]. The resulting crumples were directly

captured on silicon substrates and identified using commercial silicon AFM probes (Mikromasch HQ:NSC36/AL BS-C) which has a 10nm tip radius and a nominal spring constant of 0.6 N/m. Figure 18(a) illustrates an AFM tip of radius 10nm pushing on a single crumple of radius 150 nm resting on a rigid silicon substrate. AFM topography data of a single crumple was obtained in tapping mode (AC Mode) where the AFM tip is driven near its resonance frequency. Figure 18(b) shows a typical isolated single crumple that is approximately 300 nm wide and 300 nm tall. This compares well with scanning electron microscope (SEM) images of typical crumples as shown in Figure 18(c). We then switched to contact mode to probe its mechanical response by performing contact mode force-indentation curves close to the center of the crumple. Figure 19(a) shows a typical force indentation curve with negligible adhesion and continuous approach (blue) and retract (red) halves. However, we often observed force curves that had abrupt discontinuities. As the crumples are not chemically bonded to the surface in our experiments, rolling or sliding of crumples is possible when a large force is applied. The AFM tip can also jump abruptly as creases lock into each other. This can render force curves inconsistent, cause abrupt discontinuities in indentation and cause the AFM tip to twist and experience lateral forces which can be easily monitored through the friction signal of the AFM. Such cases with lateral forces were excluded from analyses. The AFM tip can also pick up bits of sheets which can convolute with the mechanical behavior of the crumples. We obtained force curves on Silicon surface before and after each experiment. Pushing against silicon is analogous to indenting an infinitely hard wall and should result in no indentation. Any

deviations indicated likely contamination of the tip which can be dropped off by scanning on clean silicon or may require replacing the tip.

Results

In cases we obtained consistent force curves as shown in Figure 19(a), we observed a large hysteresis between the approach and retract halves. The hysteresis in force-indentation curves is a measure of energy dissipation during an indentation cycle and can be attributed to several different reversible and irreversible mechanisms described further in this study. To assess the deformation mechanisms and to calculate the mechanical properties of the crumples it is necessary to apply contact mechanics models. Several contact mechanics models exist to describe a wide range of tip-sample interactions. In general, force-indentation curves can be qualitatively described as,

$$F \propto \delta^n \tag{30}$$

where, F is applied force, δ is indentation and n is the power law exponent that reveals the contact mechanics and the nature of mechanical response. The choice of appropriate model requires knowledge about the geometry of the sample, geometry of the indenter and the experimental strains induced during the force curves. Many individual crumples were extensively characterized by SEM and AFM and were found to be spherical with radius ~150nm. In our experiments, the indenter was a commercial Silicon AFM tip whose shape is a cone with a spherical apex of radius ~10nm. However, it has been shown experimentally and theoretically that the sphere to cone transition during indentation occurs for indentation values an order of magnitude greater than the tip radius[139, 140]. The experimental indentation was within ~40nm, which is on the order of tip radius,

suggesting that interaction was predominantly limited to the spherical portion of the tip and that the strains were small.

The validity of spherical indenter is further supported by our experimental force curves. Using equation(30), the exponent was obtained from force-indentation curve in Figure 19(a) as shown in Figure 19(A) inset. Clearly, there are three distinct deformation regimes with power law exponents *n* being 1.219, 2.484 and 1.346 respectively, all of which are significantly different from the expected power law exponent of 2 for a conical indenter, thereby validating the choice of contact mechanics for a spherical indenter. However, there are several different contact mechanics models for spherical indenters. The choice from this point is purely dictated by the experimental results. The exponent at low applied forces (n=1.219) is close to 3/2 indicating a linear elastic behavior under Hertzian approximation. Mathematically, this is given as,

$$F = \frac{4}{3} Y_{eff} R_{tip}^{\frac{1}{2}} \delta^{\frac{3}{2}} \tag{31}$$

where, Y_{eff} is the effective young's modulus of the tip-crumple contact, R_{tip} is the tip radius and δ is the indentation. Any deviation from this exponent bears clear indication to the deformation mechanism. For instance, the exponent of the second regime, *n*=2.484, is much higher than 3/2 suggesting strain hardening. This is likely due to more closer packing of the creases under compression reflecting as the strengthening of the crumple. Whereas, the third regime indicates a subsequent decrease in the exponent (*n*=1.346), suggesting a strain weakening behavior likely due to plastic deformation during formation of new creases. Thus, the three regimes in the crumple deformation behavior can be identified as elastic (I), hardening (II) and plastic (III).

To decouple the irreversible and reversible interactions between the indenter and the crumple, we performed fatigue test by repeatedly pushing on the crumple (Figure 19(b)). From the evolution of force curves as a function of iterations, we could observe irreversible interactions by two means. First, the initial three regime behavior of the crumples, steadily transitions into a two-regime behavior with the disappearance of the plastic deformation regime. Tracking the exponents of the three regimes as a function of iterations like in Figure 19(b) inset clearly demonstrates that the plastic deformation regime (green diamonds) gradually blends with the hardening regime (red squares). Second, as seen in Figure 19(b), the hysteresis between the approach and retract halves of the force curves changes with repeated pushing. This change in hysteresis tracked as function of iterations shows a steady decrease initially which stabilizes around 15 iterations (Figure 20 blue circles). The irreversible interactions can be attributed to formation of new creases and reorganization of existing creases, both of which increase the crease density of the crumple.

The hysteresis stabilized around 15 iterations and was reversible there on. Beyond this point, no plastic deformation is observed. This is further supported by calculating the indentation from force curves as a function of iterations as shown by red squares in Figure 20. The indentations gradually increase from 30.13 nm during the first iteration to 52.89 nm after 15 iterations indicating an irreversible change occurring to the crumple. Whereas, there is no significant change in the indentation from the 15th iteration, after which, the hysteresis and energy dissipation is also completely reversible. This can be attributed

purely to heat or frictional dissipation due to high pressure sliding of the layers in the crumple.

The total energy that went into creating creases can be calculated from Figure 20. For each iteration, the irreversible energy component in making creases is the difference between the actual energy dissipation at that iteration and the frictional dissipation energy. The total energy therefore is the cumulative sum of crease formation energy from each iteration. In the case of our crumples, the total crease formation energy was calculated to be 55.76 keV which must have created multiple creases in the already crumpled graphene. While the actual crease density cannot be measured without ex-situ techniques, this energy from our force-indentation can still be related in a useful way to energy required to bend flat sheets of graphene. Theoretical studies show that graphene exhibits a racquet type bending (Figure 21(a) illustrates the cross section of an arbitrary fold)[124, 141-144]. The total length of the fold (L_{Total}) is the sum of the flat (L_1) and bent regions (L_2) given as,

$$L_{Total} = 2L_1 + 2L_2 \tag{32}$$

Bending a flat sheet of graphene is a competition between the adhesion between the flat portion (L_1) and bending rigidity from the curved portion (L_2). Mathematically it can be stated as,

$$U_{Total} = [\![(U]\!]_{Bend} \times 2L_2) - (U_{Adhesion} \times 2L_1) \tag{33}$$

where, U_{Total} is the total energy of folded graphene, U_{Bend} is the bending rigidity of graphene and $U_{Adhesion}$ is the adhesion energy of graphene. Generally, a stable fold minimizes the total energy. Specifically, when a fold is made such that the magnitude of adhesion energy from L_1 is less than the magnitude of bending energy from L_2, the total energy becomes positive and results in an unstable folded state which unravel

spontaneously. Whereas, when the magnitude of adhesion energy is greater than that of bending energy, the total energy is negative, and the fold is stable.

Molecular dynamics simulations based on the energy balance in equation(33) show that graphene sheets must be sufficiently long to sustain a fold[143]. Specifically, when the total length of fold cross section given by equation(32) is less than 6.5 nm, it cannot sustain a fold and it would remain flat even on external perturbation. When the total length is between 6.5 and 10.5 nm, folded states are metastable and unravel back to flat morphology with external perturbations. When the total length is exactly equal to 10.5 nm, folded state is more stable than flat graphene and hence it is thermodynamically preferable. This scenario is special because at L_{Total} = 10.5 nm, simulations show that L_2 must be 2.5 nm, meaning only one folded configuration is possible. Whereas, for sheets longer than 10.5 nm, a range of stable folded configurations are possible with varying values of L_2. Nevertheless, irrespective of the total length, the minimum energy configuration always has L_2 = 2.5 nm.

The existence of a metastable and stable states makes it possible to describe the folding process as a structural transformation from an initial flat state to a final folded state with an energy barrier to cross over a metastable transition state. Generally, reaction coordinate diagrams are utilized to describe the evolution of potential energy during structural changes. The reaction coordinate is a parameter that tracks all the geometrical changes occurring during the transformation. In the context of fold cross section represented in Figure 21(a) we can choose overlap length as the reaction coordinate that can effectively replace the lengths L_1 and L_2 to adequately describe the fold morphology.

Figure 21(b) shows the reaction coordinate diagram for the fold process, where, the initial flat state must acquire the activation energy barrier (E_a) to cross over the metastable state and attain the stable folded state. The activation energy i.e. the difference between the metastable state and the flat state is shown through MD simulations to be +30eV[143]. The transition state theory based thermodynamic description allows us to relate the energy barrier to the energy dissipated during the force curve experiments in creating more creases in the crumple. On the assumption that every fold process goes through the metastable state to reach the final folded state, each fold consumes 30eV. Therefore, the total energy spent during force curves (55.76 keV) should have resulted in nearly 1850 individual fold events, thereby increasing the overall crease density of the crumple considerably.

As 2D materials essentially inherit their bending rigidity from their chemistry, the critical sheet length for stable fold and the energetics of folding must depend on the chemistry of the starting sheets. To explore the effect of chemistry, we performed our force-indentation fatigue routine on several similarly sized graphene and graphene oxide crumples. Figure 22, which shows two representative experiments each for graphene oxide (open and closed black circles) and graphene (open and closed red squares), demonstrates that the magnitude of irreversible component of energy dissipation for graphene oxide is larger than that of graphene oxide. This suggests that, for the same experimental conditions, crumpled graphene consistently converted a smaller fraction of input energy towards making new creases than crumpled graphene oxide. This is consistent with simulations and experiments that show that the bending rigidity of graphene is much

higher than that of graphene oxide[145] and that presence of defects reduces the barrier to folding and results in more stable folded configurations[146, 147].

Conclusion

Folding in crumpled materials is a random and complex phenomenon, where, the folding mechanics and the cross section of fold has also been shown to vary with the number of layers that are being folded. The critical folding length increases with number of layers, whereas, the energy barrier for folding decreases with number of layers[141]. Crumpling also causes local stacking of multiple layers, mechanics and energy absorption characteristics of which are significantly different from single layer bending. Observing changes to surface and inner crease morphologies during compression of a nanometer scale crumple is not trivial and requires specialized equipment. Conducting our force-indentation routines within Scanning Electron Microscopes (SEM) and combining AFMs with Transmission electron Microscopes will help assess the surface and sub-surface structural evolution of crumples on compression.

In summary, we have demonstrated a robust ambient mode atomic force microscopy routine to measure and monitor energy absorption characteristics of crumpled graphene. Crumpled graphene shows a marked non linearity in force-indentation and strain hardening with increased applied load. The hysteresis between the loading and unloading halves reduces with repeated compressions and bears a measure of new crease formation events. Our experiments allow direct comparison with first principles based theoretical studies enabling us to quantify the energetics of the aggregate fold events. Crumpling graphene results in a morphology capable of absorbing large amounts of

mechanical energy, while still providing a large accessible surface area. Crumpled Graphene converts a smaller fraction of input energy into creases than crumpled graphene oxide, demonstrating that the energy absorption characteristics can be tuned by controlling the extent and type of functionalization of graphene. The tunability of mechanical behavior by control over chemistry and a large accessible surface area makes crumpled morphology of 2D materials a promising candidate for applications in the fields of reversible energy and material storage, chemical sensing and friction modification.

Figures

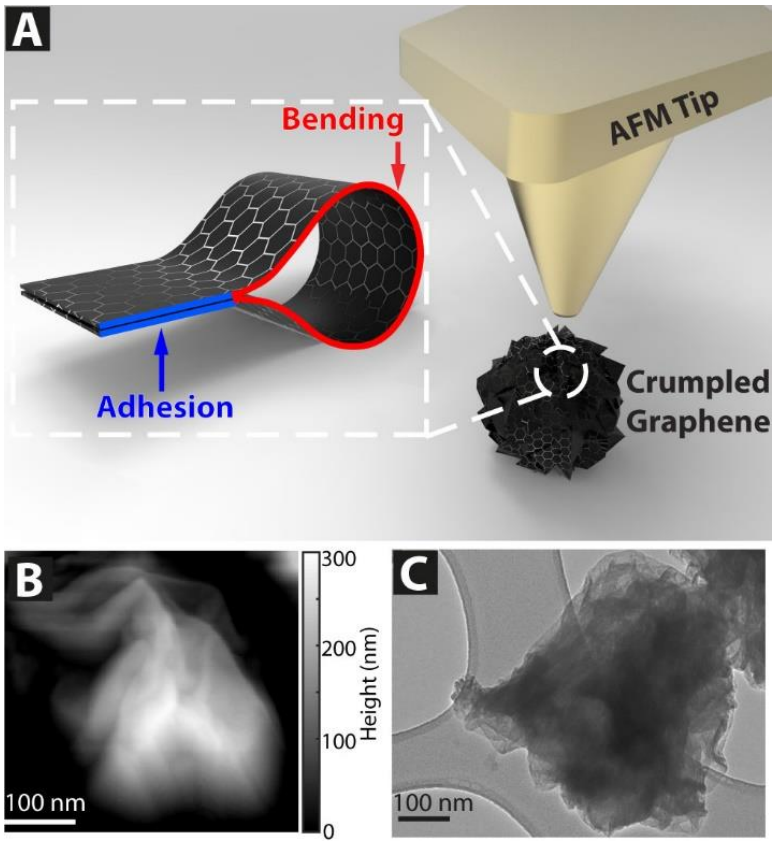

Figure 18: A) A silicon AFM tip pushes on crumpled graphene sample held on a rigid silicon substrate. B) AFM image of a typical isolated crumple. C) SEM image of a typical crumple.

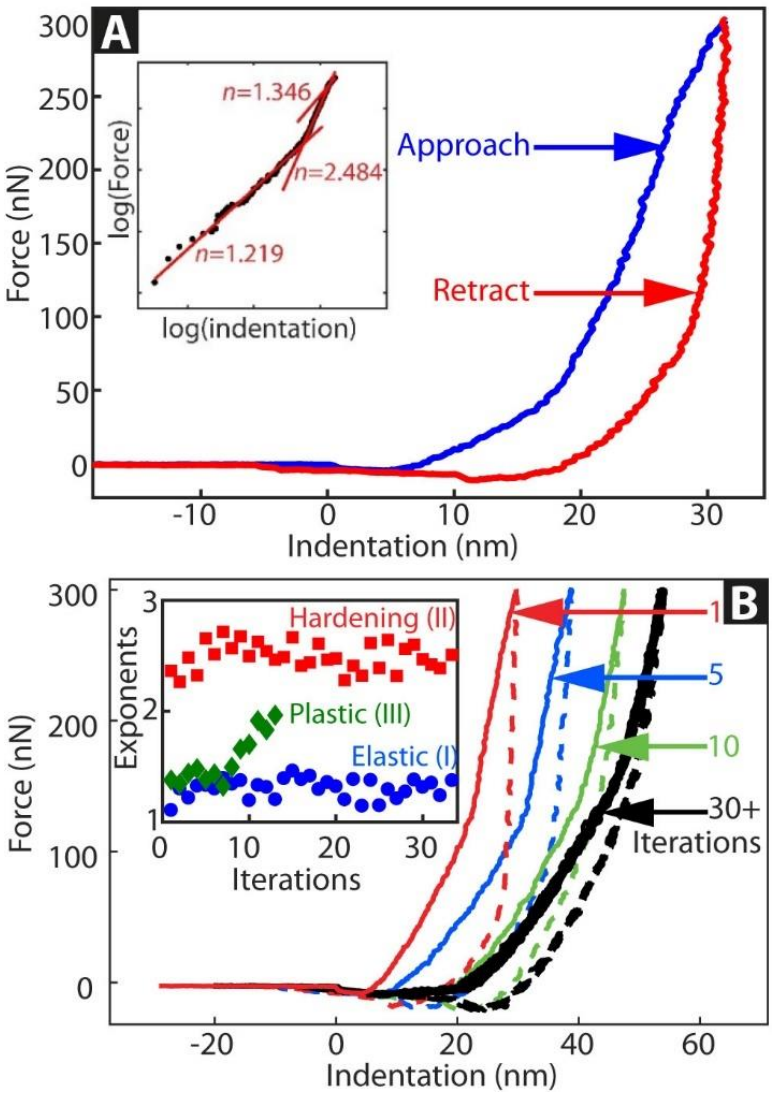

Figure 19: A) A typical force curve obtained on crumpled graphene sample. The hysteresis (area between the approach and retract curves) is a measure of energy dissipated during the interaction of the AFM tip and crumples. Inset shows the regimes identified from log-log plot. B) Repeated force-indentation curves on a crumple shows steady decrease in hysteresis during the first few iterations (specified by number). Inset plots the exponents from each deformation regime as a function of iterations.

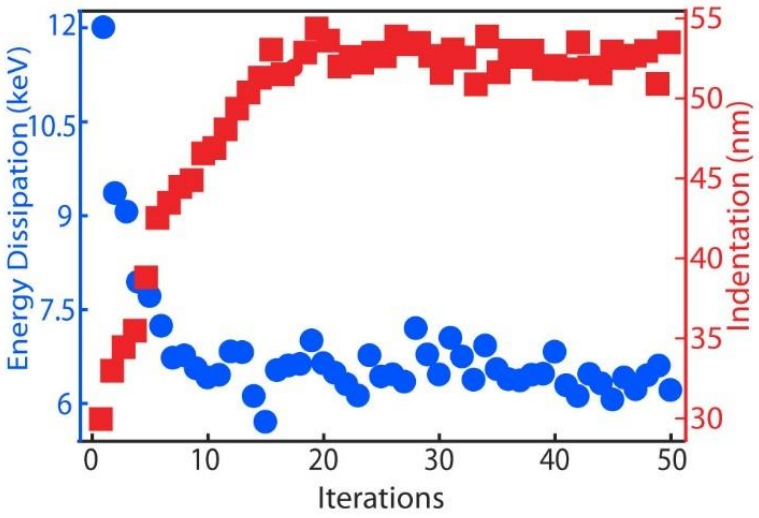

Figure 20: Hysteresis as a function of iterations (black circle). Indentation as a function of iterations (red squares).

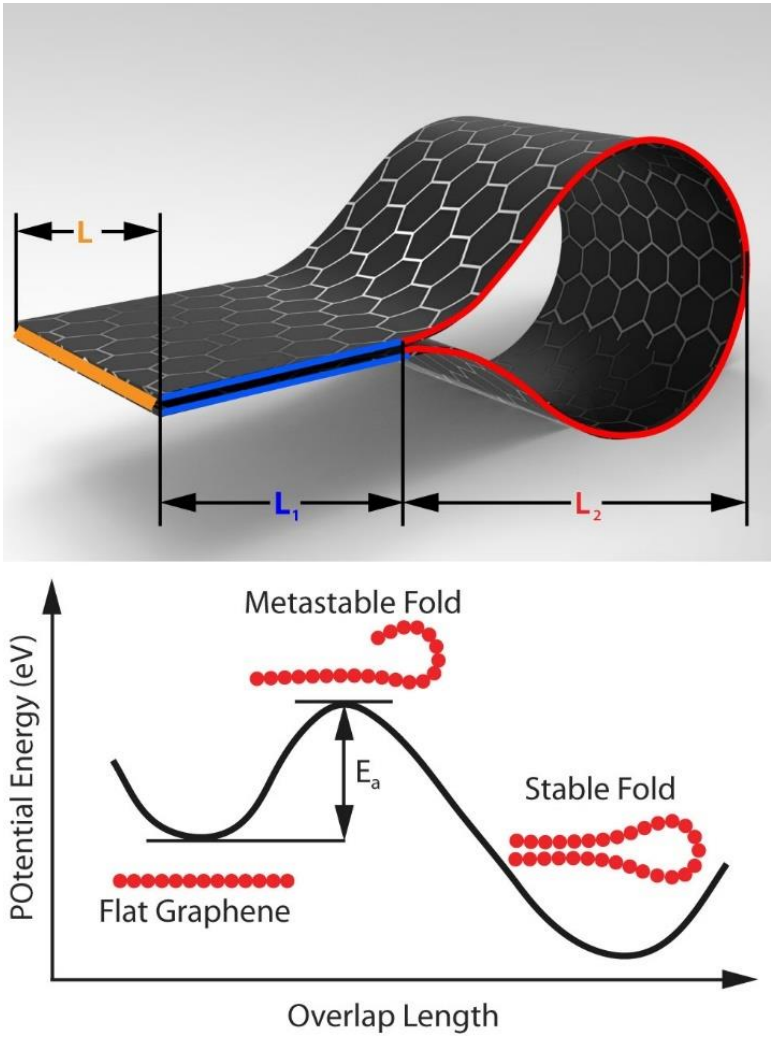

Figure 21: A) Racquet type bending of graphene representing a fold as a competition between adhesion and bending rigidity. Length L1 is in Adhesion and length L2 is in bending. B) Graphene Fold process is represented as a structural transformation with a finite energy barrier.

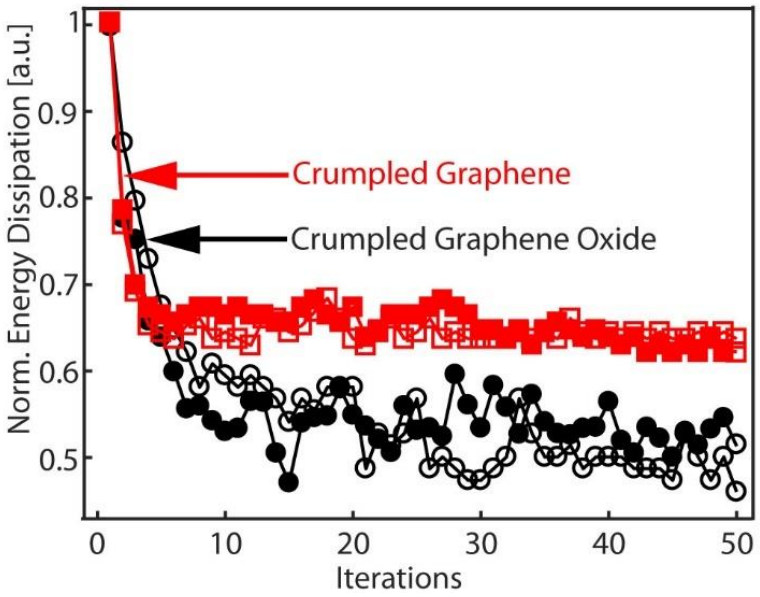

Figure 22: Normalized energy dissipation as a function iterations.

CHAPTER V

A REACTOR FOR GRAM SCALE MECHANO-CHEMICAL SYNTHESIS

Introduction

Much of this dissertation has explored mechanochemistry at the atomic scale. We showed that applied force can significantly alter the reaction conditions and accelerate the processes. Applied force can also reduce the energy barrier for oxygen desorption and adsorption on graphene. This chapter focuses on the design, operation and testing of a novel reactor for gram scale mechanochemical synthesis, that can directly leverage insights obtained from our nanoscale AFM experiments.

Although mechanochemistry is an ancient concept, some of the most significant developments in mechanochemical synthesis took place only in the last three decades. The primary driving force behind the efforts was the need to establish cleaner, safer and more efficient material synthesis protocols to realize a future of sustainable green chemistry[148-150]. Traditional solvothermal synthesis involves significant amounts of expensive and hazardous solvents, leading to significant amounts of waste, environmental and health hazards, and excess cost. Driving reaction through force provides an additional and alternative route for producing a wide range of chemical compounds that requires little or no solvents and is inherently scalable.

Current Trends in Mechano-chemical Synthesis

Mechano-synthesis protocols typically involve ball milling the starting reactants with very little to no use of dissolution media. In its rudimentary form, a ball mill is a

closed steel vessel containing hard metal or ceramic balls [151]. When the setup is aggressively shaken or rotated, reactants enclosed in the vessel are ground by the metal balls and are progressively fragmented. This continuous fragmentation introduces defects in the materials and expose fresh surfaces which increases the chemical reactivity without the use of liquid media. Several kinds of mills such as planetary mills, vibration mills, pin mills and rolling mills were developed to increase the energy input to the reactants and to facilitate continuous material processing[151].

Recent efforts include integration of *in situ* chemical measurement techniques such as X-Ray Diffraction (XRD), Raman and Infra-Red Spectroscopy with high energy milling[152-154]. One such real time kinetics study of mechano-chemical MOF synthesis using *in situ* XRD revealed a first order process pointing towards diffusion limited kinetics[155]. *In situ* studies have also been successful in revealing novel material topologies and metastable intermediates previously unexplored [156]. Mechano-chemistry even offers excellent stoichiometric control[157-160], unique synthesis routes and products impossible to produce in solution media[161-163].

While there has been significant effort in developing sophisticated devices that can both drive and monitor large scale mechano-synthesis, it is currently impossible to know the magnitude or direction of the force vector on the reacting species, precluding deep fundamental understanding of how force drives these important synthesis reactions. Most studies describe the energy input to the reactants in parameters that are specific to the design of the equipment driving the reaction and in units that are incompatible with conventional thermodynamic descriptors. This lack of knowledge has largely limited the

predictive power of mechano-chemistry, creating a significant bottleneck in the design of chemical synthesis routes a priori.

Here, we introduce a device to apply precise forces on bulk materials in a controlled fashion. We further test, for the first time, the following fundamental questions of mechano-chemistry at the bulk macroscale: 1) how does the magnitude of the force affect the rate of the chemical reaction under study, 2) does the direction of the applied load relative to the impacting surface matter (i.e. is the reaction driven preferentially by compression or shear)?, and 3) for cases where multiple reaction products are possible, are the yields for these products sensitive to the magnitude and direction of load (i.e. can we preferentially make one species by controlling load and its direction)?

Device Design

Our mechano-chemical reactor has tightly coupled hardware and LabView based software routines to enable real time force control. The reactor has a steel sphere mounted onto a vertical shaft which is powered by an AC motor (Figure 23). Reciprocating motion causes the sphere to strike the sample stage. On impact, the stage slides away and the attached shaft hits the force sensor. As a result, the entire sensor assembly on that side moves away from the electromagnet and in turn engages the sensor assembly on the other side onto its electromagnet. We record the impact transmitted from the sphere to the force sensor in microsecond time resolution using a commercially available Data Acquisition (DAQ) device and LabView. We achieve force control by tuning the strength of the DC electromagnet assembly. A larger current essentially produces stronger magnetic fields and holds the sensor assembly stronger. So, the sample stage experiences a larger impact

force before it slides away. When the sphere reciprocates back and forth at high speeds dictated by the VFD and impacts the stages repeatedly, our software lets us tune the holding force of the electromagnet and automatically records each impact on both sides. Below is a detailed description of all the sub-assemblies in the reactor.

The Actuator Assembly: The actuator assembly shown in Figure 24(a) is driven by an AC motor controlled by a variable frequency drive (VFD). The VFD provides speed control while maintaining torque which cannot be achieved with DC motors where the torque and speed are directly related. The actuator is a threaded shaft with a steel sphere (0.5-inch diameter) welded to one of its ends. The actuator is clamped to the reciprocator using two hex nuts. A large linear bearing provides a seal during movement and prevents sample spillage.

The Sample Assembly: The sample assembly shown in Figure 24(b) contains the sample enclosure for holding sample, and two sliding sample stages. The sample stage is threaded onto a shaft which impacts the force sensor. The sample stage is grooved and fitted with Teflon rings to minimize friction during sliding inside the sample enclosure.

The Electromagnet Assembly: The electromagnet assembly shown in Figure 24(c) contains a DC electromagnet (red) that is held in place inside the magnet enclosure. The enclosure also hosts linear bearing to minimize friction of the sliding shaft. The holding force of the electromagnet is directly proportional to the DC voltage applied to the electromagnet. The magnet used in our study can provide up to 120N holding force.

The Force sensor Assembly: Force sensor assembly (Figure 24(c)) is held in place by the electromagnet. When the sphere hits the sample stage and pushes it away, the shaft

hits the force sensor. This impact overcomes the holding force and pulls the magnetic piece (blue) away. Simultaneously, the force sensor records the impact with microsecond time resolution.

Prototype Fabrication

Fabrication was done in the Fischer Engineering Design Center of Texas A&M University (College Station, Texas). Figure 25 shows photographs of the prototype. The actuator was driven by a Brook Crompton 1HP 3 Phase AC motor whose speed was controlled by a single-phase input, three-phase output TECO-Westinghouse L510 Variable Frequency Drive (VFD). Electromagnets were made to order by APW Company which has a maximum holding force of 120N at 24V and were powered by programmable power supply PPS2116A purchased from Circuit Specialists. Impact profiles were measured using FX 1901 force sensor and captured at 1MHz sampling rate using an NI USB-6363 DAQ, which also powered the force sensor via the SCB-68A break out box. The VFD, power supply and the force sensor were triggered and controlled using LabView while real time data analyses were performed using embedded MATLAB sub-routines.

Calibration and Testing

Impact Calibration: We calibrated the reactor at 10Hz operating frequency, therefore causing 10 impacts per second on each sample stage. We recorded several impact profiles (in volts at 1MHz sampling rate) for electromagnet voltages ranging from 2-20 V with 2V increments. Figure 26(a) shows representative impact profile at each voltage, where, the impact profiles changed significantly with changing electromagnet voltage. The impact profiles can be well approximated by a Gaussian fit which is to be expected

for a single nearly elastic collision free of plastic deformations of colliding bodies. Any improper fastening of parts or coarse sliding due to damaged bearings created multiple successive collisions clearly observable in the impact profiles as multiple peaks. This enabled us to monitor the mechanical integrity of the reactor continually throughout a reaction. The impact profiles in voltages were then converted to force units using the factory calibration curve for the sensor. The peak force for each impact was observed to be linearly proportional to electromagnet voltage for both sensors (Figure 26(b)). At 10Hz, the minimum force our reactor can apply is 30N, whereas, the electromagnets used in this prototype tune the force up to ~120N. The calibration routine was performed before every experiment to ensure reliability and repeatability in measured forces.

Salt Particle Size Reduction: Almost all mechano-chemical synthesis protocols involve grinding or comminution of reactant particles as the first step. It is therefore essential to test the force dependence of particle size reduction. For this test, we used sodium chloride (NaCl) crystals purchased from sigma Aldrich. Fresh samples were mostly cubic crystals predominantly with 275µm dimension as shown in Figure 27(a). Whereas, we observed significant size reduction with grinding. For example, Figure 27(b) shows much smaller particles after 2 min at 30 N. To systematize the study, we measured the particle size distribution every 15s for up to 150s and repeated the set at 30, 75 and 120N impact force. In all cases, we observed that particles which were predominantly 275µm in dimension changed into 100µm in size over the course of grinding (Figure 27(c), (d) and (e)). However, the kinetics of reduction showed a strong dependence on the holding force. At 30N, the transition occurred around 75 seconds, whereas, at 75 and 150N, the transition

was as quick as 50 and 25 seconds respectively. This is more clearly illustrated by Figure 27(f) and (g) which plot the 275 μm peak and the 100μm peak as volume fractions as a function of time. This preliminary result proves the capability of our reactor to control the magnitude of the applied force.

Conclusion

We introduced a table top mechano-chemical reactor with force control and real time impact monitoring to perform gram scale mechano-chemical synthesis. We used tunable DC electromagnets to control the impact force, while measuring the collisions with microsecond time resolution. The impacts follow a gaussian profile indicating that the collision are near elastic and does not involve any plastic deformation of either the actuator or the sample stage. This device enables us to quantitatively assess force-dependence of mechano-chemical reactions, a feature that is not possible with existing ball mills. To test the reactor, we monitored salt particle size reduction at different forces. While the particles generally reduced in size at all forces, the kinetics of the process strongly depended on the magnitude of compressive forces. By adding in situ chemical measurement techniques, we can transform this prototype into an indispensable tool for probing solid state reactions in both labs and other research facilities.

Figures

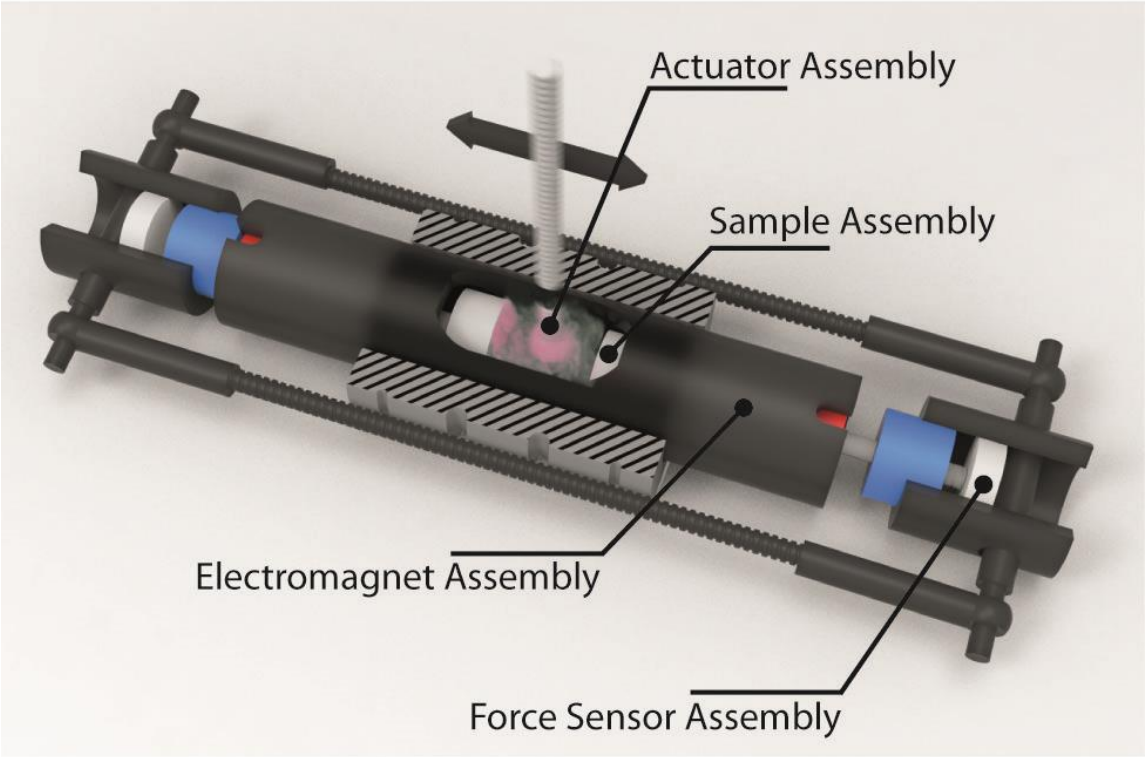

Figure 23: Mechano-chemical reactor with force control. Hatched areas show cutaway.

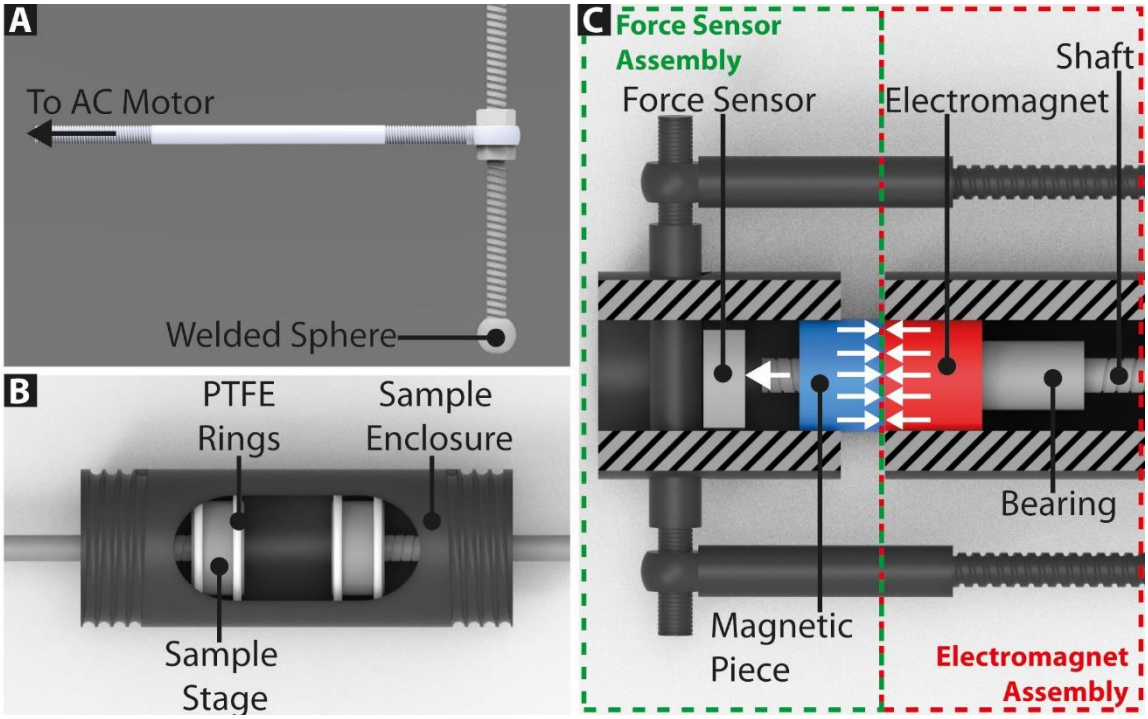

Figure 24: Various Assemblies in the reactor. A) Sphere welded to a vertical shaft. The horizontal shaft is powered by an AC motor. B) Sample enclosure containing sliding sample stages. Teflon rings minimize friction due to sliding. C) Force control assembly containing electromagnet and a magnetic piece. When the shaft hits the force sensor, it overcomes the holding force and pushes the magnetic piece away. Simultaneously, the force sensor records the impact with microsecond time resolution. Hatched areas represent cutaway.

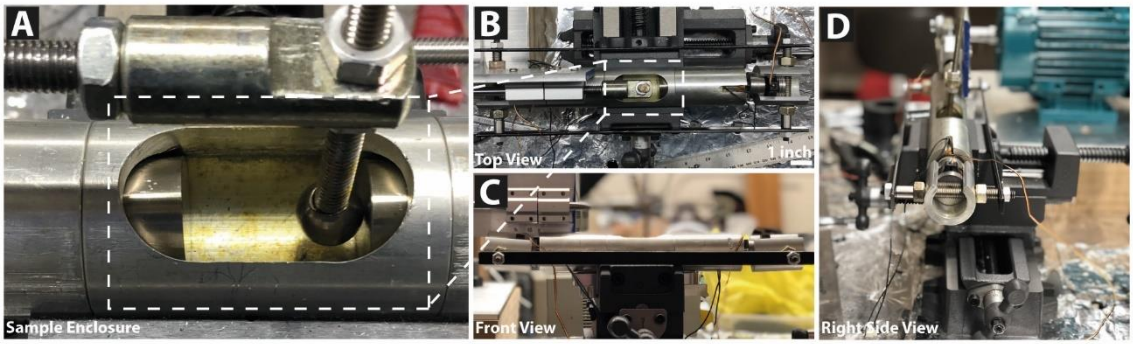

Figure 25: Photographs of A) Sample Enclosure, B) Top View, C) Front View and D) Right Side View.

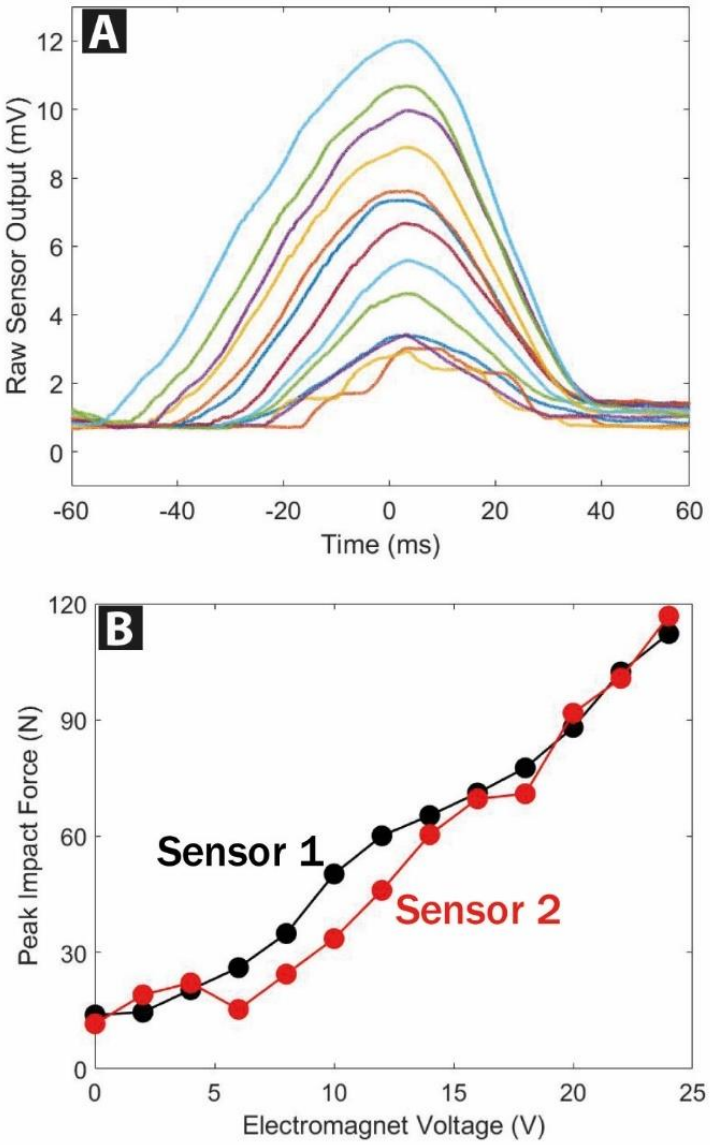

Figure 26: A) Impact profiles as a function of time for various electromagnet voltages. B) Peak impact force as a function of electromagnet voltage for both force sensors.

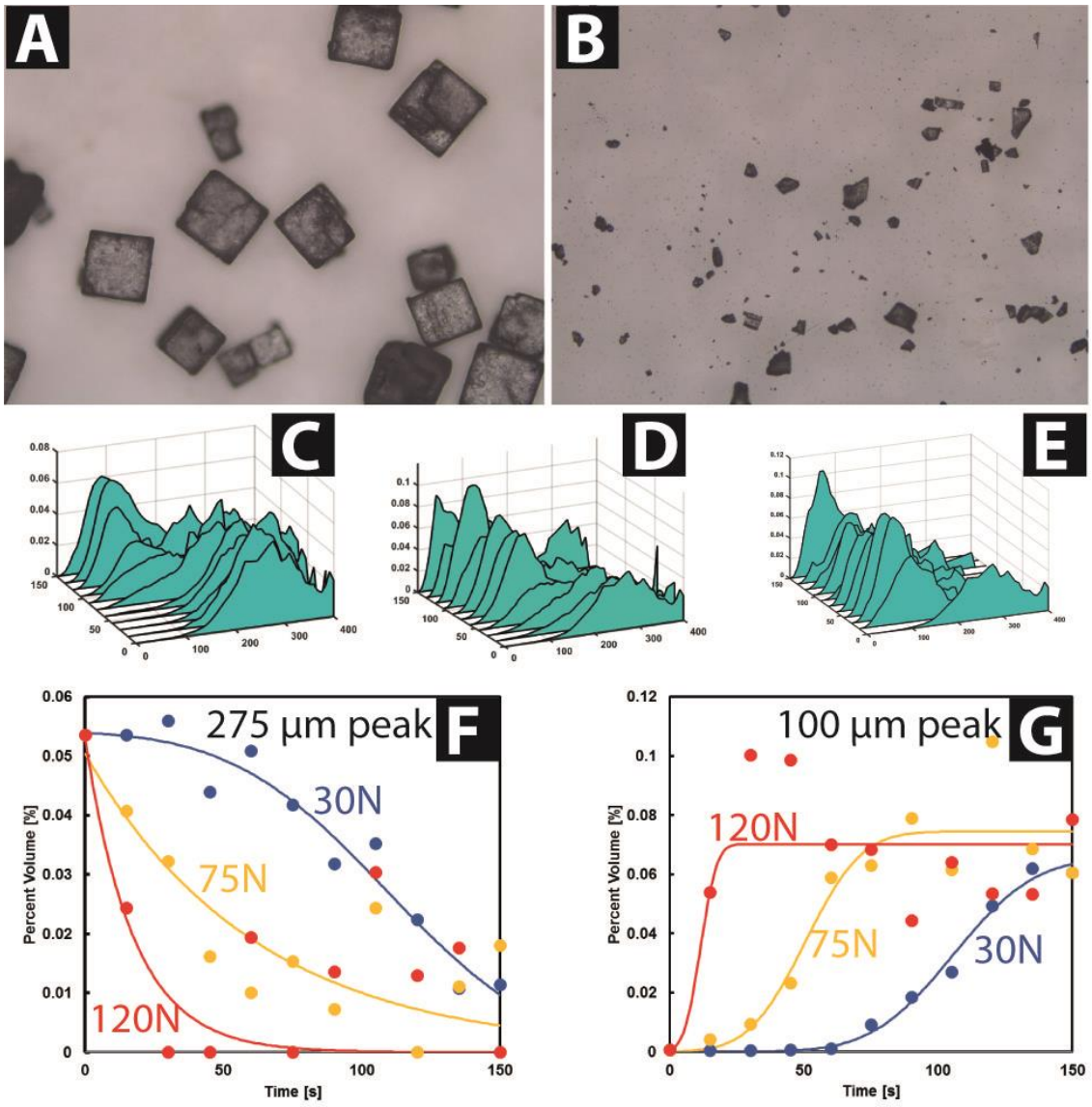

Figure 27: Results from Salt Particle size reduction experiment. A) initial optical microscope image showing predominantly crystalline material. B) After 2 min of grinding at 30N showing a significant size reduction. C, D and E) particle size histograms for 30, 75 and 120N holding force. All three histograms show a size reduction which is clear from the disappearance of 275 µm peak and the appearance of 100µm peak. However, the kinetics of size reduction is fairly slow at 30N, and it becomes faster with increasing holding forces. F and G) 275µm peak and 100µm peak respectively shown as volume fractions as a function of time exhibit clear force dependence.

CHAPTER VI

CONCLUSIONS AND FUTURE DIRECTIONS

Introduction

This dissertation systematically explores the fundamental connections between nanotribology, Nano mechanics and mechano-chemistry and examines the possibility of describing them with a single theoretical framework based on chemical kinetics and reaction dynamics. We provided a theoretical framework based on transition state theory and chemical kinetics to describe chemical reactions simultaneously driven by heat, stress and electric field (Chapter 1). With our work on thermal reduction of Graphene Oxide and electrochemical oxidation of graphene (Chapter 2 and 3), we showed that friction strongly depends on the surface chemistry. The Nano mechanics of crumpled graphene (Chapter 4) demonstrated that structural transformations and deformations at the atomic scale can be described as thermally activated processes. The mechano-chemical reactor (Chapter 5) aims at extending these insights to the gram scale by introducing force control. This chapter points out interesting questions that stem from our studies and proposes future directions in each discipline.

Friction-Composition: The phenomenon of friction has been studied for a few centuries, yet, its physical and chemical origin is as elusive as ever. The very basic empirical relationship, called Amonton's law, that friction is proportional to the normal force is widely used even today despite studies reporting many instances where this law can be violated. Friction can depend on chemical composition of surfaces in contact, direction of sliding and the environment[164-166]. Most studies pointing out such

interesting trends in friction have been atomic scale AFM experiments due to the ability to probe sliding between two well defined surfaces with exquisite control over force applied between them.

Further, our studies qualitatively indicate that the friction contrast between oxygenated graphene and pristine graphene is very different for mechano-thermal and mechano-electrochemical reactions. Figure 28 shows sub 50 nm lines fabricated by thermal reduction (Figure 28(a)) and electrochemical oxidation (Figure 28(c)). The contrast between oxygenated graphene is ~2x for thermal reduction (Figure 28(b)), whereas the contrast is ~6x for electrochemical oxidation (Figure 28(d)). This likely indicates that friction also depends on the extent and type of functional groups on the surface. By combining our tribology routines with orthogonal chemical measurement techniques, we intend to explore the dependence of friction on the type and extent of chemical composition quantitatively at the atomic scale.

Traditionally, Raman and IR spectroscopy are powerful tools to study the extent and type of functional groups on graphene. Defect density of graphene can be assessed by analyzing the Raman spectra of pristine and functionalized graphene. Whereas, absorption peaks in IR spectroscopy are strong indicators of the type of functional groups on graphene. Despite traditional Raman and FTIR are effective chemical analyses techniques, their spatial resolution requires fabricating large features thereby rendering AFM based experiments time consuming. Recent developments combine Raman and IR spectroscopy with AFM techniques to break the diffraction limit and increase the spatial resolution. Studies have shown that the defect densities in graphene can be monitored by TERS[167].

Recent study shows that the type of functional groups can be mapped out on graphene using AFM-IR[168]. Therefore, correlating friction evolution from our AFM routines with chemical measurements such as AFM-IR and TERS will provide fundamental insights into the relationship between friction and chemical composition.

Directionality of Force: One of the unique aspects of mechano-chemistry that differentiates it from thermochemistry is that the direction of applied force can lead to vastly different kinetics and yet this aspect is largely unexplored in a systematic and quantitative manner. Our framework of using friction to track chemical change can be extended to study the kinetics and energetics of bond removal of oxygen cleavage on graphene as a function of normal and shear forces in an AFM.

The normal force in an AFM can be tuned by changing the deflection of the cantilever or in other words by simply pushing harder on the sample. An AFM tip is essentially an end loaded cantilever beam whose spring stiffness in the vertical direction can be calibrated through force deflection curves. With a known normal stiffness of the beam, a very precise normal force can be applied on the surface. When an AFM tip pushes on the surface the contact area increases, thereby increasing the quantity of interaction between the tip and surface. Many contact mechanics models exist that can provide contact area-Normal Force relationship[169]. While it is intuitive that sliding friction should increase with increased quantity of contact, the exact relationship between friction force and the contact area is complicated. Especially, an AFM experiment like ours which often involves multiple asperities in contact and care should be taken to characterize the tip

shape and to monitor tip wear frequently when directly measuring the Friction-Normal Force relationship.

The lateral force on the other hand can be tuned by controlling the velocity of sliding. Many studies have explored the dependence of lateral force (often called as friction force) on sliding velocity[170, 171]. Generally, the sliding between an AFM tip and a surface can be regarded as a series of thermally activated lattice hopping processes. The resulting motion of the tip on a surface exhibits a characteristic saw-tooth like stick-slip behavior. According to the Prandtl-Tomlinson Model, lateral force increases logarithmically with sliding velocities. At sufficiently high sliding velocities however, thermal activation ceases to be relevant and the lateral force becomes a constant value.

Chapters 1 and 2 describe how wear influences measured relative friction. We showed at a preliminary level that relative friction can be used as a measure to monitor the surface composition. With slight modifications to our experiments, wear processes can be studied as a function of normal and lateral forces simultaneously by incorporating normal and lateral load effects on friction. To test this, we probed mechano-chemical removal of oxygen from graphene as a function of increasing velocity (lateral force) for various applied normal forces (Figure 29). From the relative friction, which is a proxy for composition, we can see that the wear process strongly depends both the normal and shear loads. At extremely low normal loads (15, 25 and 50nN), we observed a transition velocity beyond which wear accelerates. Conversely, there was no significant wear at low velocities (shear forces). This transition velocity decreased with increasing normal loads

and at high applied loads (175, 200 and 300nN), slow speeds and thereby low shear forces were sufficient to initiate wear.

We hypothesize that there is a competition between the friction dependence on wear and velocity. As friction increases with sliding velocity and mechano-chemical wear leads to a friction decrease, a combination of these results in a characteristic transition velocity observed in Figure 29. By incorporating these effects into the theoretical framework described in Chapter 1, we can decouple the kinetics and energetics dependence on normal and lateral (shear) forces.

Next Generation Mechano-chemical Reactor: Our current prototype introduced normal force control and demonstrated dependence of comminution kinetics on compressive or Normal Force. This sets the stage to directly assess the fundamental principles of mechano-chemistry at the gram scale. First, by choosing appropriate candidate reactions, we can study the rates and energetics of chemical processes. However, this requires us to continually monitor the products formed within the reactor. While some mechano-chemical reactions exhibit a distinct color change which can be sufficiently captured by timed snaps or a video, most mechano-chemical reactions yield products that can be identified only through spectroscopic tools. Therefore, by incorporating in situ spectroscopic methods, our reactor can be greatly improved to rival existing ball mills that possess similar features.

Second, we can add shear force control to the reactor by installing a separate motor on the actuator shaft to rotate it at controlled speeds and torques. This enables us to test the independent effects of shear and normal forces on reaction kinetics and energetics at

the gram scale. Studies show that the products, their relative compositions and their stabilities strongly depend on the type of ball mill[151, 172, 173]. This demonstrates at a preliminary level that normal and shear force can have their own unique effects on reactions. However, with precise control over the magnitudes like in our reactor and in situ chemical monitoring, we can quantitatively interpret the results using the chemical kinetics framework.

Figures

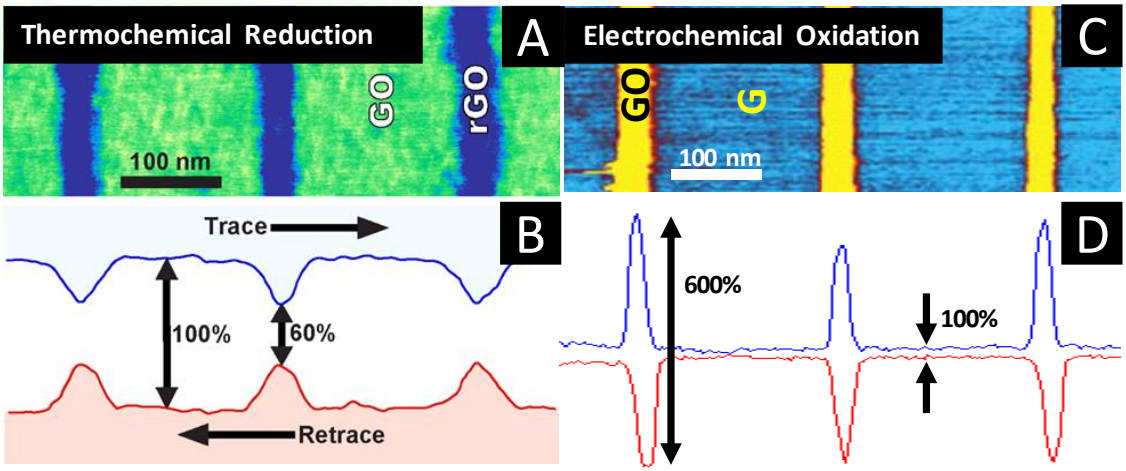

Figure 28: A) Thermochemically reduced features on GO. B) Line scan through features in A showing a 40% drop in friction. C) Electrochemically oxidized features on pristine graphene. D) Line scan through features in C showing 6 times increase in friction.

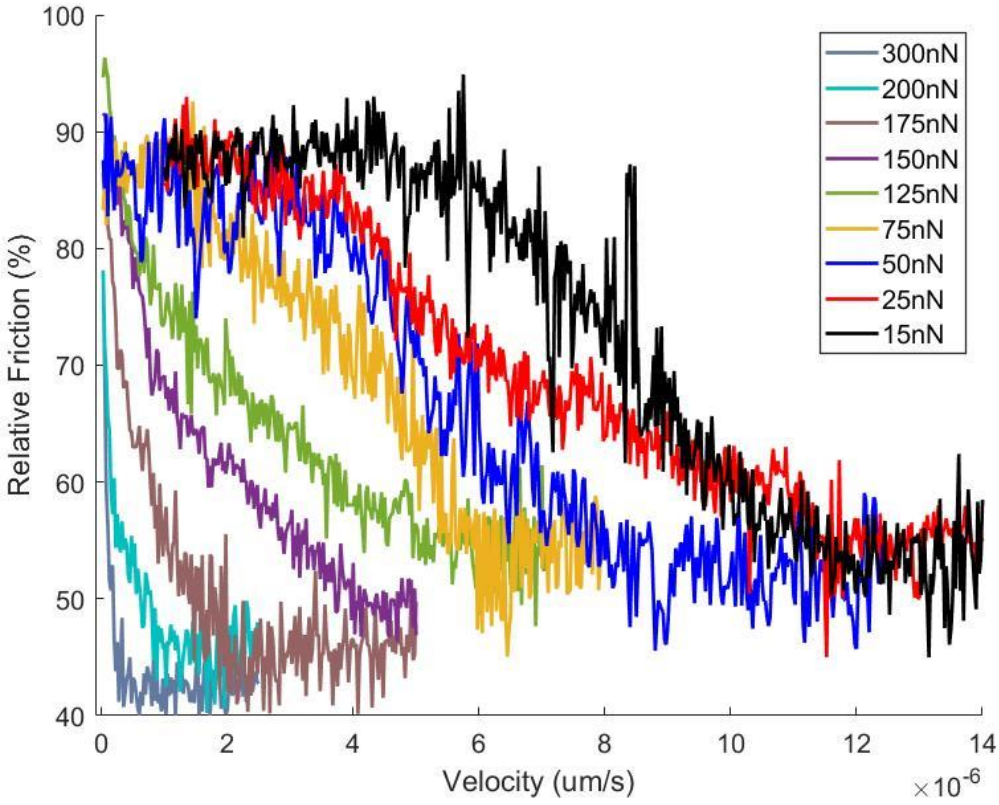

Figure 29: Graphene oxide reduction as a function of shear force (Velocity) for various applied normal forces.

REFERENCES

1. Takacs, L., *The historical development of mechanochemistry.* Chemical Society Reviews, 2013. **42**(18): p. 7649-7659.

2. Avvakumov, E., *Mechanical methods of activation of chemical processes*. 1986, Nauka, Novosibirsk.

3. Lea, M., *Researches on the latent image.* Brit J Phot, 1866. **13**: p. 84.

4. Benjamin, J. *New materials by mechanical alloying techniques*. in *E. Arzt and LS Schultz (Eds. i, DGM Conf, Calw-Hirsau, FRG, 3 5 October 1988, p. 3*. 1989.

5. Crismer, L., *Walthère Spring, sa vie et son œuvre*. 1912.

6. Ling, A.R. and J.L. Baker, *Halogen derivatives of quinone. Part III. Derivatives of quinhydrone.* Journal of the Chemical Society, Transactions, 1893. **63**: p. 1314-1327.

7. Samorì, B., *Stretching single molecules along unbinding and unfolding pathways with the scanning force microscope.* Chemistry–A European Journal, 2000. **6**(23): p. 4249-4255.

8. Janshoff, A., M. Neitzert, Y. Oberdörfer and H. Fuchs, *Force spectroscopy of molecular systems—single molecule spectroscopy of polymers and biomolecules.* Angewandte Chemie International Edition, 2000. **39**(18): p. 3212-3237.

9. Puchner, E.M. and H.E. Gaub, *Force and function: probing proteins with AFM-based force spectroscopy.* Current opinion in structural biology, 2009. **19**(5): p. 605-614.

10. Grandbois, M., M. Beyer, M. Rief, H. Clausen-Schaumann and H.E. Gaub, *How strong is a covalent bond?* Science, 1999. **283**(5408): p. 1727-1730.

11. Beyer, M.K. and H. Clausen-Schaumann, *Mechanochemistry: the mechanical activation of covalent bonds.* Chemical Reviews, 2005. **105**(8): p. 2921-2948.

12. Hickenboth, C.R., J.S. Moore, S.R. White, N.R. Sottos, J. Baudry and S.R. Wilson, *Biasing reaction pathways with mechanical force.* Nature, 2007. **446**(7134): p. 423.

13. Ong, M.T., J. Leiding, H. Tao, A.M. Virshup and T.J. Martínez, *First principles dynamics and minimum energy pathways for mechanochemical ring opening of*

cyclobutene. Journal of the American Chemical Society, 2009. **131**(18): p. 6377-6379.

14. Avdoshenko, S.M. and D.E. Makarov, *Reaction coordinates and pathways of mechanochemical transformations.* The Journal of Physical Chemistry B, 2015. **120**(8): p. 1537-1545.

15. Do, J.-L. and T. Friščić, *Mechanochemistry: a force of synthesis.* ACS central science, 2016. **3**(1): p. 13-19.

16. Schlegel, H.B., *Exploring potential energy surfaces for chemical reactions: an overview of some practical methods.* Journal of computational chemistry, 2003. **24**(12): p. 1514-1527.

17. Anslyn, E.V. and D.A. Dougherty, *Modern physical organic chemistry*. 2006: University Science Books.

18. Marcus, R.A., *Chemical and electrochemical electron-transfer theory.* Annual Review of Physical Chemistry, 1964. **15**(1): p. 155-196.

19. Konda, S.S.M., J.N. Brantley, B.T. Varghese, K.M. Wiggins, C.W. Bielawski and D.E. Makarov, *Molecular catch bonds and the anti-Hammond effect in polymer mechanochemistry.* Journal of the American Chemical Society, 2013. **135**(34): p. 12722-12729.

20. Makarov, D.E., *Perspective: Mechanochemistry of biological and synthetic molecules.* The Journal of chemical physics, 2016. **144**(3): p. 030901.

21. Ribas-Arino, J., M. Shiga and D. Marx, *Understanding covalent mechanochemistry.* Angewandte Chemie International Edition, 2009. **48**(23): p. 4190-4193.

22. Ribas-Arino, J. and D. Marx, *Covalent mechanochemistry: theoretical concepts and computational tools with applications to molecular nanomechanics.* Chemical reviews, 2012. **112**(10): p. 5412-5487.

23. Bockris, J.O.M. and Z. Nagy, *Symmetry factor and transfer coefficient. A source of confusion in electrode kinetics.* Journal of Chemical Education, 1973. **50**(12): p. 839.

24. Guidelli, R., R.G. Compton, J.M. Feliu, E. Gileadi, J. Lipkowski, W. Schmickler and S. Trasatti, *Defining the transfer coefficient in electrochemistry: An assessment (IUPAC Technical Report).* Pure and Applied Chemistry, 2014. **86**(2): p. 245-258.

25. Haines, P.J., *Thermal methods of analysis: principles, applications and problems*. 2012: Springer Science & Business Media.

26. Coats, A. and J. Redfern, *Kinetic parameters from thermogravimetric data.* 1964.

27. Arico, A.S., P. Bruce, B. Scrosati, J.-M. Tarascon and W. Van Schalkwijk, *Nanostructured materials for advanced energy conversion and storage devices.* Nature materials, 2005. **4**(5): p. 366-377.

28. Candelaria, S.L., Y. Shao, W. Zhou, X. Li, J. Xiao, J.-G. Zhang, Y. Wang, J. Liu, J. Li and G. Cao, *Nanostructured carbon for energy storage and conversion.* Nano Energy, 2012. **1**(2): p. 195-220.

29. Choi, H.-J., S.-M. Jung, J.-M. Seo, D.W. Chang, L. Dai and J.-B. Baek, *Graphene for energy conversion and storage in fuel cells and supercapacitors.* Nano Energy, 2012. **1**(4): p. 534-551.

30. Duan, X., Y. Huang, Y. Cui, J. Wang and C.M. Lieber, *Indium phosphide nanowires as building blocks for nanoscale electronic and optoelectronic devices.* Nature, 2001. **409**(6816): p. 66-69.

31. Wang, X., C.J. Summers and Z.L. Wang, *Large-scale hexagonal-patterned growth of aligned ZnO nanorods for nano-optoelectronics and nanosensor arrays.* Nano Letters, 2004. **4**(3): p. 423-426.

32. Dai, L., V. Sorkin and Y.-W. Zhang, *Effect of Surface Chemistry on the Mechanisms and Governing Laws of Friction and Wear.* ACS Applied Materials & Interfaces, 2016. **8**(13): p. 8765-8772.

33. Xue, Q., W. Liu and Z. Zhang, *Friction and wear properties of a surface-modified TiO 2 nanoparticle as an additive in liquid paraffin.* Wear, 1997. **213**(1): p. 29-32.

34. Lin, Y., A. Böker, J. He, K. Sill, H. Xiang, C. Abetz, X. Li, J. Wang, T. Emrick and S. Long, *Self-directed self-assembly of nanoparticle/copolymer mixtures.* Nature, 2005. **434**(7029): p. 55-59.

35. Albanese, A., P.S. Tang and W.C. Chan, *The effect of nanoparticle size, shape, and surface chemistry on biological systems.* Annual review of biomedical engineering, 2012. **14**: p. 1-16.

36. Jain, P.K., X. Huang, I.H. El-Sayed and M.A. El-Sayed, *Noble metals on the nanoscale: optical and photothermal properties and some applications in imaging, sensing, biology, and medicine.* Accounts of chemical research, 2008. **41**(12): p. 1578-1586.

37. Yang, K., J. Wan, S. Zhang, B. Tian, Y. Zhang and Z. Liu, *The influence of surface chemistry and size of nanoscale graphene oxide on photothermal therapy of cancer using ultra-low laser power.* Biomaterials, 2012. **33**(7): p. 2206-2214.

38. Daniel, M.-C. and D. Astruc, *Gold nanoparticles: assembly, supramolecular chemistry, quantum-size-related properties, and applications toward biology, catalysis, and nanotechnology.* Chemical reviews, 2004. **104**(1): p. 293-346.

39. Sapsford, K.E., W.R. Algar, L. Berti, K.B. Gemmill, B.J. Casey, E. Oh, M.H. Stewart and I.L. Medintz, *Functionalizing nanoparticles with biological molecules: developing chemistries that facilitate nanotechnology.* Chemical reviews, 2013. **113**(3): p. 1904-2074.

40. Guardingo, M., P. González-Monje, F. Novio, E. Bellido, F. Busqué, G. Molnár, A. Bousseksou and D. Ruiz-Molina, *Synthesis of Nanoscale Coordination Polymers in Femtoliter Reactors on Surfaces.* ACS nano, 2016. **10**(3): p. 3206-3213.

41. Cui, C.-H. and S.-H. Yu, *Engineering interface and surface of noble metal nanoparticle nanotubes toward enhanced catalytic activity for fuel cell applications.* Accounts of chemical research, 2013. **46**(7): p. 1427-1437.

42. Wang, L., D. Wang, Z. Dong, F. Zhang and J. Jin, *Interface chemistry engineering for stable cycling of reduced GO/SnO2 nanocomposites for lithium ion battery.* Nano letters, 2013. **13**(4): p. 1711-1716.

43. Kim, T., G. Jung, S. Yoo, K.S. Suh and R.S. Ruoff, *Activated graphene-based carbons as supercapacitor electrodes with macro-and mesopores.* Acs Nano, 2013. **7**(8): p. 6899-6905.

44. Sung, S., S. Park, W.-J. Lee, J. Son, C.-H. Kim, Y. Kim, D.Y. Noh and M.-H. Yoon, *Low-Voltage Flexible Organic Electronics Based on High-Performance Sol–Gel Titanium Dioxide Dielectric.* ACS applied materials & interfaces, 2015. **7**(14): p. 7456-7461.

45. Gosvami, N., J. Bares, F. Mangolini, A. Konicek, D. Yablon and R. Carpick, *Mechanisms of antiwear tribofilm growth revealed in situ by single-asperity sliding contacts.* Science, 2015. **348**(6230): p. 102-106.

46. Wu, G., P. Li, H. Feng, X. Zhang and P.K. Chu, *Engineering and functionalization of biomaterials via surface modification.* Journal of Materials Chemistry B, 2015. **3**(10): p. 2024-2042.

47. Avouris, P., T. Hertel and R. Martel, *Atomic force microscope tip-induced local oxidation of silicon: kinetics, mechanism, and nanofabrication.* Applied Physics Letters, 1997. **71**(2): p. 285-287.

48. Wei, Z., D. Wang, S. Kim, S.-Y. Kim, Y. Hu, M.K. Yakes, A.R. Laracuente, Z. Dai, S.R. Marder, C. Berger, W.P. King, W.A. de Heer, P.E. Sheehan and E. Riedo, *Nanoscale Tunable Reduction of Graphene Oxide for Graphene Electronics.* Science, 2010. **328**(5984): p. 1373-1376.

49. Felts, J.R., M.S. Onses, J.A. Rogers and W.P. King, *Nanometer Scale Alignment of Block-Copolymer Domains by Means of a Scanning Probe Tip.* Advanced Materials, 2014. **26**(19): p. 2999-3002.

50. Sheehan, P., L. Whitman, W.P. King and B.A. Nelson, *Nanoscale deposition of solid inks via thermal dip pen nanolithography.* Applied physics letters, 2004. **85**(9): p. 1589-1591.

51. Nelson, B.A., W. King, A. Laracuente, P. Sheehan and L. Whitman, *Direct deposition of continuous metal nanostructures by thermal dip-pen nanolithography.* Applied Physics Letters, 2006. **88**(3): p. 033104.

52. Carroll, K.M., A.J. Giordano, D. Wang, V.K. Kodali, J. Scrimgeour, W.P. King, S.R. Marder, E. Riedo and J.E. Curtis, *Fabricating Nanoscale Chemical Gradients with ThermoChemical NanoLithography.* Langmuir, 2013. **29**(27): p. 8675-8682.

53. Szoszkiewicz, R., T. Okada, S.C. Jones, T.-D. Li, W.P. King, S.R. Marder and E. Riedo, *High-speed, sub-15 nm feature size thermochemical nanolithography.* Nano Letters, 2007. **7**(4): p. 1064-1069.

54. Jacobs, T.D. and R.W. Carpick, *Nanoscale wear as a stress-assisted chemical reaction.* Nature nanotechnology, 2013. **8**(2): p. 108-112.

55. Butt, H.-J. and M. Jaschke, *Calculation of thermal noise in atomic force microscopy.* Nanotechnology, 1995. **6**(1): p. 1.

56. Raghuraman, S., M.B. Elinski, J.D. Batteas and J.R. Felts, *Driving Surface Chemistry at the Nanometer Scale Using Localized Heat and Stress.* Nano Letters, 2017. **17**(4): p. 2111-2117.

57. Nelson, B.A. and W. King, *Temperature calibration of heated silicon atomic force microscope cantilevers.* Sensors and Actuators A: Physical, 2007. **140**(1): p. 51-59.

58. Corbin, E.A. and W.P. King, *Electrical noise characteristics of a doped silicon microcantilever heater-thermometer.* Applied Physics Letters, 2011. **99**(26): p. 263107.

59. Felts, J.R., A.J. Oyer, S.C. Hernandez, K.E. Whitener, Jr., J.T. Robinson, S.G. Walton and P.E. Sheehan, *Direct mechanochemical cleavage of functional groups from graphene.* Nat Commun, 2015. **6**: p. 6467.

60. Ko, J.-H., S. Kwon, I.-S. Byun, J.S. Choi, B.H. Park, Y.-H. Kim and J.Y. Park, *Nanotribological properties of fluorinated, hydrogenated, and oxidized graphenes.* Tribology Letters, 2013. **50**(2): p. 137-144.

61. Pandey, D., R. Reifenberger and R. Piner, *Scanning probe microscopy study of exfoliated oxidized graphene sheets.* Surface Science, 2008. **602**(9): p. 1607-1613.

62. Zhurkov, S., *Kinetic concept of the strength of solids.* International Journal of Fracture, 1984. **26**(4): p. 295-307.

63. Bell, G.I., *Models for the specific adhesion of cells to cells.* Science, 1978. **200**(4342): p. 618-627.

64. Evans, E. and K. Ritchie, *Dynamic strength of molecular adhesion bonds.* Biophysical journal, 1997. **72**(4): p. 1541.

65. Merkel, R., P. Nassoy, A. Leung, K. Ritchie and E. Evans, *Energy landscapes of receptor–ligand bonds explored with dynamic force spectroscopy.* Nature, 1999. **397**(6714): p. 50-53.

66. Getfert, S., M. Evstigneev and P. Reimann, *Single-molecule force spectroscopy: practical limitations beyond Bell's model.* Physica A: Statistical Mechanics and its Applications, 2009. **388**(7): p. 1120-1132.

67. Valishin, A. and É. Kartashov, *Nonlinear effects in the kinetics of fracture of polymers and composites.* Strength of materials, 1993. **25**(6): p. 403-407.

68. Konda, S.S.M., J.N. Brantley, C.W. Bielawski and D.E. Makarov, *Chemical reactions modulated by mechanical stress: extended Bell theory.* The Journal of chemical physics, 2011. **135**(16): p. 164103.

69. Jencks, W.P., *A primer for the Bema Hapothle. An empirical approach to the characterization of changing transition-state structures.* Chemical Reviews, 1985. **85**(6): p. 511-527.

70. Larciprete, R., S. Fabris, T. Sun, P. Lacovig, A. Baraldi and S. Lizzit, *Dual path mechanism in the thermal reduction of graphene oxide.* Journal of the American Chemical Society, 2011. **133**(43): p. 17315-17321.

71. Jung, I., D.A. Field, N.J. Clark, Y. Zhu, D. Yang, R.D. Piner, S. Stankovich, D.A. Dikin, H. Geisler and C.A. Ventrice Jr, *Reduction kinetics of graphene oxide determined by electrical transport measurements and temperature programmed desorption.* The Journal of Physical Chemistry C, 2009. **113**(43): p. 18480-18486.

72. Mehmood, F., R. Pachter, W. Lu and J.J. Boeckl, *Adsorption and diffusion of oxygen on single-layer graphene with topological defects.* The Journal of Physical Chemistry C, 2013. **117**(20): p. 10366-10374.

73. Radovic, L.R., A. Suarez, F. Vallejos-Burgos and J.O. Sofo, *Oxygen migration on the graphene surface. 2. Thermochemistry of basal-plane diffusion (hopping).* Carbon, 2011. **49**(13): p. 4226-4238.

74. Kim, S., S. Zhou, Y. Hu, M. Acik, Y.J. Chabal, C. Berger, W. de Heer, A. Bongiorno and E. Riedo, *Room-temperature metastability of multilayer graphene oxide films.* Nature materials, 2012. **11**(6): p. 544-549.

75. Lee, C., Q. Li, W. Kalb, X.-Z. Liu, H. Berger, R.W. Carpick and J. Hone, *Frictional characteristics of atomically thin sheets.* Science, 2010. **328**(5974): p. 76-80.

76. Shunaev, V.V. and O.E. Glukhova, *Topology Influence on the Process of Graphene Functionalization by Epoxy and Hydroxyl Groups.* The Journal of Physical Chemistry C, 2016. **120**(7): p. 4145-4149.

77. Pumera, M., *Electrochemistry of graphene: new horizons for sensing and energy storage.* The Chemical Record, 2009. **9**(4): p. 211-223.

78. Conway, B.E., *Electrochemical supercapacitors: scientific fundamentals and technological applications*. 2013: Springer Science & Business Media.

79. Boulanger, C., *Thermoelectric material electroplating: a historical review.* Journal of electronic materials, 2010. **39**(9): p. 1818-1827.

80. Shockley, J.M., D.J. Horton and K.J. Wahl, *Effect of aging of 2507 super duplex stainless steel on sliding tribocorrosion in chloride solution.* Wear, 2017. **380**: p. 251-259.

81. Du, M., L. Cui, Y. Cao and A.J. Bard, *Mechanoelectrochemical catalysis of the effect of elastic strain on a platinum nanofilm for the ORR exerted by a shape*

memory alloy substrate. Journal of the American Chemical Society, 2015. **137**(23): p. 7397-7403.

82. Svedruzic, D. and B.A. Gregg, *Mechano-Electrochemistry and Fuel-Forming Mechano-Electrocatalysis on Spring Electrodes.* The Journal of Physical Chemistry C, 2014. **118**(33): p. 19246-19251.

83. Oja, S.M., M. Wood and B. Zhang, *Nanoscale electrochemistry.* Analytical chemistry, 2012. **85**(2): p. 473-486.

84. Eliaz, N. and M. Eliyahu, *Electrochemical processes of nucleation and growth of hydroxyapatite on titanium supported by real-time electrochemical atomic force microscopy.* Journal of Biomedical Materials Research Part A, 2007. **80**(3): p. 621-634.

85. Gross, L., F. Mohn, N. Moll, B. Schuler, A. Criado, E. Guitián, D. Peña, A. Gourdon and G. Meyer, *Bond-order discrimination by atomic force microscopy.* Science, 2012. **337**(6100): p. 1326-1329.

86. Li, Y., B.W. Maynor and J. Liu, *Electrochemical AFM "dip-pen" nanolithography.* Journal of the American Chemical Society, 2001. **123**(9): p. 2105-2106.

87. Macpherson, J.V. and P.R. Unwin, *Combined scanning electrochemical− atomic force microscopy.* Analytical Chemistry, 2000. **72**(2): p. 276-285.

88. Manne, S., P. Hansma, J. Massie, V. Elings and A. Gewirth, *Atomic-resolution electrochemistry with the atomic force microscope: copper deposition on gold.* Science, 1991. **251**(4990): p. 183-186.

89. Riss, A., A.P. Paz, S. Wickenburg, H.-Z. Tsai, D.G. De Oteyza, A.J. Bradley, M.M. Ugeda, P. Gorman, H.S. Jung and M.F. Crommie, *Imaging single-molecule reaction intermediates stabilized by surface dissipation and entropy.* Nature chemistry, 2016. **8**(7): p. 678-683.

90. Schuler, B., S. Fatayer, F. Mohn, N. Moll, N. Pavliček, G. Meyer, D. Peña and L. Gross, *Reversible Bergman cyclization by atomic manipulation.* Nature chemistry, 2016. **8**(3): p. 220-224.

91. Zhang, J., P. Chen, B. Yuan, W. Ji, Z. Cheng and X. Qiu, *Real-space identification of intermolecular bonding with atomic force microscopy.* Science, 2013. **342**(6158): p. 611-614.

92. Kueng, A., C. Kranz, A. Lugstein, E. Bertagnolli and B. Mizaikoff, *Integrated AFM–SECM in tapping mode: simultaneous topographical and electrochemical*

imaging of enzyme activity. Angewandte Chemie International Edition, 2003. **42**(28): p. 3238-3240.

93. Irmer, B., M. Kehrle, H. Lorenz and J. Kotthaus, *Nanolithography by non-contact AFM-induced local oxidation: fabrication of tunnelling barriers suitable for single-electron devices.* Semiconductor science and technology, 1998. **13**(8A): p. A79.

94. Takahashi, Y., A.I. Shevchuk, P. Novak, Y. Murakami, H. Shiku, Y.E. Korchev and T. Matsue, *Simultaneous noncontact topography and electrochemical imaging by SECM/SICM featuring ion current feedback regulation.* Journal of the American Chemical Society, 2010. **132**(29): p. 10118-10126.

95. Bard, A.J. and M.V. Mirkin, *Scanning electrochemical microscopy*. 2012: CRC Press.

96. Bergner, S., P. Vatsyayan and F.-M. Matysik, *Recent advances in high resolution scanning electrochemical microscopy of living cells–a review.* Analytica chimica acta, 2013. **775**: p. 1-13.

97. Bertoncello, P., *Advances on scanning electrochemical microscopy (SECM) for energy.* Energy & Environmental Science, 2010. **3**(11): p. 1620-1633.

98. Jesse, S., A. Kumar, T.M. Arruda, Y. Kim, S.V. Kalinin and F. Ciucci, *Electrochemical strain microscopy: Probing ionic and electrochemical phenomena in solids at the nanometer level.* Mrs Bulletin, 2012. **37**(7): p. 651-658.

99. Morozovska, A., E. Eliseev, N. Balke and S.V. Kalinin, *Local probing of ionic diffusion by electrochemical strain microscopy: Spatial resolution and signal formation mechanisms.* Journal of Applied Physics, 2010. **108**(5): p. 053712.

100. Ryu, Y.K. and R. Garcia, *Advanced oxidation scanning probe lithography.* Nanotechnology, 2017. **28**(14): p. 142003.

101. Hernández, J.G. and C. Bolm, *Altering product selectivity by mechanochemistry.* The Journal of organic chemistry, 2017. **82**(8): p. 4007-4019.

102. Han, X., S. Bian, Y. Liang, K. Houk and A.B. Braunschweig, *Reactions in elastomeric nanoreactors reveal the role of force on the kinetics of the Huisgen reaction on surfaces.* Journal of the American Chemical Society, 2014. **136**(30): p. 10553-10556.

103. Raghuraman, S., M. Soleymaniha, Z. Ye and J.R. Felts, *The role of mechanical force on the kinetics and dynamics of electrochemical redox reactions on graphene.* Nanoscale, 2018. **10**(37): p. 17912-17923.

104. Ondarçuhu, T. and L. Fabié, *Capillary Forces in Atomic Force Microscopy and Liquid Nanodispensing*, in *Surface Tension in Microsystems*. 2013, Springer. p. 279-305.

105. Spear, J.C., J.P. Custer and J.D. Batteas, *The influence of nanoscale roughness and substrate chemistry on the frictional properties of single and few layer graphene.* Nanoscale, 2015. **7**(22): p. 10021-10029.

106. Kuramochi, H., F. Pérez-Murano, J.A. Dagata and H. Yokoyama, *Faradaic current detection during anodic oxidation of the H-passivated p-Si (001) surface with controlled relative humidity.* Nanotechnology, 2003. **15**(3): p. 297.

107. Takemura, Y., Y. Shimada, G. Watanabe, T. Yamada and J.-i. Shirakashi. *Measurement of faradaic current during AFM local oxidation of magnetic metal thin films*. in *Journal of Physics: Conference Series*. 2007. IOP Publishing.

108. Byun, I.-S., W. Kim, D.W. Boukhvalov, I. Hwang, J.W. Son, G. Oh, J.S. Choi, D. Yoon, H. Cheong and J. Baik, *Electrical control of nanoscale functionalization in graphene by the scanning probe technique.* NPG Asia Materials, 2014. **6**(5): p. e102.

109. Felts, J.R., A.J. Oyer, S.C. Hernández, K.E. Whitener Jr, J.T. Robinson, S.G. Walton and P.E. Sheehan, *Direct mechanochemical cleavage of functional groups from graphene.* Nature communications, 2015. **6**.

110. Wei, Z., D. Wang, S. Kim, S.-Y. Kim, Y. Hu, M.K. Yakes, A.R. Laracuente, Z. Dai, S.R. Marder and C. Berger, *Nanoscale tunable reduction of graphene oxide for graphene electronics.* Science, 2010. **328**(5984): p. 1373-1376.

111. Zhurkov, A., *Kinetic concept of the strength of solids.* Int. J. Fract. Mech., 1965. **1**: p. 311-323.

112. Deng, Z., A. Smolyanitsky, Q. Li, X.-Q. Feng and R.J. Cannara, *Adhesion-dependent negative friction coefficient on chemically modified graphite at the nanoscale.* Nature materials, 2012. **11**(12): p. 1032.

113. Gong, P., Q. Li, X.-Z. Liu, R.W. Carpick and P. Egberts, *Adhesion Mechanics between Nanoscale Silicon Oxide Tips and Few-Layer Graphene.* Tribology Letters, 2017. **65**(2): p. 61.

114. Li, S., Q. Li, R.W. Carpick, P. Gumbsch, X.Z. Liu, X. Ding, J. Sun and J. Li, *The evolving quality of frictional contact with graphene.* Nature, 2016. **539**(7630): p. 541.

115. Nguyen, M.-T., *An ab initio study of oxygen on strained graphene.* Journal of Physics: Condensed Matter, 2013. **25**(39): p. 395301.

116. Katin, K.P., V.S. Prudkovskiy and M.M. Maslov, *Chemisorption of hydrogen atoms and hydroxyl groups on stretched graphene: A coupled QM/QM study.* Physics Letters A, 2017. **381**(33): p. 2686-2690.

117. Bissett, M.A., S. Konabe, S. Okada, M. Tsuji and H. Ago, *Enhanced chemical reactivity of graphene induced by mechanical strain.* ACS nano, 2013. **7**(11): p. 10335-10343.

118. Chen, P.Y., M. Liu, Z. Wang, R.H. Hurt and I.Y. Wong, *From Flatland to Spaceland: Higher Dimensional Patterning with Two-Dimensional Materials.* Advanced Materials, 2017. **29**(23): p. 1605096.

119. Choi, J., J. Mun, M.C. Wang, A. Ashraf, S.-W. Kang and S. Nam, *Hierarchical, dual-scale structures of atomically thin MoS2 for tunable wetting.* Nano letters, 2017. **17**(3): p. 1756-1761.

120. Song, J., Z. Yu, M.L. Gordin and D. Wang, *Advanced sulfur cathode enabled by highly crumpled nitrogen-doped graphene sheets for high-energy-density lithium–sulfur batteries.* Nano letters, 2016. **16**(2): p. 864-870.

121. Parviz, D., S.D. Metzler, S. Das, F. Irin and M.J. Green, *Tailored Crumpling and Unfolding of Spray-Dried Pristine Graphene and Graphene Oxide Sheets.* Small, 2015. **11**(22): p. 2661-2668.

122. Chen, W., X. Gui, L. Yang, H. Zhu and Z. Tang, *Wrinkling of two-dimensional materials: Methods, properties and applications.* Nanoscale Horizons, 2019. **4**(2): p. 291-320.

123. El Rouby, W.M., *Crumpled graphene: preparation and applications.* RSC Advances, 2015. **5**(82): p. 66767-66796.

124. Deng, S. and V. Berry, *Wrinkled, rippled and crumpled graphene: an overview of formation mechanism, electronic properties, and applications.* Materials Today, 2016. **19**(4): p. 197-212.

125. Pan, Z., N. Liu, L. Fu and Z. Liu, *Wrinkle engineering: a new approach to massive graphene nanoribbon arrays.* Journal of the American Chemical Society, 2011. **133**(44): p. 17578-17581.

126. Bai, K.-K., Y. Zhou, H. Zheng, L. Meng, H. Peng, Z. Liu, J.-C. Nie and L. He, *Creating one-dimensional nanoscale periodic ripples in a continuous mosaic graphene monolayer.* Physical review letters, 2014. **113**(8): p. 086102.

127. Pereira, V.M., A.C. Neto, H. Liang and L. Mahadevan, *Geometry, mechanics, and electronics of singular structures and wrinkles in graphene.* Physical review letters, 2010. **105**(15): p. 156603.

128. Yan, W., W.-Y. He, Z.-D. Chu, M. Liu, L. Meng, R.-F. Dou, Y. Zhang, Z. Liu, J.-C. Nie and L. He, *Strain and curvature induced evolution of electronic band structures in twisted graphene bilayer.* Nature communications, 2013. **4**: p. 2159.

129. Zang, J., S. Ryu, N. Pugno, Q. Wang, Q. Tu, M.J. Buehler and X. Zhao, *Multifunctionality and control of the crumpling and unfolding of large-area graphene.* Nature materials, 2013. **12**(4): p. 321.

130. Zhu, W., T. Low, V. Perebeinos, A.A. Bol, Y. Zhu, H. Yan, J. Tersoff and P. Avouris, *Structure and electronic transport in graphene wrinkles.* Nano letters, 2012. **12**(7): p. 3431-3436.

131. Cranford, S.W. and M.J. Buehler, *Packing efficiency and accessible surface area of crumpled graphene.* Physical Review B, 2011. **84**(20): p. 205451.

132. Shah, S., T. Habib, H. Gao, P. Gao, W. Sun, M. Green and M. Radovic, *Template-free 3D titanium carbide (Ti 3 C 2 T x) MXene particles crumpled by capillary forces.* Chemical Communications, 2017. **53**(2): p. 400-403.

133. Bari, R., D. Parviz, F. Khabaz, C.D. Klaassen, S.D. Metzler, M.J. Hansen, R. Khare and M.J. Green, *Liquid phase exfoliation and crumpling of inorganic nanosheets.* Physical Chemistry Chemical Physics, 2015. **17**(14): p. 9383-9393.

134. Lei, W., D. Liu and Y. Chen, *Highly crumpled boron nitride nanosheets as adsorbents: scalable solvent-less production.* Advanced Materials Interfaces, 2015. **2**(3): p. 1400529.

135. Xiong, F., Z. Cai, L. Qu, P. Zhang, Z. Yuan, O.K. Asare, W. Xu, C. Lin and L. Mai, *Three-dimensional crumpled reduced graphene oxide/MoS2 nanoflowers: a stable anode for lithium-ion batteries.* ACS applied materials interfaces, 2015. **7**(23): p. 12625-12630.

136. Yi, C., X. Chen, L. Zhang, X. Wang and C. Ke, *Nanomechanical z-shape folding of graphene on flat substrate.* Extreme Mechanics Letters, 2016. **9**: p. 84-90.

137. Baimova, A., E. Korznikova, S. Dmitriev, B. Liu and K. Zhou, *Review on Crumpled Graphene: Unique Mechanical Properties.* Reviews on Advanced Materials Science, 2014. **39**(1).

138. Baimova, J.A., B. Liu, S.V. Dmitriev and K. Zhou, *Mechanical properties of crumpled graphene under hydrostatic and uniaxial compression.* Journal of Physics D: Applied Physics, 2015. **48**(9): p. 095302.

139. Bonilla, M., J. Stokes, M. Gidley and G. Yakubov, *Interpreting atomic force microscopy nanoindentation of hierarchical biological materials using multi-regime analysis.* Soft Matter, 2015. **11**(7): p. 1281-1292.

140. Briscoe, B., K. Sebastian and M.J.J.o.P.D.A.P. Adams, *The effect of indenter geometry on the elastic response to indentation.* Journal of Physics D: Applied Physics Letters, 1994. **27**(6): p. 1156.

141. Meng, X.-H., M. Li, Z. Kang and J.-L. Xiao, *Folding of multi-layer graphene sheets induced by van der Waals interaction.* Acta Mechanica Sinica, 2014. **30**(3): p. 410-417.

142. Cranford, S., D. Sen and M.J. Buehler, *Meso-origami: folding multilayer graphene sheets.* Applied physics letters, 2009. **95**(12): p. 123121.

143. Meng, X., M. Li, Z. Kang, X. Zhang and J. Xiao, *Mechanics of self-folding of single-layer graphene.* Journal of Physics D: Applied Physics, 2013. **46**(5): p. 055308.

144. Su, N., M. Liu and F. Liu, *Chemical versus thermal folding of graphene edges.* Nano Research, 2011. **4**(12): p. 1242-1247.

145. Poulin, P., R. Jalili, W. Neri, F. Nallet, T. Divoux, A. Colin, S.H. Aboutalebi, G. Wallace and C. Zakri, *Superflexibility of graphene oxide.* Proceedings of the National Academy of Sciences, 2016. **113**(40): p. 11088-11093.

146. Becton, M., L. Zhang and X. Wang, *On the crumpling of polycrystalline graphene by molecular dynamics simulation.* Physical Chemistry Chemical Physics, 2015. **17**(9): p. 6297-6304.

147. Giordanelli, I., M. Mendoza, J.S. Andrade Jr, M. Gomes and H.J. Herrmann, *Crumpling Damaged Graphene.* Scientific reports, 2016. **6**: p. 25891.

148. Anastas, P.T. and J.C. Warner, *Green chemistry.* Frontiers, 1998. **640**.

149. Anastas, P. and N. Eghbali, *Green chemistry: principles and practice.* Chemical Society Reviews, 2010. **39**(1): p. 301-312.

150. Poliakoff, M., J.M. Fitzpatrick, T.R. Farren and P.T. Anastas, *Green chemistry: science and politics of change.* Science, 2002. **297**(5582): p. 807-810.

151. Baláž, P., M. Achimovičová, M. Baláž, P. Billik, Z. Cherkezova-Zheleva, J.M. Criado, F. Delogu, E. Dutková, E. Gaffet and F.J. Gotor, *Hallmarks of mechanochemistry: from nanoparticles to technology.* Chemical Society Reviews, 2013. **42**(18): p. 7571-7637.

152. Batzdorf, L., F. Fischer, M. Wilke, K.J. Wenzel and F. Emmerling, *Direct In Situ Investigation of Milling Reactions Using Combined X-ray Diffraction and Raman Spectroscopy.* Angewandte Chemie International Edition, 2015. **54**(6): p. 1799-1802.

153. Gracin, D., V. Štrukil, T. Friščić, I. Halasz and K. Užarević, *Laboratory Real-Time and In Situ Monitoring of Mechanochemical Milling Reactions by Raman Spectroscopy.* Angewandte Chemie International Edition, 2014. **53**(24): p. 6193-6197.

154. Friščić, T., I. Halasz, P.J. Beldon, A.M. Belenguer, F. Adams, S.A. Kimber, V. Honkimäki and R.E. Dinnebier, *Real-time and in situ monitoring of mechanochemical milling reactions.* Nature chemistry, 2013. **5**(1): p. 66.

155. Halasz, I., T. Friščić, S.A. Kimber, K. Užarević, A. Puškarić, C. Mottillo, P. Julien, V. Štrukil, V. Honkimäki and R.E. Dinnebier, *Quantitative in situ and real-time monitoring of mechanochemical reactions.* Faraday discussions, 2014. **170**: p. 203-221.

156. Katsenis, A.D., A. Puškarić, V. Štrukil, C. Mottillo, P.A. Julien, K. Užarević, M.-H. Pham, T.-O. Do, S.A. Kimber and P. Lazić, *In situ X-ray diffraction monitoring of a mechanochemical reaction reveals a unique topology metal-organic framework.* Nature communications, 2015. **6**: p. 6662.

157. Karki, S., T. Friščić and W. Jones, *Control and interconversion of cocrystal stoichiometry in grinding: stepwise mechanism for the formation of a hydrogen-bonded cocrystal.* CrystEngComm, 2009. **11**(3): p. 470-481.

158. Mavračić, J., D. Cinčić and B. Kaitner, *Halogen bonding of N-bromosuccinimide by grinding.* CrystEngComm, 2016. **18**(19): p. 3343-3346.

159. Trask, A.V., J. van de Streek, W.S. Motherwell and W. Jones, *Achieving polymorphic and stoichiometric diversity in cocrystal formation: Importance of solid-state grinding, powder X-ray structure determination, and seeding.* Crystal growth design, 2005. **5**(6): p. 2233-2241.

160. Štrukil, V., L. Fábián, D.G. Reid, M.J. Duer, G.J. Jackson, M. Eckert-Maksić and T. Friščić, *Towards an environmentally-friendly laboratory: dimensionality and reactivity in the mechanosynthesis of metal–organic compounds.* Chemical communications, 2010. **46**(48): p. 9191-9193.

161. Wang, G.-W., K. Komatsu, Y. Murata and M. Shiro, *Synthesis and X-ray structure of dumb-bell-shaped C 120.* Nature, 1997. **387**(6633): p. 583.

162. Korpany, K.V., C. Mottillo, J. Bachelder, S.N. Cross, P. Dong, S. Trudel, T. Friščić and A.S. Blum, *One-step ligand exchange and switching from hydrophobic to water-stable hydrophilic superparamagnetic iron oxide nanoparticles by mechanochemical milling.* Chemical Communications, 2016. **52**(14): p. 3054-3057.

163. Rak, M.J., N.K. Saadé, T. Friščić and A. Moores, *Mechanosynthesis of ultra-small monodisperse amine-stabilized gold nanoparticles with controllable size.* Green Chemistry, 2014. **16**(1): p. 86-89.

164. Weymouth, A.J., D. Meuer, P. Mutombo, T. Wutscher, M. Ondracek, P. Jelinek and F.J. Giessibl, *Atomic structure affects the directional dependence of friction.* Physical review letters, 2013. **111**(12): p. 126103.

165. Yu, C. and Q.J. Wang, *Friction anisotropy with respect to topographic orientation.* Scientific reports, 2012. **2**: p. 988.

166. Szlufarska, I., M. Chandross and R.W. Carpick, *Recent advances in single-asperity nanotribology.* Journal of Physics D: Applied Physics, 2008. **41**(12): p. 123001.

167. Su, W., N. Kumar, A. Krayev and M. Chaigneau, *In situ topographical chemical and electrical imaging of carboxyl graphene oxide at the nanoscale.* Nature communications, 2018. **9**(1): p. 2891.

168. Liu, Z., T. Rios-Carvajal, M. Ceccato and T. Hassenkam, *Nanoscale chemical mapping of oxygen functional groups on graphene oxide using atomic force microscopy-coupled infrared spectroscopy.* Journal of colloid interface science, 2019. **556**: p. 458-465.

169. Carpick, R.W., D.F. Ogletree and M.J.J.o.c. Salmeron, *A general equation for fitting contact area and friction vs load measurements.* Journal of colloid, interface science, 1999. **211**(2): p. 395-400.

170. Braun, O. and M. Peyrard, *Dependence of kinetic friction on velocity: Master equation approach.* Physical Review E, 2011. **83**(4): p. 046129.

171. Riedo, E., E. Gnecco, R. Bennewitz, E. Meyer and H. Brune, *Interaction potential and hopping dynamics governing sliding friction.* Physical review letters, 2003. **91**(8): p. 084502.

172. Disma, F., L. Aymard, L. Dupont and J.M. Tarascon, *Effect of mechanical grinding on the lithium intercalation process in graphites and soft carbons.* Journal of the Electrochemical Society, 1996. **143**(12): p. 3959-3972.

173. Salver-Disma, F., C. Lenain, B. Beaudoin, L. Aymard and J.-M. Tarascon, *Unique effect of mechanical milling on the lithium intercalation properties of different carbons.* Solid State Ionics, 1997. **98**(3-4): p. 145-158.